Scandinavian Workshop on Imaging Food Quality 2011

Ystad, May 27, 2011

Proceedings

IMM-Technical Report-2011-15

Organizers:
Assistant Professor Line Clemmensen, Technical University of Denmark
Professor Jussi Parkkinen, University of Eastern Finland
Professor Jon Yngve Hardeberg, Gjövik University College
Professor Rasmus Larsen, Technical University of Denmark
Professor Bjarne Ersbøll, Technical University of Denmark

List of content

Using image analysis based on light scattering for non-invasive characterization of “edible soft matter”

Alan Parker

Department of Materials Science, Firmenich SA, 7, rue de la Bergère, CH-1211 Meyrin 2 Geneva, Switzerland

Abstract. Light scattering is a powerful method for non-invasive characterization of materials, especially soft matter. Traditionally, point detectors are used, such as photomultipliers or avalanche photodiodes. The introduction of camera-based detection has caused a revolution in light scattering. Its main advantage is that each pixel can act as a point detector, so acquisition rates are vastly increased. However, cameras cannot completely replace traditional detectors.

First, I give a short, broad brush review of light scattering techniques, including the use of polarized light. I point out those that are most suitable for camera-based methods. Second, I explain in more detail several techniques of camera-based light scattering that either could or have been used to characterize food systems. These techniques are equally applicable to any other kind of soft matter, such as ink, cement, or cosmetics.

Actual or potential applications include: tracking emulsification in real time without dilution, measuring the gelling of milk and measuring the drying of a concentrated solution.

Sensometrics for Food Quality Control

Per Bruun Brockhoff

DTU Informatics, Technical University of Denmark,
Richard Petersens Plads, Building 321, DK-2800 Lyngby, Denmark,
www.imm.dtu.dk/~pbb, pbb@imm.dtu.dk

Abstract. The industrial development of innovative and succesful food items and the measuring of food quality in general is difficult without actually letting human beings evaluate the products using their senses at some point in the process. The use of humans as measurement instruments calls for special attention in the modelling and data analysis phase. In this paper the focus is on sensometrics – the „metric“ side of the sensory science field. The sensometrics field is introduced and related to the fields of statistics, chemometrics and psychometrics. Some of the most commonly used sensory testing methods are introduced and some of the corresponding sensometrics methods reviewed and discussed.
Keywords: Sensometrics, Statistics, Chemometrics, Psychometrics, Sensory.

1 Introduction

The current contribution is an extended version of [1]. The use of humans as measurement instruments is playing an increasing role in product development and user driven innovation in many industries. This ranges from the use of experts and trained human test panels to market studies where the consumer population is tested for preference and behaviour patterns. This calls for improved understanding on one side of the human measurement instrument itself and on the other side the modelling and empirical treatment of data. The scientific grounds for obtaining improvements within a given industry span from experimental psychology to mathematical modelling, statistics, chemometrics and machine learning together with specific product knowledge be it food, TVs, Hearing aids, mobile phones or whatever.

In particular in the food industry sensory and consumer data is frequently produced and applied as the basis for decision making. And in the field of food research, sensory and consumer data is produced and used similar to the industrial use, and academic environments specifically for sensory and consumer sciences exists worldwide. The development and application of statistics and data analysis within this area is called sensometrics.

2 Sensometrics

2.1 Sensometrics and Sensory Science

As the name indicates sensometrics really grew out of and is still closely linked to sensory science, where the use of trained sensory panels plays a central role. Sensory science is the cross disciplinary scientific field dealing with human perception of stimuli and the way they act upon sensory input. Sensory food research focuses on better understanding of how the senses react during food intake, but also how our senses can be used in quality control and innovative product development. Historically it can be viewed as a merger of simple industrial product testing with psychophysics as originated by G. T. Fechner and S.S. Stevens in the 19th century. Probably the first exposition of the modern sensory science is given by [2]. Rose Marie Pangborn(1932-1990) was considered one of the pioneers of sensory analysis of food and the main global scientific conference in sensory science is named after her. The 1st Pangborn Symposium was held in Helsinki, Finland in 1992 and these conferences are approaching in the order of 1000 participants - the 9th will take place in Toronto, Canada in 2011. Jointly with this, international Sensometrics conferences have been held also since 1992, where the first took place in Leiden, Holland (as a small workshop) and the 10th took place in Rotterdam, Holland in 2010. The sensometrics conferences have a participation level of around 150. Both conferences are working together with the Elsevier Journal Food Quality and Preference which is also the official membership journal for the Sensometrics Society (www.sensometric.org).

2.2 Sensometrics: Statistics, Psychometrics or Chemometrics?

The “sensometrician” is faced with a vast collection of data types from a widespread number of experimental settings ranging from a simple one sample binomial outcome to complex dynamical and/or multivariate data sets, see e.g. [3] for a recent review of quantitative sensory methodology. So what is really (good) sensometrics? The answer will depend on the background of the sensometrician, which for the majority, if not a food scientist, is coming from one of the following fields: generic statistics, psychophysics/experimental psychology or chemometrics.

The generic statistician arch type would commonly carry out the data analysis as a purely “empirical” exercise in the sense that methods are not based on any models for the fundamental psychological characteristics underlying the sensory phenomena that the measurements express. The advantage of a strong link to the generic scientific fields of mathematical and applied statistics is the ability to employ the most modern statistical techniques when relevant for sensory data and to be on top of sampling uncertainty and formal statistical inferential reasoning. And this is certainly needed for the sensory field as for any other field producing experimental data. The weakness is that the lack of proper psychophysical models may lead to inadequate interpretations of the analysis results. In e.g. [4] the first sentence of the abstract is expressing this concern rather severely: “Sensory and hedonic variability are fundamental psychological characteristics that must be explicitly modeled if one is to

develop meaningful statistical models of sensory phenomena." A fundamental challenge of this ambitious approach is that the required psychophysical (probabilistic) models of behavior is on one hand only vaguely verifiable, since they are based on models of a (partly) unobserved system, the human brain and perceptual system, and on the other may lead to rather complicated statistical models. [4] is published in a special sensory data issue of The Journal of Chemometrics, see [5]. Chemometricians are the third and final arch type of a sensometrician. In chemometrics the focus is more on multivariate data analysis and for some the explorative principle is at the very heart of the field, see e.g. [6] and [7]. The advantage of the chemometrics approach is that usually all multivariate features of the data are studied without forcing certain potentially inadequate model structures on the data. The weakness is exactly also this lack of modelling rendering potentially certain well understood psychophysical phenomena for the explorative modelling to find out by itself. Also, linked with the explorative approach, the formal statistical inferential reasoning is sometimes considered less important by the chemometrician.

Now, none of these arch types are (at their best) unintelligent and they would all three of them understand (some of) the limitations of their pure versions of analysis approach. And they all have ways of dealing with (some of) these concerns for practical data analysis, such that often, at the end of the day, the end results may not differ that much. There is though, in the point of view of this author, a lack of comprehensive comparisons between these different approaches where they all are used at their best.

3 Sensory Profile Data

Probably the most used sensory technique is the so-called sensory profiling – a quantitative descriptive analysis, where a number of products are evaluated on a continuous line scale with respect to a number of properties. In sensory profiling the panellists develop a test vocabulary (defining attributes) for the product category and rate the intensity of these attributes for a set of different samples within the category. Thus, a sensory profile of each product is provided for each of the panellists, and most often this is replicated, see [8]. Hence, data is inherently multivariate as many characteristics of the products are measured.

The statistics arch type would focus on the ANOVA structure of the setting and perform univariate and multivariate analysis of variance (ANOVA) and would make sure that the proper version of a mixed model ANOVA is used, see e.g. [9] and [10]. For studying the multivariate product structure the Canonical Variates Analysis (CVA) within the Multivariate ANOVA (MANOVA) framework would be the natural choice, see eg. [11], since it would be an analysis that incorporates the within product (co)variability.

The chemometrics arch type would begin with principal components analysis (PCA) on averaged and/or unfolded data. For more elaborate analysis maybe 3-way methods, see [12], [13] or other more ANOVA like extensions would be used, see e.g. [14]. Analysis accounting for within product (co)variability could be provided by extensions as presented in [15] or in [16].

In [4] the approach for this type of data is that of probabilistic multidimensional scaling (PROSCAL). In short, a formal statistical model for product differences is expressed as variability on the (low-dimensional) underlying latent sensory scale. It is usually presented as superior to the use of e.g. standard PCA, focussing on the point that it naturally includes models for different within product variability, which in the standard PCA could be confounded with the "signal" – the inter product distances.

One recurrent issue in sensometrics is the monitoring and/or accounting for individual differences in sensory panel data also called dealing with panel performance. A model based approach within the univariate ANOVA framework was introduced in [17] leading to multiplicative models for interaction effect expressing the individual varying scale usage. In [18] the open source stand alone software PanelCheck (www.panelcheck.com) was introduced as a general tool for panelist performance analysis. PanelCheck was developed in a Danish/Norwegian consortium of industrial and research partners to optimize the industrial use of the tool while still maintaining the proper statistical methodology. PanelCheck also gives tools for the heavily used univariate attribute-by-attribute analysis of variance (ANOVA). Standard univariate mixed model analysis of variance is then used to investigate the product differences for each attribute, see [10]. In [19], [20] and [21] random effect versions of such analyses were put forward leading to either a multiplicative (nonlinear) mixed model or a linear random coefficient model. This approach offers a synthesis of the individuality focus with the random effect approach that really applies when product differences are in focus.

Specifically, scaling differences will often constitute a non-trivial part of the assessor-by-product interaction in such sensory profile data, [22], [23] and [24]. In [21] a new mixed model ANOVA analysis approach is suggested that properly takes this into account by a simple inclusion of the product averages as covariates in the modeling and allow the covariate regression coefficients to depend on the assessor. This gives a more powerful analysis and provides more correct confidence limits that are deduced as an adjusted version of the linear random scaling model confidence limits. In 52 sensory profile data sets with all together 564 attributes, 344 (61.1%) showed significant (P-value<0.10) scaling difference. Among almost all these 344 attributes, the product difference P-values were for the new approach smaller than for the traditional analysis. In 15 cases an attribute was significant on level 5% by the new approach and not so by the classical approach and in 5 more cases on level 10%. These 20 changed conclusions were among 37 attributes showing significant scaling differences in spite of being claimed NS by the traditional analysis - and all together only 87 attributes out of the 564 were claimed NS by the traditional approach. Among these 344 attributes, 33.432 post-hoc comparisons were calculated. In 13.503 cases the classical analysis claimed significance (5%) but the new analysis claimed so in 15.137 cases. Still, generally the new, and non-symmetrical, confidence limits are more often wider than narrower compared to the classical ones: in 19.926 cases the new lower limit was wider and in 26.591 cases the new upper limit was wider. In the final paper the meta study will be extended to include an investigation in SensoBase (www.sensobase.fr), using in the order of 500 profile data sets with around 9000 attributes.

4 Basic Sensory Difference and Similarity Test Data

The so-called difference and/or similarity tests are a commonly used sensory technique resulting in binary and/or categorical frequency data - the so-called triangle test is a classical example. In the triangle test an individual is presented with 3 samples, two of which are the same, and then asked to select the odd sample. The result is binary: correct or incorrect. Such sensory tests were already in the 1950s treated by the statistical community, see e.g. [25] and [26]. These types of tests and results have also been treated extensively from a more psychophysical approach, often here denoted a Thurstonian approach. The focus in the Thurstonian approach is on quantifying/estimating the underlying sensory difference d between the two products that are compared in the difference test. This is done by setting up mathematical/psycho-physical models for the cognitive decision processes that are used by assessors in each sensory test protocol, see e.g. [27]. For the triangle test, the usual model for how the cognitive decision process is taking place is that the most deviating product would be the answer – sometimes called that the assessors are using a so-called tau-strategy. Using basic probability calculus on 3 realizations from two different normal distributions, differing by exactly the true underlying sensory difference d, one can deduce the probability of getting the answer correct for such a strategy. This function is called the psychometric function and relates the observed number of correct answers to the underlying sensory difference d. Different test protocols will then lead to different psychometric functions.

In [28] probably the first systematic exposition of the psychological scaling theory and methods by Thurstone was given. This included a sound psychological basis as well as a statistical one with the use and theory of maximum likelihood methods. Within the field known as signal detection theory, see e.g. [29] or [30], methods of this kind were further developed, originally with special emphasis on detecting weak visual or auditory signals. Further developments of such methods and their use within food testing and sensory science have developed over the last couple of decades with the numerous contributions of D. Ennis as a corner stone see e.g. [31]. In [32] it was emphasized and exploited that the thurstonian based statistical analysis of data from the basic sensory discrimination test protocols can be identified as generalized linear models using the inverse psychometric functions as link functions. With this in place, it is possible to extend and combine designed experimentation with discrimination/similarity testing and combine standard statistical modeling/analysis with thurstonian modeling. All this was implemented in the R-package *sensR*, cf [33]. So *sensR* now offers a complete tool for the planning and analysis of sensory discrimination and similarity experiments. The *sensR* package includes easily accessible tools for handling the six basic sensory test protocols: duo-trio, triangle, 2-AFC, 3-AFC, A-not A and Same-Different test. For all of these sensR provides:

- power and sample size calculations
- simulation
- hypothesis tests
- standard and improved (likelihood based) confidence intervals
- thurstonian analysis
- plotting features

In addition to this sensR currently offers:

- Analysis of A-not-A tests with or without sureness response
- ROC curve computations and plotting
- Signal Detection Theory (SDT) Computation of d-prime
- Beta-Binomial (standard and corrected) analysis for replicated data
- Replicated Thurstonian Model for discrimination analysis
- A link between standard statistical (regression/anova/ancova) modeling and thurstonian modeling.
- Simulation of replicated difference tests

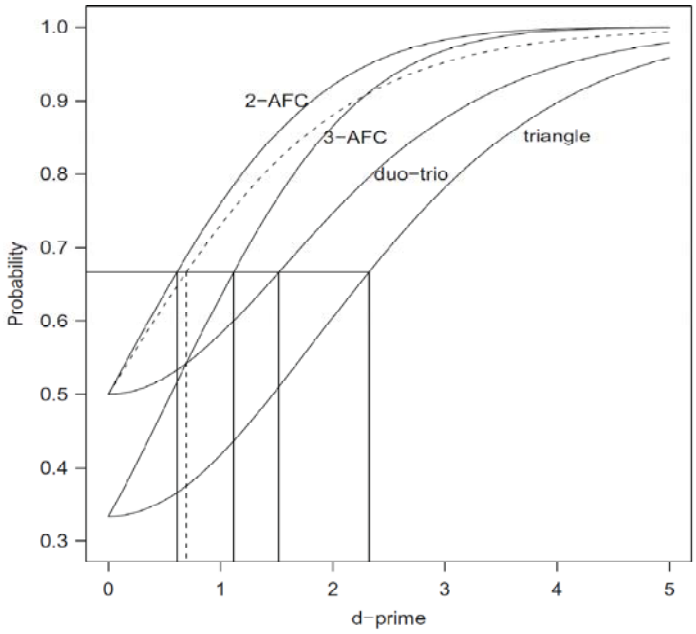

Fig. 1. The four psychometric functions used for the four basic testing protocols. The logistic link function is shown as the dashed curve. A response of 2/3 correct answer leads to four different estimates of sensory difference in the four different protocols (neither of which equals the logistic based estimate)

The basic idea from [32] is shown in Figure 1 illustrating the four basic psychometric functions together with the logistic link function. It is emphasized how a response of 2/3 correct answers has quite different interpretation depending on how the sensory testing protocol was actually carried out. Or expressed in more popular terms: The answer you get depends on the question you pose! The thurstonian modeling approach offers an approach to explicitly include the modeling of the question dependency into the data analysis framework. Linking this more to general statistical

theory and methods than traditionally done in the literature offers an extended and improved toolbox of methods. This becomes evident, when turning to mixed effect versions of these models, which, as for the profile data above, becomes highly relevant to capture and model individual differences in such data. Due to the complexity of this challenge, these issues are still discussed in the sensory and sensometrics literature, and much more work is called for here. A friendly introduction to the analysis of the basic discrimination and similarity testing data is given in Chapter 8 in [10].

5 Other Types of Data

5.1 Ranking and ordinal data

Another commonly used sensory and consumer survey methodology is to use rankings or scoring on an ordinal scale. In [34] a general approach for non-parametric analysis based on orthogonal polynomial decompositions is presented. The methods are applicable in a variety of situations but were not well suited to handle ties in the data. In [35] a method is developed based on polynomials that are orthogonal with respect to the given tie structure that allows for ties in this kind of analysis. Among other things it is shown that the generalized decomposition of the Anderson χ-statistic for randomized block designs allowing for ties has a first component that equals the well known tie corrected version of the Friedman statistic. The second component is a novel tie corrected test for dispersion effects. This is an important aspect of consumer preference data as this may reflect segmentations in the population. In [36] and [37] this extended methodology is presented in a more applied oriented way. In [38] the methods are extended and exemplified for the incomplete block design setting. In [39] the methods are presented in a user friendly way to the sensory practitioner including a website with relevant R code (http://www2.imm.dtu.dk/stat/nonparametrics/).

The disadvantage of this classical nonparametric approach to such data is the lack of models and hence the lack of the ability to easily quantify the effects and their (proper) uncertainty including random effects of individuals. A model based approach is taken in [40] and [21]. The close link between certain Thurstonian models and well established statistical models are extended to these data and the consequence of including proper random effect models are illustrated. In the new R-package *ordinal*, cf. [41], likelihood based models for ordinal (ordered categorical) data based on cumulative probabilities are implemented in the framework of cumulative link (mixed) models. This includes the important proportional odds model but also allows for general regression structures for location as well as scale of the latent distribution, i.e. additive as well as multiplicative structures, structured thresholds (cut-points), nominal effects, flexible link functions and random effects.

5.2 Linking multivariate data

Another recurring issue is the relation of multivariate data sets, e.g. trying to predict sensory response by instrumental/ spectroscopic and/or chemical

measurements. Similarly there is a wish to be able to predict how the market(consumers) will react to sensory changes in food products – then called Preference Mapping, [42]. This links the area closely to the chemometrics field and also naturally to the (machine) learning area. When analyzing consumer data a possible market segmentation is a key issue. So for relational models the so-called latent class regression models have been used frequently in market research. In [43] and [44] a `latent class random coefficient' regression model is formulated, handled and applied. It is a combination of the typical latent class regression model and the typical random coefficient model. Furthermore it is combined with principal component regression.

For such regression and/or correlation analyses often average sensory data is used. The issue of correcting for the ``measurement error'' of these averages is treated in [45], [46] and [47]. In [47] it is among other things described how simple F-test statistics can be used for the diagnostics and correction of measurement error in simple correlations in even rather complex settings.

One of the big challenges in the food industrial R&D process is the comparability/predictability of different levels of testing procedures/protocols applied throughout the development process – many of which may involve human perception. This goes from in house fast screening methods through more elaborate sensory evaluations to larger scale consumer surveys. A coherent theme is hence to develop methodology that can disentangle product differences from human differences, and jointly to be able to do so for data with multi-protocol origin. The multi-protocol data setup is a current research topic.

Another important open source tool for the analysis of sensory and consumer data is the the R-based SensoMiner, [48].

6 References

1. Brockhoff, P.B.: Sensometrics. In: International Encyclopedia of Statistical Science (Ed: M. Lovric), Part 19, 1302-1305, Springer (2011)
2. Amerine, M.A., Pangborn, R.M. and Roessler, E.B.: Principles of sensory evaluation of food. Academic press, New York (1965)
3. Bredie, W.L.P., Dehlholm, C., Byrne D.V. and Martens, M.: Descriptive sensory analysis of food: a review, to be submitted to: Food Quality and Preference (2011)
4. MacKay, D.B.: Probabilistic scaling analyses of sensory profile, instrumental and hedonic data. Journal of Chemometrics 19 (3),180-190 (2005)
5. Brockhoff, P. B., Næs, T., Qannari, M.: Editorship, Journal of Chemometrics, 19(3), pp. 121 (2005)
6. Munck, L.: A new holistic exploratory approach to Systems Biology by Near Infrared Spectroscopy evaluated by chemometrics and data inspection. Journal of Chemometrics 21, 406-426 (2007)
7. Martens, H. and Martens, M.: Multivariate Analysis of Quality: An Introduction. Wiley, Chicester, UK (2001)
8. Lawless, H. T., & Heymann, H.: Sensory evaluation of food. Principles and Practices. New York: Chapman & Hall (1999)
9. Lea, P. Næs, T. and Rødbotten, M.: Analysis of variance of sensory data. J. Wiley and sons (1997)

10. Næs, T., Tomic, O. and Brockhoff, P.B.: Statistics for Sensory and Consumer Science, John Wiley & Sons (2010)
11. Schlich, P.: What are the sensory differences among coffees? Multi-panel analysis of variance and flash analysis. Food Quality and Preference 9, 103 (1998)
12. Brockhoff, P, Hirst, D. and Næs, T.: Analysing individual profiles by three-way factor analysis. In T. Næs & E. Risvik (Eds.), Multivariate Analysis of Data in Sensory Science (Vol. 16 - Data handling in science and technology, pp. 71-102): Elsevier Science B.V. (1996)
13. Bro, R., Qannari, E.M, Kiers, H.A., Næs, T. And Frøst, M.B.: Multi-way models for sensory profiling data. J. Chemometrics, 22, 36-45 (2008)
14. Luciano, G. and Næs, T.: Interpreting sensory data by combining principal component analysis and analysis of variance. Food Quality and Preference 20(3), 167-175 (2009)
15. Bro, R., Sidiropoulos, N.D., Smilde, A.K.: Maximum likelihood fitting using ordinary least squares algorithms, Journal of Chemometrics, 16(8-10), 387-400 (2002)
16. Martens, H., Hoy, M., Wise, B., Bro, R. and Brockhoff, P.B.: Pre-whitening of data by covariance-weighted pre-processing. Journal of Chemometrics 17(3), 153-165 (2003)
17. Brockhoff, P.M. and Skovgaard, I.M.: Modelling individual differences between assessors in sensory evaluations. Food Quality and Preference 5, 215-224 (1994)
18. Tomic, O., Nilsen, A. N., Martens, M., Næs, T.: Visualization of sensory profiling data for performance monitoring, LWT - Food Science and Technology, 40, 262 – 269 (2007)
19. Smith A, Cullis B, Brockhoff P. and Thompson R.: Multiplicative mixed models for the analysis of sensory evaluation data. Food Quality and Preference 14(5-6), 387-395 (2003)
20. Brockhoff, P.B. and Sommer, N.A.: Accounting for scaling differences in sensory profile data. Proceedings of 10th European Symposium on Statistical Methods for the Food Industry, pp. 283-290, Louvain-La-Neuve, Belgium (2008)
21. Christensen, R.H.B. and Brockhoff P.B.: Analysis of replicated ordinal ratings data from sensory experiments. Submitted to: Food Quality and Preference (2011)
22. Brockhoff, P.B.: Statistical testing of individual differences in sensory profiling. FQP, 14(5-6), 425-434 (2003)
23. Brockhoff, P.M.: Assessor modelling. FQP, 9(3), 87-89 (1998)
24. Brockhoff, P.M. and Skovgaard, I.M.: Modelling individual differences between assessors in sensory evaluations. FQP, 5, 215-224 (1994)
25. Hopkins, J.W.: A Procedure for quantifying subjective appraisals of odor, flavour and texture of foodstuffs. Biometrics, 6 (1), 1-16 (1950)
26. Bradley, R.A.: Triangle, Duo-trio, and Difference-from-Control tests in taste testing, Biometrics 14: 566 (1958)
27. Ennis, D. M.: The power of sensory discrimination methods. Journal of Sensory Studies, 8, 353–370 (1993)
28. Bock, D. R., Jones, L. V.: The measurement and prediction of judgment andchoice. Holden-Day, San Francisco (1968)
29. Green, D. M., & Swets, J. A.: Signal detection theory and psychophysics. John Wiley & Sons (1966)
30. Macmillan, N. A. and Creelman, C.D.: Detection Theory, A User's Guide (2nd ed.). Lawrence Elbaum Associates, Publishers (2005)
31. Ennis, D.M.: Foundations of sensory science. In H.R. Moskowitz, A.M. Munoz, and M.C. Gacula (Eds.), Viewpoints and Controversies in Sensory Science and Consumer Product Testing. Trumbull, CT: Food & Nutrition Press (2003)
32. Brockhoff, P.B. and Christensen, R.H.B.: Thurstonian models for sensory discrimination tests as generalized linear models. Food Quality and Preference 21(3), 330-338 (2010)
33. Christensen, R. H. B. and Brockhoff, P. B.: sensR: An R-package for Thurstonian modelling of discrete sensory data. R-package version 1.2.5 (www.cran.r-project.org/package=sensR/) (2010)

34.Rayner, J.C.W., Best, D.J., Brockhoff, P.B. and Rayner, G.D.: Nonparametrics for Sensory Science: A More Informative Approach, Blackwell Publishing, USA (2005)
35.Brockhoff, P.B., Best, D.J. and Rayner, J.C.W.: Partitioning Anderson's statistic for tied data. Journal of Statistical Planning and Inference, 121, 93-111 (2004)
36.Best, D.J., Brockhoff, P.B. and Rayner, J.C.W.: An application of extended analysis for ranked data with ties. Australian & New Zealand Journal of Statistics. 46(2), 197-208 (2004)
37.Brockhoff, P.B., Best, D.J. and Rayner, J.C.W.: Using Anderson's statistic to compare distributions of consumer preference rankings. Journal of Sensory Studies 18, 77-82 (2003)
38.Best, D. J., Brockhoff, P. B., Rayner, J. W.: Test for balanced incomplete block ranked data with ties, Statistica Neerlandica., 60(1), 3-11 (2006)
39.Rayner, J.C.W., Best, D.J., Brockhoff, P.B. and Rayner, G.D.: Nonparametrics for Sensory Science: A More Informative Approach, Blackwell Publishing, USA (2005)
40.Christensen, R.H.B. Cleaver, G. and Brockhoff, P.B.: Statistical and Thurstonian models for the A-not A protocol with and without sureness, Food Quality and Preference (2011).
41. Christensen, R. H. B.: ordinal: An R-package for Regression Models for Ordinal Data. R-package version 2011-12-15 (www.cran.r-project.org/package=ordinal/) (2010)
42.McEwan, J. A.: Preference mapping for product optimization. In T. Næs & E. Risvik (Eds.), Multivariate Analysis of Data in Sensory Science (Vol. 16 - Data handling in science and technology, pp. 71-102): Elsevier Science B.V (1996)
43.Erichsen, L. and Brockhoff, P.B.: An application of latent class random coefficient regression. Journal of Applied Mathematics and Decision Sciences, 8(4), 201-214 (2004)
44.Poulsen, C.S., Brockhoff, P.M.B. and Erichsen, L.: Heterogeneity in consumer preference data - a combined approach. Food Quality and Preference 8(5/6), 409-417 (1997)
45.Andersen, C.M., Bro, R. and Brockhoff, P.B.: Effect of sampling errors on predictions using replicated measurements, Journal of Chemometrics. 17, 1-9 (2003)
46.Martens, H., Hoy, M., Wise, B., Bro, R. and Brockhoff, P.B.: Pre-whitening of data by covariance-weighted pre-processing. Journal of Chemometrics 17(3),153-165 (2003)
47.Brockhoff, P.B.: Sensory Profile Average Data: Combining Mixed Model ANOVA with Measurement Error methodology. Food Quality and Preference 12(5-7), 413-426 (2001)
48.Lê, S., Husson, F.: SensoMineR: a package for sensory data analysis. Journal of Sensory Studies 23 (1), 14-25 (2008)

Meat Evaluation by RGB-to-spectrum Imaging

Joni Orava[1], Jussi Parkkinen[1], Markku Hauta-Kasari[1], Paula Hyvonen[2], and Atte von Wright[2]

[1] Department of Computer Science, University of Eastern Finland,
P.O. Box 111, 80101 Joensuu, Finland
[2]Department of Biosciences, University of Eastern Finland,
P.O. Box 1627, 70211 Kuopio, Finland
joni.orava,jussi.parkkinen,markku.hauta-kasari,paula.hyvonen,
atte.vonwright@uef.fi
http://www.uef.fi

Abstract. In this study a set of minced meat samples of differing age were imaged both by spectral imaging and by RGB imaging. Spectral imaging gives better information about the meat and it is used as a reference method for reconstructed spectral images. Hierarchical temporal clustering of the samples is made using normalized RGB image data, spectral image data and reconstructed spectral image data. Bacterium concentrations are also specified for the samples, and the correlation between bacterium concentrations and image data are defined. Recommendations for imaging procedure and usability of method are given.

Keywords: Spectral imaging, spectral estimation, meat spoilage

1 Introduction

In food industry, it is important to know when a product is perished. Usually food producers set a shelf life for their products, which depends strongly on storage conditions. This shelf life is only a normative minimum time for the real preservability. Many products can be used also after their sell-by date. It is obvious that shelf life can not be extended without ensuring somehow the quality of the product. However, the traditional measurements of bacterium quantities are very complicated and time-consuming procedures. Thus, a need for new efficient methods for measuring food quality is existing.

In this research, a new method for measuring the quality of minced meat is demonstrated. It is well known that the color of meat changes as a function of storage time. Redness of meat is caused by myoglobin and its different forms, such as oxymyoglobin and metmyoglobin, which all have different spectral absorbances [1]. Our method is based on measuring the spectral properties of meat in visible and near-infra-red wavelength range. There are earlier studies also in which the quality of meat is evaluated using spectral imaging, but these studies do not concern perishing [2–4]. In our study, the correlation between the spectral changes and the changes in different bacteria quantities are determined. Measuring of spectral properties of meat samples are accomplished using spectral

camera. Spectral cameras are very expensive and demand usually professional users. However, if a training set containing the spectral properties of minced meat samples is available, also a basic digital camera with three color channels (RGB) can be used for the evaluation of spectral properties. In our study we are using Wiener estimation for spectral reconstruction [5, 6].

2 Experimental

In this study, 18 industrially produced and packaged minced meat samples (beef) were provided. Each sample (400 g) was packaged in protective gas atmosphere, which gives eight days shelf life for meat, if cold chain in maintained. Samples were transferred to measurements about 24 hours after mincing, without cold-chain being broken. After that, three packages were opened, and small samples were taken from each of them to bacterium assay. All three opened packages were also imaged by digital camera (RGB) and spectral camera. After imaging, the packaged were abandoned. Remaining 15 packages were contained in 15 degrees Celsius, and three of them were opened and analyzed at the time according to Table 1.

Table 1. Containing times of packages.

Sample number	Containing time [hours]
1-3	0
4-6	24
7-9	48
10-12	72
13-15	96
16-18	144

In bacterium assay, four different micro-biological concentrations (colony forming unit/g) were defined, that are aerobic mesofilic micro-organisms, coliform bacteria, *Escherichia Coli* bacteria and lactic acid bacteria, according to ISO standard methods (see Table 2 in Results-section). Also the visual appearance and smell were evaluated by five people for samples 1-3, 10-12 and 16-18 (grades from 0 to 5, 0=bad 5=excellent).

The samples were imaged in a dark room with 45/0 geometry. RGB images were taken by Nikon D90 digital camera. Spectral images were taken by CRI Nuance EX spectral camera in a wavelength range 450-950 nm with 20 nm intervals, totalling 26 wavelength bands. The same optics (Nikkor 60 mm macro) was used with both cameras. 50 W halogen lamp was used as a light source. White balance card were used as white reference for calibration of both cameras.

Spectral reconstruction of images were made using Wiener estimation with second degree terms [5, 6]. The training set were collected by manually choosing

36 spectrally different areas covering about 20 x 20 pixels from images 1, 4, 7, 10, 13 and 16, and by calculating component-wise median spectra for them. These median spectra and the normalized RGB values from corresponding areas were used to calculate the estimation matrix. RGB values were linearized by using standard gamma of 2.4, and normalized by dividing the linear RGB values by the corresponding values of the white reference.

Hierarchical clustering of samples was made using Ward's algorithm [7]. At first, the real spectral, reconstructed spectral and RGB images were aligned so that the pixels to be selected would cover the same region. Median spectra from the central part (200 x 200) of the spectral and reconstructed spectral images were calculated (region of interest, later referred as ROI). The second derivative of the median spectra were used for clustering to reveal the peaks of the data and also to correct the baseline. For RGB images, the median RGB values (component-wise) were used for clustering. Finally each image set was clustered in six clusters.

3 Results

The results of the bacterium assay are collected to table 2. The concentration definitions of aerobic mesofilic micro-organisms and lactid acid bacteria failed for sample 18.

Table 2. Microbiological and sensory results

Sample number	Mesof. micro-org. [cfu/g]	Coliformic bact. [cfu/g]	E. Coli bact. [cfu/g]	Lactic acid bact. [cfu/g]	Visual app. [0-5]	Smell [0-5]
1	8×10^2	< 100	< 100	< 100	5	5
2	6.5×10^2	< 100	< 100	< 100	5	5
3	9×10^2	< 100	< 100	50	5	5
4	21×10^2	< 100	< 100	53×10^2		
5	13×10^2	< 100	< 100	35×10^2		
6	28×10^2	< 100	< 100	64×10^2		
7	27×10^4	< 100	< 100	125×10^4		
8	29×10^4	750	< 100	94×10^4		
9	33×10^4	< 100	< 100	112×10^4		
10	65×10^5	1300	< 100	10×10^6	2.5	1.75
11	74×10^5	< 100	< 100	10×10^6	2.5	1.75
12	93×10^5	< 100	< 100	10×10^6	3.25	2.25
13	104×10^6	26×10^4	< 100	11×10^6		
14	90×10^6	7×10^4	< 100	11×10^6		
15	95×10^6	$< 1 \times 10^4$	< 100	12×10^6		
16	61×10^7	49×10^4	< 100	41×10^7	0	1
17	60×10^7	3×10^4	< 100	42×10^6	0	0
18	no result	$< 1 \times 10^4$	< 100	no result	0	1

It can been seen from Table 2 that all bacterium concentrations expect *Escherichia coli* bacteria increase somewhat exponentially with respect to containing time.

The median spectra of ROI for images 1, 4, 7, 10, 13 and 16 are showed in Figure 1. It can be seen that overall brightness levels varies slightly which is mainly caused by imaging geometry variations between samples. Especially sample 4 seems to be brighter than others. However, it can be seen that the main differences in spectral shapes are at wavelengths from 530 to 580 nm and at 630 nm. These are also the absorption peaks of oxymyoglobin and metmyoglobin, respectively [1]. Spectral shapes indicate clearly that the concentration of oxymyoglobin decreases and correspondingly metmyoglobin increases when containing time is extended.

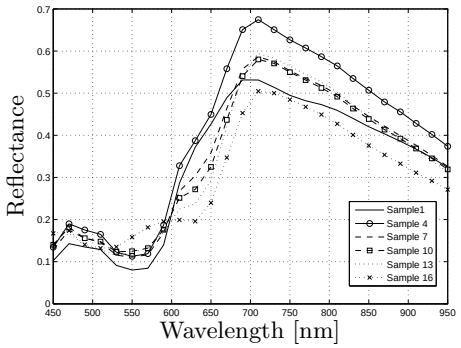

Fig. 1. Median spectral reflectance of samples 1, 4, 7, 10, 13 and 16.

Results of spectral reconstruction can be seen in Figure 2. It can be seen from the figure that the shape of the reconstructed spectra correspond well to real spectra, although small differences can be observed.

RGB-images, spectral images and reconstructed spectral images were clustered into six clusters using hierarchical clustering. Ideally, images should form clusters in daily basis, i.e. three images per day in correct temporal order. The results are collected to Table 3. It can be seen that clustering result for spectral data is perfect. RGB-data performs very poorly. A few reconstructed spectral images are located to neighboring cluster, others being perfectly clustered.

Because the absorbances of certain wavelength bands seem to vary temporally due to oxymyoglobin changing to metmyoglobin, the changes in quotients of reflectance channels 570 and 630 nm are computed. For comparison, the change in quotient of normalized green and red channel from the RGB images are also computed. Results are shown in Figure 3. Scales in the figure are logarithmic.

Clearly, the correlation is the best with real spectral data. It can also be seen that reconstructed spectral data outperforms RGB data, while it still is too inaccurate for the evaluation of containing time or bacterium concentration.

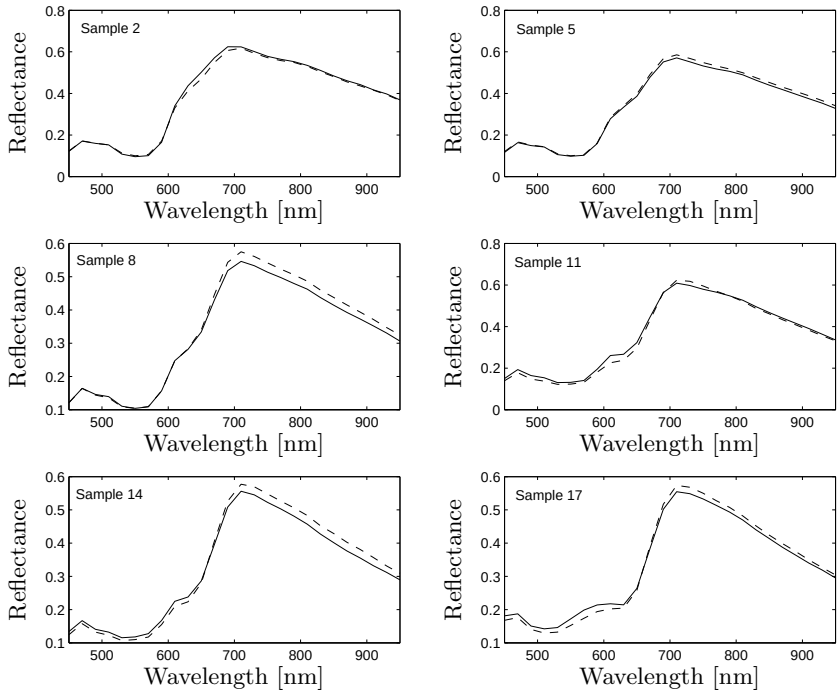

Fig. 2. Median spectra (continuous line) and reconstructed median spectra (dashed line) of samples 2, 5, 8, 11, 14 and 17.

Table 3. Clustering results for different image sets.

Image set	Images in the correct cluster	Images in the adjacent cluster
RGB	8	5
Spectral	18	0
Reconstructed spectral	14	4

4 Conclusions

The study demonstrated a new method for temporal classification of minced meat. 18 minced meat samples, which were contained in raised temperature (15 ^{0}C) were imaged both by spectral and RGB camera during six days, three samples at a time. Spectral images were reconstructed from RGB images using Wiener estimation. For images taken by a spectral camera, the clustering results were perfect. Also reconstructed spectral data outperformed clearly the pure RGB data. Two critical absorption peaks (about 570 nm and 630 nm) were found from the spectral data, which is related to different forms of myoglobin.

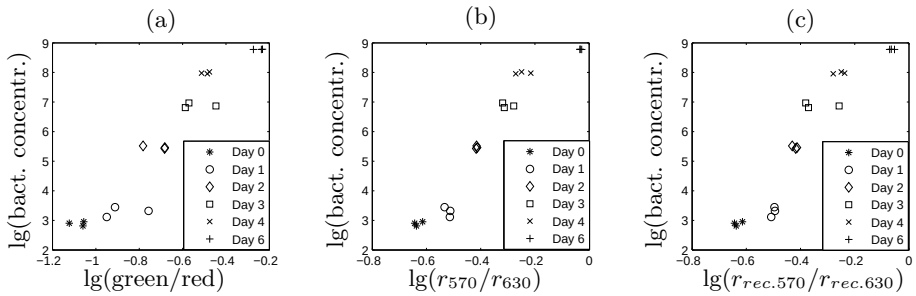

Fig. 3. Correlations between bacteria concentration (Mesofilic aerobic microorganisms) and (a) normalized green to red quotient (b) 570 nm to 630 quotient (spectral data) (c) 570 nm to 630 nm quotient (reconstructed spectral data).

By comparing the proportions of the reflectances on above wavelengths, the containing time of the meat sample can be predicted.

Acknowledgments. We sincerely appreciate HKScan Corporation for providing samples for this research.

References

1. Bowen, W. J.: The Absorption Spectra and Extinction Coefficients of Myoglobin. J. Biol. Chem. 179, 235–245 (1949)
2. Qiao, J., Wang, N., Ngadi, M. O., Gunenc, A., Monroy, M., Gariépy C., Prasher, S.O.: Prediction of drip-loss, pH, and color for pork using a hyperspectral imaging technique. J. Meat. Sci. 76, 1–8 (2007)
3. Qiao, J., Ngadi, M. O., Wang, N., Gariépy C., Prasher, S.O.: Pork quality and marbling level assessment using a hyperspectral imaging system. J. Food. Eng. 83, 10–16 (2007)
4. Liu, L., Ngadi, M. O., Prasher, S.O., Gariépy C.: Categorization of pork quality using Gabor filter-based hyperspectral imaging technology. J. Food. Eng. 99, 284–293 (2010)
5. Tsumura, N., Sato, H., Hasegawa, T., Haneishi, H., Miyake, Y.:Limitation of Color Samples for Spectral Estimation from Sensor Responses in Fine Art Painting. Opt. Rev. 6, 57–61 (1999)
6. Stigell, P., Miyata, K., Hauta-Kasari, M.:Wiener Estimation Method in Estimating of Spectral Reflectance from RGB Images. PRIA. 17, 233–242 (2007)
7. Ward, J. H.: Hierarchical Grouping to optimize an objective function. J. Amer. Statistical Assoc. 58, 236–244 (1963).

Design of characteristics of optical filter set for prediction and visualization of fat content in raw beef cuts

Ken-ichi Kobayashi[1], Ken Nishino[1], Bjørn Skovlund Dissing[2], Masaaki Mori[3], Toshihiro Toyota[1], and Shigeki Nakauchi[1]

[1] Department of Computer Sciences, Toyohashi University of Technology, 1-1 Hibarigaoka, Tenpaku-cho, Toyohashi 441-8580, Japan
{kobayashi09,nishino06,toyota}@vpac.cs.tut.ac.jp,nakauchi@tut.jp
http://www.vpac.cs.tut.ac.jp/
[2] Department of Informatics and Mathematical Modelling, Technical University of Denmark, DK-2800 Lyngby, Denmark
bdi@imm.dtu.dk
[3] Mie Prefecture Livestock Research Institute, 1444-1 Ureshino-cho, Matsusaka 515-2324, Japan
morim05@pref.mie.jp

Abstract. Quantification of specific compounds in a food-matrix is a very important factor for an overall quantification of the quality. Near infrared (NIR) hyperspectral imaging is a powerful technique to quantify specific constituents as well as its spatial distribution of the food-matrix. Hyperspectral imaging is however very expensive. We propose a way to design a simple measurement system consisting of a NIR sensitive monochrome camera together with a small set of optical filters to estimate and visualize a specific food compound without requiring a full hyperspectral device. Based on a set of hyperspectral measurements of beef and physical and chemical analysis of the fat within the beef, we propose a method to design a set of ideal Band Pass Filters (BPF), as small as possible while still maintaining predictability of fat content. The results show that 2 filters is a suitable amount of filters for prediction.

Keywords: NIR hyperspectral imaging, Optical filter, Beef, Content

1 Introduction

Traditionally quality evaluation of food has been done using visual inspection, chemical measurements or sensory testing. These methods are destructive, time-consuming and/or subjective, which calls for other quantification methods. Recently non-destructive methods for evaluation of food quality as well as visualization of the spatial distribution of constituents, by using (NIR) hyperspectral information have emerged [1]. Although hyperspectral image data is very versatile and contains much information, the measurement system is extremely expensive to install in a food factory. As another approach based on hyperspectral data, a method designing the optical transmission for the optical filter to modulate a

RGB camera's spectral sensitivity and to highlight an object's spectral features is proposed [2][3].

We propose a simple measurement system consisting of a NIR monochrome camera together with a small set of optical filters to estimate and visualize a specific food compound without use of a hyperspectral device. We use the fat content in raw beef as the target. Currently in Japan, the quality evaluation of beef carcasses is performed manually by a grader. In this grading, only visual inspection is used. Marbling, which is the amount and distribution of fat in the meat is the most important factor. Based on a set of hyperspectral measurements and physical and chemical analysis of fat within the beef, we propose a method to design a set of optical Filters, which accurately is able to predict the amount and distribution of this fat.

2 Materials and methods

2.1 Samples and measurements

A total of 126 meat samples consisting of various parts from three 25-month-old Japanese black cattle were collected. After about 60 days of ageing at $0-5°\mathrm{C}$, the beef carcasses were kept at $-25°\mathrm{C}$ to maintain the fat properties during storage and transportation.

The fat content used for reference values was analyzed by physical and chemical method. Automated Soxhlet extraction equipment (Soxtherm416, Gerhardt, Germany) was used to obtain the fat percentage.

The hyperspectral measurements were performed by a NIR hyperspectral imaging system consisting of a linear image sensor (Spectral Camera SWIR; SPECIM Spectral Imaging Ltd, Finland), a linear slide table and halogen light sources (MH-M15, 150 W; Hataya Ltd, Japan). The hyperspectral camera works in the wavelength range of 970-2500 nm with a bandwidth of 6.3 nm at a resolution of 320 pixels (X-axis). We acquired samples at a resolution of $380\mu m/pixel$ over a rectangular region of $120\times130mm$ by moving the slide table. The exposure time was 3.0 ms.

2.2 Calculation of filter transmission intensity

The MATLAB 7.5 (R2007b; The MathWorks Inc., Natick, MA, USA) software package was used to analyze the hyperspectral image data. Optical filters were designed as ideal (rectangle-shaped) BPF and an assumption was made that a measurement using an optical filter consists of three images; a dark current image (I_{Dark}), a white standard image (I_{White}) and a sample image (I_{Sample}). To remove the effects of dark current, spectral features produced by the light source, and flat field inhomogeneities, we use I_R as a model parameter calculated from measured images or hyperspectral images by

$$I_R = \frac{I_{Sample} - I_{Dark}}{I_{White} - I_{Dark}} = \int_{\lambda_{short}}^{\lambda_{long}} \frac{I_{Sample}(\lambda) - I_{Dark}}{I_{White}(\lambda) - I_{Dark}} d\lambda$$

Where $\{I_{Dark}, I_{White}(\lambda), I_{Sample}(\lambda)\}$ is hyperspectral data, λ_{short} and λ_{long} are the wavelength edges of the BPF. When calculating I_R , the spectra $\{$ $I_{Sample}(\lambda), I_{White}(\lambda)$ $\}$ were interpolated by cubic spline to 1,000 wavelength points between λ_{short} and λ_{long} .

2.3 Design of optical filter property

The filter properties were modeled by using the center wavelength (λ_c) and the half-bandwidth (w_h). We limited the minimum bandwidth of BPF to 50 nm, because too narrow BPFs cannot obtain enough luminance, which will cause reduction of the signal-to-noise ratio. The maximum bandwidth was limited to 1,000 nm, because very wide BPFs are hard to implement as a real optical filter. The wavelength range was also limited from 1,000 nm to 2,300 nm, because shorter/longer wavelength ranges of hyperspectral data could not provide sufficient intensity. With a spectral resolution of about 6.3 nm, meaning a total number of wavelength-points of 206. Even if the edges of BPFs are limited to these wavelength-points, every possible combination of n BPFs is $\simeq 10^{4n}$. Therefore "brute-force search" is not suitable for more than 2 or 3 filters in terms of searching time.

Multiple Linear Regression (MLR) was used to estimate parameters for linear models using filter transmission intensities as variables. To create and evaluate the estimation models, samples were divided into calibration and validation sets. Calibration samples were selected randomly ($N_c = 84$) and remainder were used as validation samples ($N_v = 42$). These sample sets were fixed to compare the results of different feature selection method.

Filter feature selections were done using leave-one-out cross validation, to minimize the root mean square error of cross-validation ($RMSECV$) given by

$$RMSECV = \sqrt{\frac{\sum (y_c - \widetilde{y}_c)^2}{N_c}}$$

where y_c is the reference value, and $\widetilde{y_c}$ is the predicted value of the calibration-set in cross validation. Furthermore the standard error of calibration (SEC) , the root mean square error of calibration ($RMSE_c$) and the standard error of prediction (SEP) were calculated as

$$SEC = \sqrt{\frac{\sum (y_c - \hat{y}_c)^2}{N_c - n - 1}}, \quad RMSE_c = \sqrt{\frac{\sum (y_c - \hat{y}_c)^2}{N_c}}, \quad SEP = \sqrt{\frac{\sum (y_v - \hat{y}_v)^2}{N_v}}$$

where $\hat{y}_c$ is the predicted value of the calibration-set using the model, n is the number of filters, y_v is the reference value of the validation-set, and $\hat{y_v}$ is the predicted value of the validation-set using the model.

We compared the following three feature selection methods.

Stepwise random selection In this method one needs to define the number of filters. A scoremap and a countmap is maintained for each filter which is used for deciding the final properties for the corresponding filter:

1. Generate the $\{m, (m+1), (m+2), ..., n\}$-th filters randomly.
2. Calculate n filter outputs of each calibration sample.
3. Make a MLR model by using the calculated filter outputs and the corresponding reference values of the calibration-set.
4. Calculate the RMSECV for the calibration-set.
5. Add the RMSECV value to the n points in the scoremap. Also add 1 to the n points in the countmap.

6. Repeat step 1 to 5 sufficiently many times.

The scoremaps and the countmaps are made for each m-th filter individually, and have coordinate points corresponding to every filter feature (λ_c, w_h).

7. Remove 0-count points both in the m-th countmap and the m-th scoremaps. Then make a mean scoremap by dividing the m-th scoremap by the m-th countmap.
8. Choose a point that minimizes the mean scoremap. This is then fixed as the m-th filter (λ_{c_m}, w_{h_m})
9. Repeat steps 1 to 8 n times with the $\{1, 2, ..., (m-1)\}$-th fixed filters.

Finally, local optimization (constrained nonlinear optimization) is performed using the result as a starting guess, minimizes

$$min \left(\sqrt{\frac{\sum_i^{N_c} (y_i - \sum_j^n f(\lambda_{short}(j), \lambda_{long}(j), x_i))^2}{N_c}} \right), f(\lambda_{short}, \lambda_{long}, x) = \int_{\lambda_{short}}^{\lambda_{long}} x d\lambda$$
$$s.t. \quad (1000 \leq \lambda_{short}, \lambda_{long} \leq 2300), \quad (50 \leq \lambda_{long} - \lambda_{short} \leq 1000)$$

where x is reflectance (hyperspectral data) of a sample. In this method, a filter feature which has small average error in many trials of various feature combinations, is assumed to contain useful information for estimation.

Forward selection method Inspired by the classic variable selection technique also known as forward selection [4], the forward selection method calculates $RMSECV$ for all possible filters and selects the filter (λ_{C_1}, w_{h_1}) which minimizes this metric. This filter (λ_{C_1}, w_{h_1}) is fixed at the found feature and the procedure is then repeated for next filter (λ_{C_2}, w_{h_2}) . The m-th filter (λ_{C_m}, w_{h_m}) is chosen with $(m-1)$ fixed filters. The wavelength of the BPF edges are discrete values.

At the m-th filter selection step, this method consider the combination of $(m-1)$ filters already fixed and m-th filter. Contrary to this the stepwise random selection method considers the combination of n filters at every step.

Forward selection with local optimization After each forward selection step, local optimization (same to stepwise random selection method) is performed using the result of the forward selection method as a starting guess.

3 Results and discussion

Table 1 shows the statistics of results for the calibration and validation samples found by the physical and chemical analyses. The samples have a rather wide distribution.

Table 1. Statistics for reference values in each data set

	Number	Mean[%]	SD[%]	Min[%]	Max[%]
Entire set	126	30.92	14.66	5.25	71.23
Calibration set	84	30.36	13.99	5.25	63.50
Validation set	42	32.04	16.03	8.98	71.23

Figure 1 shows an example of the result of stepwise random selection for n=6 with the area-averaged reflectance spectra from all 126 samples. The number of

repetitions for each selection step is 10^5. Figure 3 shows the mean scoremaps. The minimum point (the selected condition) is indicated by a magenta mark in each of the maps. Figure 2 shows an example of the plot of the evaluation values for n= 1 to 10. In this result, local optimization decreases the $RMSECV$, and increases the SEP .

Figure 4 shows the result of the forward selection method, while figure 5 shows a plot of the evaluation values. Although the $RMSE_c$ continues to decrease at least until 10 filters, the SEP begin to increase after 6 filters, and the $RMSECV$ is not improved after 3 filters. Also the 4-7th filter is exactly similar, it's impractical to implement a real optical filter individually.

Figure 6 shows the modifications achieved by local optimization after each forward selection step. It appears that there are few or no modifications. Figure 7 shows a plot of the evaluation values. Local optimization decreases the $RMSECV$ slightly, however the SEP is increased. This might indicate that the local optimization causes overfitting.

In summary, local optimization decreases the $RMSECV$, however, it does not necessarily mean the model's accuracy improves. In this case, 2 filters might be enough for prediction.

In previous work [1], which uses hyperspectral data and PLS1 regression, the SEP is 4.81. In that study, spectral correction (multiplicative scatter correction) was used. Because the purpose is to implement a real optical filter, we use raw reflectance spectra without any spectral correction. We achieve a minimum SEP around 5.0. This could indicate that our results demonstrate sufficient accuracy.

In this study, similar $RMSECV$ curves but different SEP curves are obtained. Accuracy has not improved even we increase the number of filters to more than 2. This might mean that the prediction of the fat content is rather easy, because it was high in fat.

In future work, we will apply these methods to the estimation of fatty acid content, which is more difficult to predict than fat content because the content is much lower. Also, we will apply imaging to visualize the food composition. To improve the accuracy, we will add a combination of filter output values to the estimation model, and perform selection of them.

References

1. Kobayashi, K., Matsui, Y., Maebuchi, Y., Toyota, T., Nakauchi, S.: Near infrared spectroscopy and hyperspectral imaging for prediction and visualisation of fat and fatty acid content in intact raw beef cuts. J. Near Infrared Spectrosc.,18,301–315(2010)
2. Nishino, K., Nakamura, M., Matsumoto, M., Tanno, O., Nakauchi, S.: Optical Filter for Highlighting Spectral Features Part I: Design and Development of the Filter for Discrimination of Human Skin With and Without an Application of Cosmetic Foundation. Optics Express, 19, 6020–6030(2011)
3. Nishino, K., Nakamura, M., Matsumoto, M., Tanno, O., Nakauchi, S.: Optical Filter Highlighting Spectral Features Part II: Quantitative Measurements of Cosmetic Foundation and Assessment of their Spatial Distributions under Realistic Facial Conditions. Optics Express, 19, 6031–6041(2011)
4. Wilkinson, L., Dallal, G.E.: Tests of significance in forward selection regression with an F-to enter stopping rule. Technometrics.,23,377–380(1981)

6

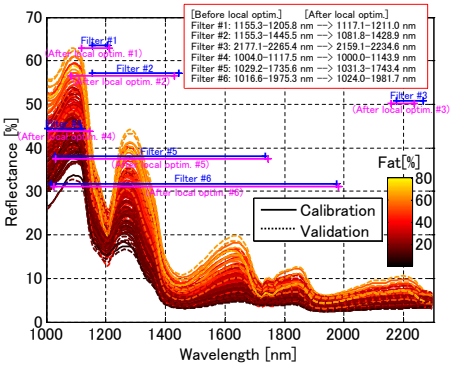

Fig. 1. An example of the result of stepwise random selection (n = 6)

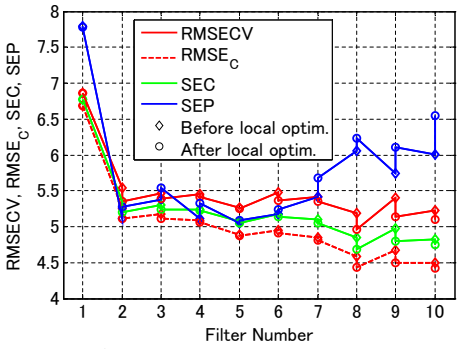

Fig. 2. An example of individual error measures (for n=1-10) for stepwise random selection

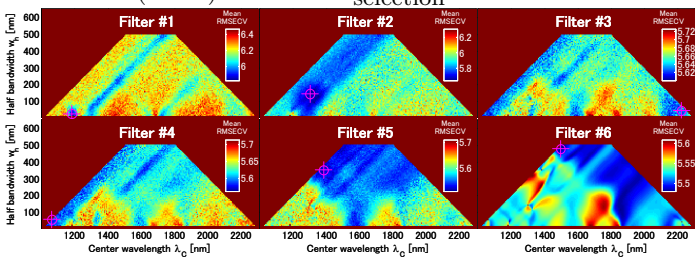

Fig. 3. An example of an evaluation map of stepwise random selection (n = 6)

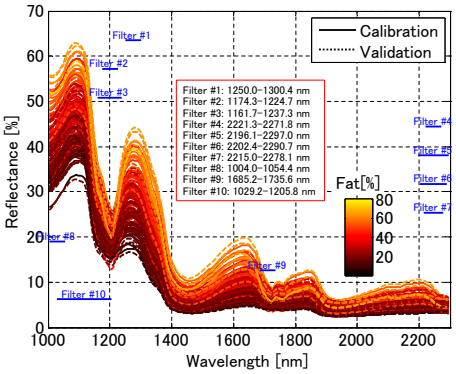

Fig. 4. The result of forward selection (n=10)

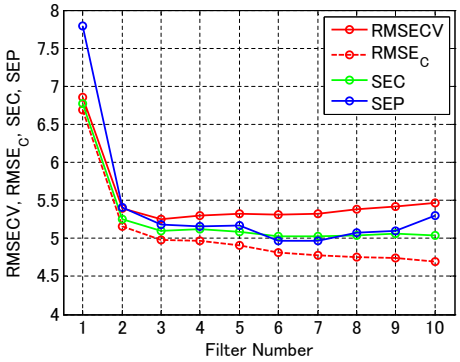

Fig. 5. Error measures for forward selection

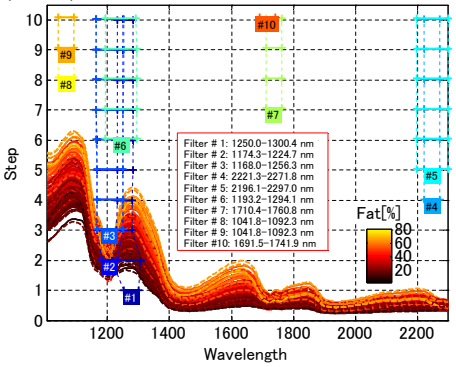

Fig. 6. Modifications of the BPFs found by local optimization after each forward selection step (n=1-10)

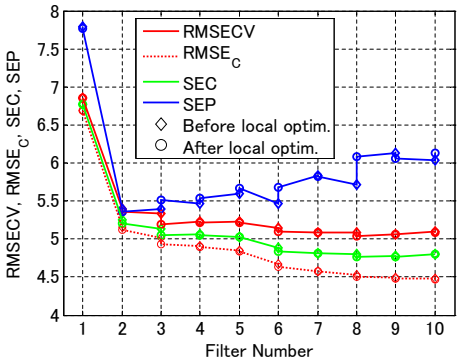

Fig. 7. Error measures for forward selection with local optimization

In Depth Analysis of Food Structures
Hyperspectral Subsurface Laser Scattering

Otto Højager Attermann Nielsen[1], Anders Lindbjerg Dahl[1], Rasmus Larsen[1], Flemming Møller[2], Frederik Donbæk Nielsen[3], Carsten L. Thomsen[3], Henrik Aanæs[1] and Jens Michael Carstensen[1]

[1]DTU Informatics, Technical University of Denmark
[2] DANISCO A/S, [3] NKT Photonics A/S

Abstract. In this paper we describe a computer vision system based on SLS (Subsurface Laser Scattering) for industrial food inspection. To obtain high and uniform quality, in for example dairy products like yoghurt and cheese, it is important to monitor the change in size and shape of microscopic particles over time. In this paper we demonstrate the usefulness of our SLS system for characterizing food items. We use a laser source that can be tuned to any wavelength in the range of 455 nm - 1020 nm by applying an AOTF (Acousto-Optical Tunable Filter) to an optical beam generated by a SuperK (supercontinuum) laser system. In our experiments we show how the system can be used for discriminating dairy products with different structure and how the structural change of a foam can be monitored over time. Time stability of the system is essential for measurements over several hours, and we demonstrate the time stability by measuring the reflectance profile of an inorganic phantom. The SLS technique is a very promising technique for non-intrusive food inspection, especially for homogenous products where particle size and shape are important parameters.

1 Introduction

The purpose of this paper is to present results of our computer vision system for characterizing structural elements in food products. The development of microstructures is important in the production of for example fermented dairy products. Controlling this development, which can take hours or days, is essential for obtaining high quality products while minimizing energy consumption and waist. Our system is based on a supercontinuum (SuperK[1]) laser source that uses an AOTF (Acusto-Optic Tunable Filter) to produce a beam with a precise wavelength that can be tuned over a broad range. The laser system delivers the light through a photonic crystal fiber that is integrated with a camera as illustrated in Figure 1. Based on this system we are able to perform hyperspectral SLS (Sub-surface Laser Scattering) measurements of various food samples. Our SLS system has high potential for becoming an integral part of product development and production, because it provides non-intrusive and objective assessment

[1] http://www.nktphotonics.com/

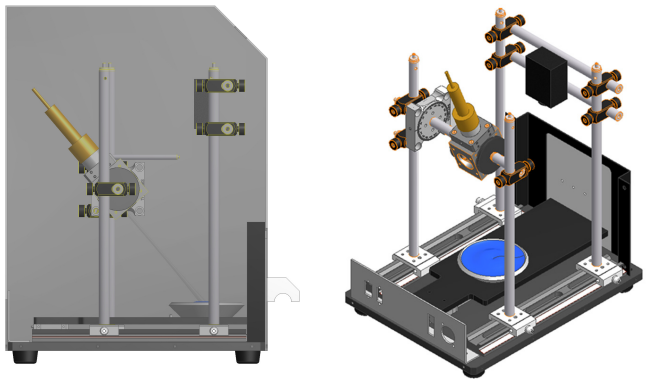

(a) Side view of the hyperspectral SLS vision system.

(b) 3D illustration of the hyperspectral SLS vision system.

Fig. 1. Illustration of the vision systems. In (a) the system is shown from the side where the laser source is at the left side pointing at the sample. The instrument mounted on the right side is the camera. The gray shade behind is the cover, which protects the setup from surrounding light. In (b) the same setup is illustrated from an angle without the cover. Both the laser source and the camera is mounted in a flexible setup that can be adjusted to various positions and angles.

of structure of the food item. Food structure can be coupled to parameters like mouth feel and creaminess [1].

Many food items are processed to change their structure. Protein structure of milk changes by fermentation from being dissociated to form chains. In a whipping process air bobbles are added to the food. Methods like rheology, microscopy and spectroscopy are traditionally used for measuring such changes [3]. The advantage of a vision systems, like our SLS system, is the avoidance of contact with the food and the possibility of implementing an inline application [7]. We will demonstrate how this variation in structural composition can be assessed using our SLS system.

2 Method

We have presented the setup for hyperspectral SLS in [6], and we are continuously developing the system for food inspection problems. The setup is shown in Figure 1, and from the results presented in [6] we have extended the procedure to include improved image acquisition using high dynamic range imaging (HDR). We also demonstrate the time stability of the system and how a process can be monitored over time.

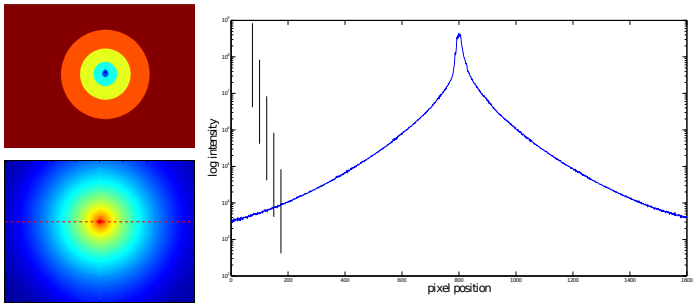

Fig. 2. Building a HDR image. Top left shows a mask used for building the HDR image. The mask with the dark blue color in the center is used as a mask for the image with the shortest exposure time, and the other masks are used with longer and longer exposure times. For each mask the pixel value of the image is divided by the corresponding exposure time. Bottom left shows the HDR image on a log scale, with the highest intensity in the center red part and lowest in the blue parts. Right is a graph of the profile along the dotted line. The vertical lines show the dynamic range of the five differently exposed images for building this HDR image.

2.1 High dynamic range imaging

The subsurface scattering profiles are highly divergent and cannot be covered by the effective dynamic range of the camera. Acquiring images at a number of exposures can solve this, but this will result in large amounts of data to be stored. To overcome this we construct a HDR image. For now we have chosen a simple approach for constructing HDR images by acquiring images with different shutter time and using the shutter time as a multiplicative factor. This approach is illustrated in Figure 2.

An image can contain pixels that are under exposed, well exposed or over exposed or a combination of these. The problem is to combine the well-exposed pixels over all images. We make the simplifying assumption that the image intensity scales linearly with exposure time, which can be expressed as $\mathbf{I}(t) = t\mathbf{I}_n$, where $\mathbf{I}$ is the image, t is the exposure time, n is the number of images and $\mathbf{I}_n$ is the image acquired with the shortest exposure time.

The HDR image is constructed by choosing the pixels from the image with highest signal to noise ratio. The image acquisition results in a stack of images, where the intensity of the pixels increases with increasing exposure time. Assuming the pixel noise to be independent of the exposure time, we will have highest signal to noise ratio for a pixel in the image with the longest exposure time, where that pixel is still not saturated. Therefore, we construct our HDR image by starting with the image acquired with the longest exposure time and choosing all non-saturated pixels. After that we choose the image with the second longest exposure time, and add all the unsaturated pixels that was not chosen until now, multiplied with a factor $\tau_i = \frac{t_1}{t_i}$, where $i = 2$ for the second image. We continue

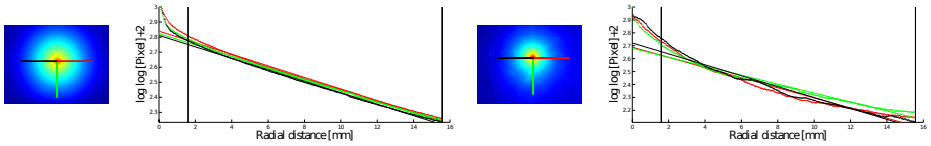

Fig. 3. Characterization of two samples – (*left*) a phantom and (*right*) a whipped cream foam. The HDR image shows the three profiles marked with a black (*backward scattering*), a red (*forward scattering*) and a green line(*orthogonal profile*). The sample is illuminated from the left. The iterated logarithm of the intensity is shown in the three curves colored similar to the profiles in the image, and the straight lines are the fitted curves. The model is only partly applicable and the vertical line shows the minimum radial distance for the fit.

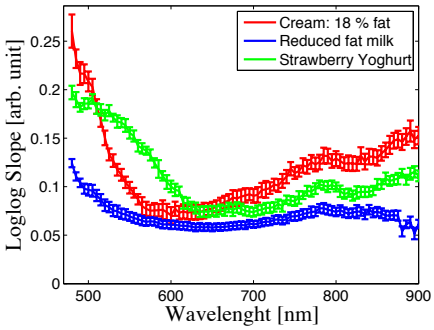

Fig. 4. Iterated logarithmic characterization as a function of wavelength for various products. The primary difference between cream and milk is the content of fat globules, and the primary difference between milk and yoghurt is the fermentation where protein structures change due to acidification. Both these differences are clearly distinguishable from the SLS characterization. The error bars are error on the slope estimate of the iterated logarithm.

this way until all images are added. If the image with the shortest exposure time contains saturated pixels, these are added to the final HDR image.

2.2 Sample characterization

The iterated logarithm of the intensity ($\log(\log(\mathbf{I}))$) presented in [2] and [6] was used for analyzing the scattering distribution. We have extended the number of profiles through the image since an oblique incident of 45° illumination was used. The oblique illumination results in a anisotropic shape of the intensity peak. Mie-theory predicts a symmetric scattering profile orthogonal to the direction of the incoming light, which has been verified in [5]. Based on this we have extended the characterization using three profiles all starting from the intensity peak – two in the incident direction of the beam and one perpendicular to this. This way we capture some of the anisotropy in the scattering distribution. This is

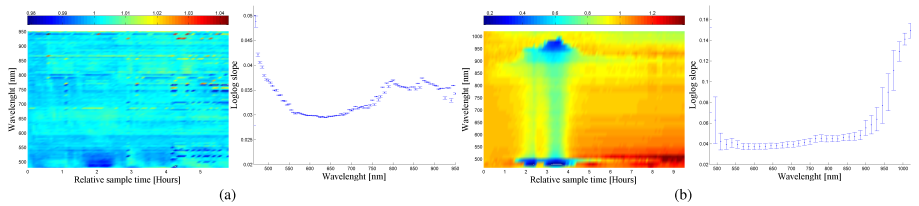

Fig. 5. Development of the SLS characterization over time. (a) time development of a phantom object and (b) time development of whipped cream. Left the SLS characterization (normalized) is shown as an image and right the average SLS parameter with error bars of one standard deviation. The phantom has almost no change over time, showing that the system is very stable, whereas the whipped cream changes significantly.

illustrated in Figure 3. But the resulting characterization based on the slope and offset of the fitted curve was very similar, so in the rest of this paper we just use the average of the three profiles.

3 Experiment and results

We have performed experiments to demonstrate how the system can be used for assessing changes over time. In Figure 4 this is shown for some commercially available dairy products, which shows that for most wavelengths there is a clear difference in their characterization. The fermentation of milk to form yoghurt changes the shape of the SLS parameter significantly.

3.1 Monitoring the time development of the scattering profile

To estimate the system stability we have measured the SLS profile of a phantom. The phantom is solid block containing polystyrene spheres made similar to the description in [4]. We measured the phantom over 5 hours and 50 minutes with wavelengths ranging from 460 nm to 1020 nm. In a similar way we measured the development of whipped cream, which is foam that changes structure over time. Scattering parameters of both phantom and whipped cream are presented in Figure 5. The measurements of the phantom are stable over time with minor variations due to noise in the measurements, whereas the whipped cream clearly changes with time as the foam collapses.

4 Discussion and conclusion

The main contributions of this paper is the demonstration of the SLS system for time studies and a HDR imaging for improved SLS characterization. The anisotropic shape of the scattering center is also characteristic for the food items. Our characterization, based on the linear fit of the iterated logarithm,

did not show the expected directional dependence, but using the anisotropy is very promising for future research.

The HDR imaging improves characterization, because the entire dynamic range is captured making it possible to measure the entire reflectance profile. This allows the SLS parameters to be estimated from a larger number of pixels and a much higher dynamic range, than using just one exposure. In addition we obtain a good characterization also in regions where the camera sensitivity or beam power is very low or very high. Images based on a single exposure would have a risk of being under or over exposed. Our procedure for building the HDR images also ensures a selection of the pixels with highest signal to noise ratio while being simple and fast.

Our SLS system is highly flexible because it offers a high spectral resolution and a high variation in geometric configuration. This makes it a unique instrument for SLS characteristics of food items, and our research will focus on finding combined radiometric and geometric configurations that optimally characterizes the food sample. From this we will be able to design a new type of vision systems for improved food quality assessment.

5 Acknowledgements

This project was carried out in the Center for Imaging Food Quality supported by The Danish Council for Strategic Research[2].

References

1. M.C. Bourne. *Food texture and viscosity: concept and measurement*. Academic Pr, 2002.
2. J. M. Carstensen and F. Møller. Online monitoring of food processes using subsurface laser scattering. In *Advances in process analytics and control technologies (APACT 09), 2009, Glasgow, Scotland, May 5-7*, 2009.
3. P. Fischer and E. J. Windhab. Rheology of food materials. *Current Opinion in Colloid & Interface Science*, 2010.
4. G. Marquez and LH Wang. White light oblique incidence reflectometer for measuring absorption and reduced scattering spectra of tissue-like turbid media. *Opt. Express*, 1(13):454–460, 1997.
5. S. Menon, Q. Su, and R. Grobe. Determination of g and μ using multiply scattered light in turbid media. *Physical review letters*, 94(15):153904, 2005.
6. O. H. A. Nielsen, A. L. Dahl, R. Larsen, F. Møller, F. Donbæk, C. L. Thomsen, H. Aanæs, and J. M. Carstensen. Supercontinuum light sources for hyperspectral subsurface laser scattering - applications for food inspection. In 2011 Proceedings SCIA, editor, *Scandinavian Conference on Image Analysis, Ystad, Sweden, May 2011*, Lecture Notes in Computer Science. Springer, may 2011.
7. D. W. Sun. *Hyperspectral imaging for food quality analysis and control*. Academic Press, 2010.

[2] http://www.cifq.dk

Spectral Imaging by Upconversion

Jeppe Seidelin Dam[1], Christian Pedersen[1] and Peter Tidemand-Lichtenberg[1],

[1] DTU Fotonik, Deparment of Photonics Engineering, Frederiksborgvej 399,
4000 Roskilde, Denmark
jdam@fotonik.dtu.dk

Abstract. We present a method to obtain spectrally resolved images using upconversion. By this method an image is spectrally shifted from one spectral region to another wavelength. Since the process is spectrally sensitive it allows for a tailored spectral response. We believe this will allow standard silicon based cameras designed for visible/near infrared radiation to be used for spectral images in the mid infrared. This can lead to much lower costs for such imaging devices, and a better performance.

Keywords: Upconversion, spectral imaging.

1 Introduction

Imaging with spectral information has many potential applications. This includes medical imaging, cleantech, combustion analysis, and food imaging. Here we present how a new technology can be used to extend the working range of silicon based cameras far beyond their normal wavelength working range. This is done by upconversion, which is a process often used to convert the wavelength of lasers. This is for example used in green laser pointers where 2 near infrared laser photons at 1064 nm combine forming one green 532 nm photon with twice the energy. The same principle can be applied where two different wavelengths are mixed inside a nonlinear crystal, generating a third wavelength as the sum energy (or frequency, if you will). Under the right circumstances, this sum frequency generation will even be able to conserve image information existing at the input wavelengths. This process can even occur if one of the input wavelengths is incoherent light and the other a powerful laser.

Work on image upconversion was an active research field in the 1960's and 1970's. Around 1980 the field was abandoned, since the quantum efficiency (QE) of the process never exceeded $2 \cdot 10^{-7}$ and the obtained images had very low resolution not exceeding 20x20 image elements [1-7]. Recently [8], we demonstrated a vast increase in the Quantum efficiency and resolution obtainable in image upconversion.

[1] Please note that the LNCS Editorial assumes that all authors have used the western naming convention, with given names preceding surnames. This determines the structure of the names in the running heads and the author index.

In fact, we increased the QE by 1000 (to 0.02 %), and the amount of image elements by a factor 500 over previous work in the field (to 200x1000 image elements). This gives reason to believe that the process can be improved to be usable for many different applications, as pointed out in a News & Views story [9] about our previous work.

2 The experimental details

The working principle of our first image conversion module is illustrated in Fig. 1.

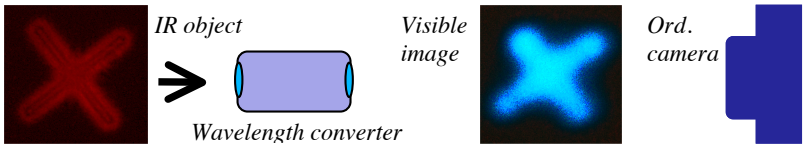

Fig. 1. The working principle of the image wavelength converter. Light from an infrared object is passing through a wavelength converter module which transforms the wavelength of the light to a new, shorter, wavelength. This wavelength can be captured by an ordinary camera.

Photons containing image information at a wavelength, λ1 are mixed with a laser with wavelength λ2, to form upconverted photons at the sum frequency, λ3. See Eq. 1.

$$\frac{1}{\lambda_1}+\frac{1}{\lambda_2}=\frac{1}{\lambda_3} \tag{1}$$

To obtain efficient conversion the phase matching condition must be satisfied. See eq. 2.

$$k_3 = k_1 + k_2 + K_{QPM} \tag{2}$$

k_i is the wavenumber of the photons, and K_{QPM} is the quasi phase matching parameter, which is $K_{QPM} = 2\pi/PP$, where *PP* is the poling period of the nonlinear crystal. Since the poling period can be designed to specifications, it is possible to design phase matching of any wavelengths, as long as the nonlinear crystal is transparent to the three involved wavelengths.

The module accepts radiation at one wavelength regime with image information, and converts that radiation to another wavelength. This wavelength-converted image has been spectrally filtered by the nonlinear process, and can be detected with a standard camera.

Details of the experimental setup can be found in reference [8]. The key ingredients are a nonlinear crystal placed within an intense laser field. The intense

laser beam is generated by setting up a resonant laser system (the laser photons are "recycled" passing through the crystal many times using an intra cavity set-up). This makes it possible to obtain very high laser powers, by use of a comparatively low power pumping laser. In the present setup the phasematched wavelength can be tuned either by tuning the temperature or other parameters in the phasematch condition. By choosing a suitable poling period any wavelength, for which the nonlinear crystal is transparent, can be upconverted.

Since the conversion efficiency is proportional to the laser power, the system optimized to provide maximimum intracavity laser power. This is done by minimizing the losses, by using laser mirrors with very high reflectivity. Furthermore the nonlinear crystal is inserted in the laser cavity at Brewster angle minimizing reflection losses. Since the Brewster angle is nearly identical for the incoming and the generated wavelength, the reflection losses are minimal.

3 Designing the bandwidth of the upconverter

In previous work we have demonstrated how very narrow or broad acceptance bandwidths can be obtained. Basically this is done by choosing the right combination of nonlinear crystal and mixing laser wavelength. We have designed a simple method to calculate how to optimize the phase match condition for broad band and narrow band upconversion respectively. The obtainable bandwidth will depend on the length of the nonlinear crystal. In the case of broadband phase matching (which happens when the wavelength dependence of phase match condition is zero in the first order approximation), it can be shown that the actual phase matched bandwidth is inversely proportional to the square root of the length of the crystal. E.g. this means that a four time's longer crystal has half the wavelength acceptance. In case of narrowband phase matching, the bandwidth is inversely proportional to the length of the nonlinear crystal.

By choosing the correct mixing laser wavelength it is thus possible to design a system with desired bandwidth acceptance parameters. By having several different poling periods, e.g. side by side within the same nonlinear crystal it is possible to tune the observed spectral wavelength [10].

4 Image enhancement

The loss of high frequency image resolution associated with imaging through a Gaussian aperture, can to some extent be corrected for. We know from the diffraction theory exactly what the optical transfer function (OTF) and point spread function (PSF) are.

The optical transfer function (OTF) and point spread function are related to each other according to Eq. 3.

$$PSF = FT\{OTF\} \tag{3}$$

FT is the Fourier transform. The PSF can be understood as the spatial distribution of upconverted photons originating from a point source. It can be shown that the OTF is the actual shape of the mixing laser (λ_2). This implies that if high spatial resolution is desired, one should have a large beam diameter inside the nonlinear crystal.

Since the OTF is Gaussian, we can correct for the loss of high frequency information. In fig. 2 we demonstrate the image enhancement possible from applying a wiener filter to deconvolve the acquired upconverted image.

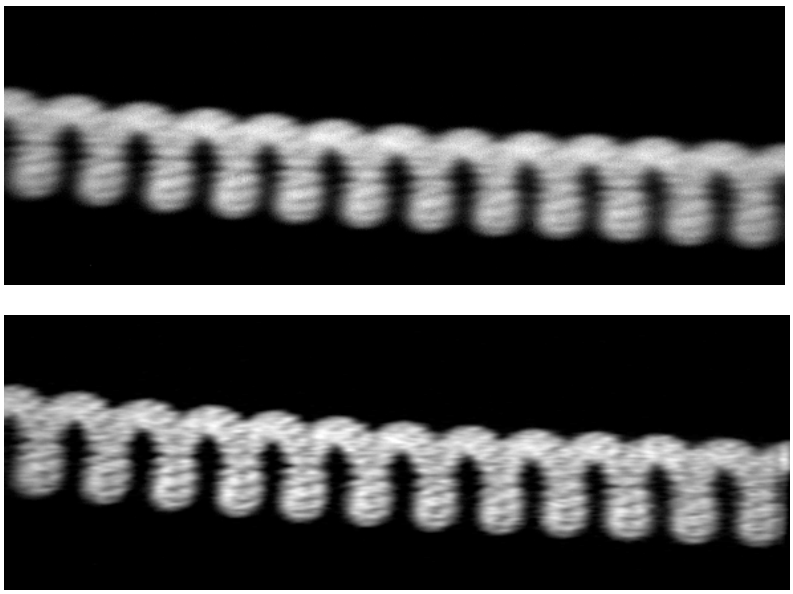

Fig. 2. Image of the filament in a light bulb. Light is upconverted from 765 nm (0.25 nm bandwidth) to 488 nm. The upper image shows the acquired image. The lower shows the same image after wiener filtering.

The ability of the wiener filter to increase the contrast and resolution is further demonstrated by applying the same filter to a resolution target as illustrated in Fig. 3.

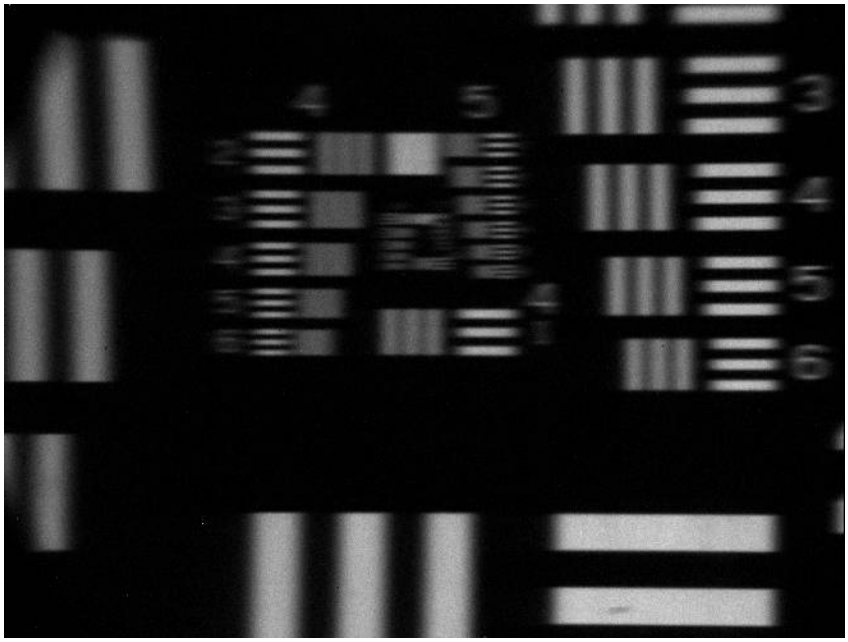
4
5
3
4
5
6

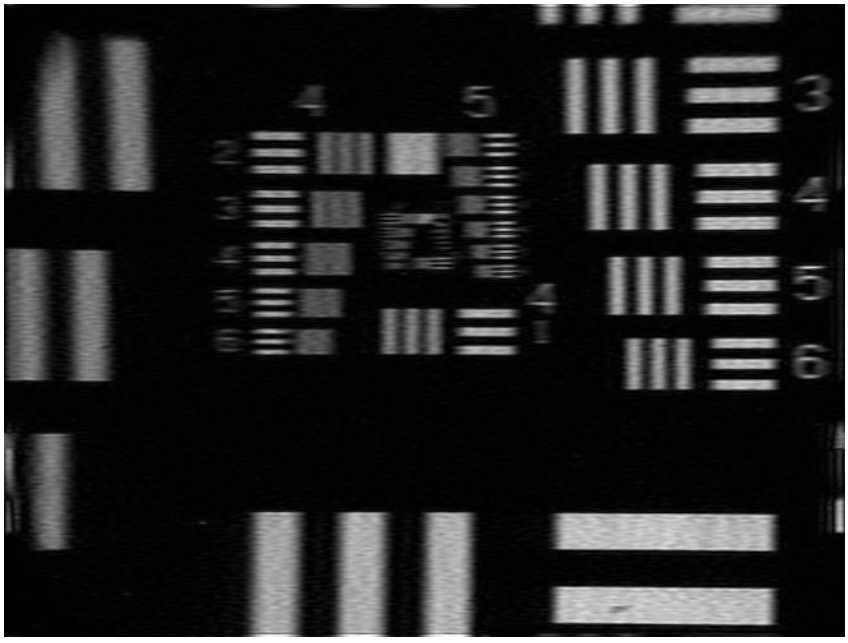
4
5
3
4
5
6

Fig. 3. Before and after image restoration. Clearly the lower image (Image restored) has better contrast and the resolution is also improved at the cost of a reduced signal to noise ratio.

As can be seen from Fig. 3 the image restoration results in higher resolution. In the original image vertical line pattern 4.2 is the smallest resolvable vertical lineset. In the image enhanced version pattern 4.3 can be resolved. This corresponds to 12 % better resolution. The contrast is also much improved.

5 Conclusion

To conclude, we have demonstrated a versatile novel method for wavelength conversion of light while preserving image information. There is a large degree of freedom in how the light is converted, as the spectral response can be designed with a quite large degree of freedom. Since the process does lead to some loss of spatial resolution, we have demonstrated how this loss can be minimized by application of image restoration techniques.

References

1. J. E. Midwinter, “Image conversion from 1.6 μ to the visible in Lithium Niobate,” Appl. Phys. Lett. 12, 68--70 (1968).
2. J. E. Midwinter, “Infrared up conversion in lithium-niobate with large bandwidth and solid acceptance angle,” Appl. Phys. Lett. 14, 29--32 (1969).
3. J. Falk and W. B. Tiffany, “Theory of parametric upconversion of thermal images,” J. Appl. Phys. 43, 3762--3769 (1972).
4. R. F. Lucy, “Infrared to Visible Parametric Upconversion,” Appl. Opt. 11, 1329--1336 (1972).
5. J. Warner, “Parametric Up-Conversion from the infra-red,” Opt. Quant Electron 3, 37--48 (1971).
6. J. Warner, “Spatial resolution measurements in up-conversion from 10.6 m to the visible,” Appl. Phys. Lett. 13, 360--362 (1968).
7. R. W. Boydand C. H. Townes, “An infrared upconverter for astronomical imaging,” Appl. Phys. Lett. 31, 440 (1977).
8. J. S. Dam, C. Pedersen, P. Tidemand-Lichtenberg, “High-resolution two-dimensional image upconversion of incoherent light”, Opt. Lett. **35**, 3796—3798 (2010).
9. S. Baldelli, “Sensing: Infrared image upconversion”, Nature Photon. **5**, 75--76 (2011).
10. J. S. Dam, C. Pedersen and P. Tidemand-Lichtenberg, "A simple model for 2D image upconversion of incoherent light", Proc. SPIE 7917, 791714 (2011).

Classification Methods for CT-Scanned Carcass Midsections

A Study of Noise Stability

Jacob Lercke Skytte[1], Anders Lindbjerg Dahl[1], Rasmus Larsen[1], Lars Bager Christensen[2], and Bjarne Kjær Ersbøll[1]

[1] DTU Informatics, Technical University of Denmark
[2] Danish Meat Research Institute, Danish Technological Institute

Abstract. Computed tomography (CT) has successfully been applied in medical environments for decades. In recent years CT has also made its entry to the industrial environments, including the slaughterhouses. In this paper we investigate classification methods for an online CT system, in order to assist in the segmentation of the outer fat layer in the midsection of CT-scanned pig carcasses. Prior information about the carcass composition can potentially be applied for a fully automated solution, in order to optimize the slaughter line. The methods comprise Markov Random Field and contextual Bayesian classification, and are adapted to use neighbourhood information in 2D and 3D. Artificial Poisson noise is added to the provided dataset to determine how well each of the methods handles noise. Good noise handling will allow lower dose scannings. The investigated methods did not perform better than the reference model in terms of classification, but the MRF segmentation showed promising results in a case with extreme simulated noise.

1 Introduction

The Danish slaughterhouses process approximately 20 million pigs every year [1]. This means that even a slight streamlining of the slaughter process might result in huge benefits. One way of streamlining the process, which has been investigated intensively in recent years, is the use of online CT-scanning [2]. Using computed tomography (CT) on a pig carcass (half a pig body), makes it possible to directly extract anatomical information, which otherwise only would be possible to obtain, after the carcass has been cut. This obviously has a huge potential in terms of optimization. There is an anatomical variation between pigs, and CT provides the possibility to determine how well a specific carcass is suited for a certain product before it is cut. Furthermore, prior information can also be used to guide the cutting process to ensure a maximum yield and minimum waste of meat. The use of CT-technology in future slaughter houses has become so well founded, that the long term goal is to scan every pig carcass online before cutting, in order to optimize, organize, and automate the entire slaughter process.

Commercial tolerances provide guidelines and quality measures for products cut from the carcass. If such tolerances can be estimated before the carcass is processed, the initial cuts could be placed optimally. Some of these commercial tolerances can be found from the outer fat layer of the carcass midsection. For the process of segmenting the outer fat layer, a natural step is to partition the voxels into a fat- and a meat class, hereby obtaining the outline of the meat, see Fig. 1.

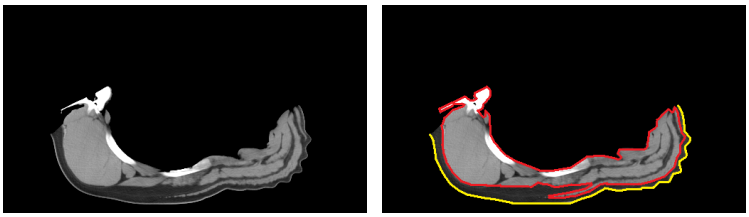

(a) (b)

Fig. 1. (a) shows a slice from the midsection of a CT-scanned carcass. **(b)** shows the same slice with a crude outlining (**red**) of the meat. The outer fat layer is located between the meat outline and the skin (**Yellow**). Note that bone is included in the outline.

We test two methods for creating a binary partition in CT-scanned carcass midsections. Each method utilizes neighbour (contextual) information in both 2D and 3D. However, the voxels of the provided CT-data are anisotropic, which complicates the step from 2D to 3D. Noise is well-known to appear in CT-scans and our motivation for taking neighbour information into consideration is that we expect an increased noise stability. If a classification to some degree can be invariant to noise, it would allow for lower dose CT-scans. In medical applications patients will be exposed less harmful radiation, and in industrial applications it is faster and more cost efficient.

2 Methods

We investigated two different methods in order to classify each voxel of a CT-scan to belong to the two classes denoted π_{fat} or π_{meat}. Both methods were applied utilizing neighbour information in both 2D and 3D.

2.1 Contextual Bayesian Classification

A 2D contextual Bayesian classification scheme has been developed by Hjort *et al.* [8], and extended to the third dimension by Larsen [4]. For these schemes, a

feature vector is created for each voxel. This feature vector contains the voxel intensity, X, of the current voxel, along with intensities for the six (for the 3D version) immediate neighbours, i.e. $\mathbf{X} = (X_{\mathrm{C}}, X_{\mathrm{N}}, X_{\mathrm{E}}, X_{\mathrm{S}}, X_{\mathrm{W}}, X_{\mathrm{T}}, X_{\mathrm{B}})^T$ where the subscripts denote current, north, east, south, west, top and bottom respectively. Based on the feature vector we want to make a classification, that is find the $v \in \{\mathrm{fat}, \mathrm{meat}\}$ that maximizes $P(C = \pi_v \mid \mathbf{X} = \mathbf{x})$. Using Bayes theorem and the law of total probability we have

$$P(C = \pi_v \mid \mathbf{X} = \mathbf{x}) = \tag{1}$$

$$\frac{p_v \sum_{a,b,c,d,e,f} P(\mathbf{X} = \mathbf{x} \mid C = (\pi_v, \pi_a, \pi_b, \pi_c, \pi_d, \pi_e, \pi_f)) g(\pi_a, \pi_b, \pi_c, \pi_d, \pi_e, \pi_f | \pi_v)}{h(\mathbf{x})},$$

where p_v is the prior probability of the classes, (a, b, c, d, e, f) is one of the possible 2^6 class configurations of the neighbours, and $h(\mathbf{x})$ is a normalization. $g(\cdot)$ introduces a prior notion of the class configurations, as it only allows the spatial patterns in Fig. 2.

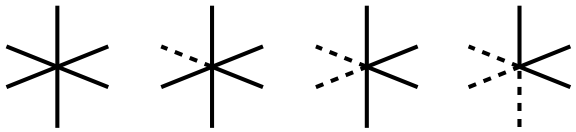

Fig. 2. Four allowed spatial patterns of the class configurations. More patterns are obtained by rotation.

2.2 Markov Random Field Segmentation

The Markov Random Field (MRF) model is well-known from medical image segmentation [3]. It can be used to model the spatial interactions between voxels, and have free parameters to control the amount of allowed interaction in the spatial directins. Following Li [7], an energy function for the MRF can be defined based on a neighbourhood system. The MRF, along with its energy function, can be translated into a flow network, and following Kolmogorov and Zabih [6], the energy can be minimized using graph cuts. This yields an optimal classification of the voxels, into π_{fat} and π_{meat}, for the defined MRF model.

3 Data

Data was provided by Danish Meat Research Institute (DMRI) and consisted of 22 CT pig carcasses scanned at a high dose (80mA), from which the midsections

were extracted. Each of the midsections consisted of approximately 70 slices (z-direction) of 512×512 pixels (xy-direction). Each voxel was anisotropic with a physical dimension size of 1×1×10mm in the xyz-directions. Furthermore, the carcasses have been preprocessed by trimming the volumes in the y-direction, in order to remove the scanner table. Fig. 3 shows an entire CT-scanned pig carcass along with the location of the midsection. Additionally, a single midsection, scanned at both high (80mA) and low dose (10mA), was also provided.

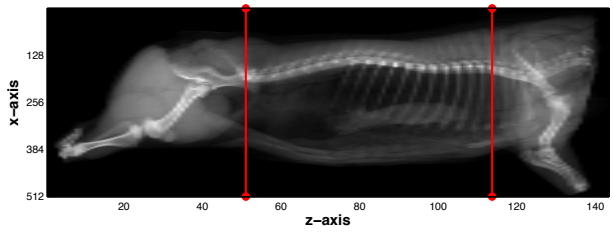

Fig. 3. A pig carcass shown in the xz-plane. The midsection is located between the red vertical lines.

4 Results

DMRI currently uses the 2D variation of the contextual Bayesian classifier along with mathematical morphology. This has shown good results regarding weight estimation of entire pig carcasses [5]. We therefore use this method as reference.

To evaluate the methods, artificial noise was added to the CT-volumes. The noise was modeled by adding Poisson noise, with parameter λ, to the data. An appropriate λ was found by comparing the amount of mis-classified voxels using the reference method on the midsection with true noise data and the same midsection with simulated noise. Additional samples, with increased noise levels, were also created. The noise simulation is illustrated in Fig. 4. More advanced CT-noise modeling was not considered.

The free parameters for the MRF segmentation were estimated for each noise level by looking at the mis-classification rates compared to the reference. It was found that the interaction in the xy-direction should be equal, but the interaction in the z-direction was insignificant.

Fig. 5 shows the amount of mis-classifications as a function of the noise level. The methods seems to have approximately equal mis-classification rates for fat

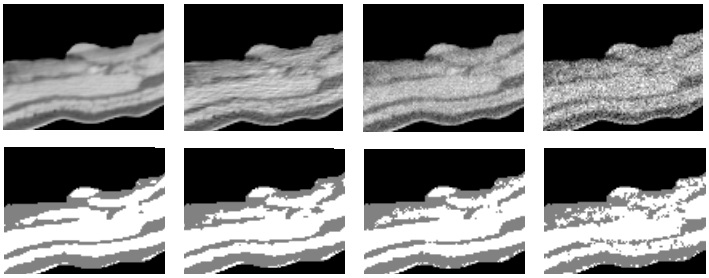

Fig. 4. The first row shows a zoomed view of a slice with, no noise, real noise, simulated noise, and increased simulated noise respectively. Notice that the real noise seems to consist of larger structures, where the simulated noise structures are small. The second row shows the corresponding classifications using the reference method.

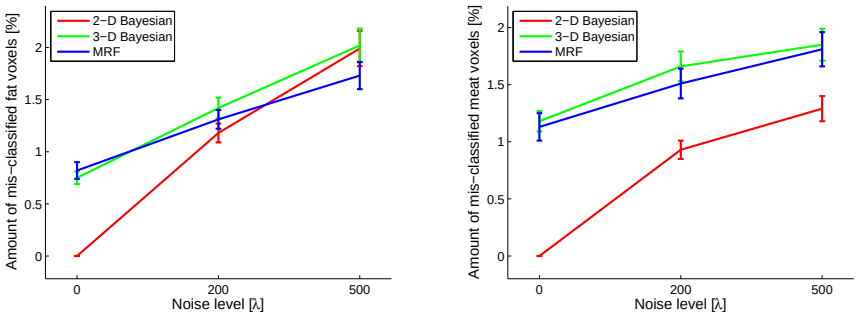

Fig. 5. The mean of mis-classification rates for fat- and meat voxels for all 22 CT-carcasses. The included interval denotes the standard deviation.

voxels, but not for the meat voxels. This was found to be due to the fat marbling, where a lot of the voxels are a mixture of fat and meat.

As fat marbling lies within larger meat structures and rapidly changing between slices, there was a tendency of overestimating the amount of meat voxels in these areas. It was found that the new methods did not introduce any significant advantages over the reference method in terms of classification.

However, for the case where we wanted to extract an outline of the meat as in Fig. 1, a small scenario with extreme noise was investigated. As seen in Fig. 6, the MRF segmentation was more successful at producing a nice and smooth outline, as the amount of smoothing can easily be controlled contrary to the contextual Bayesian classifiers. This flexibility might be really important for data with real noise, as the noise structures tend to be bigger in these cases.

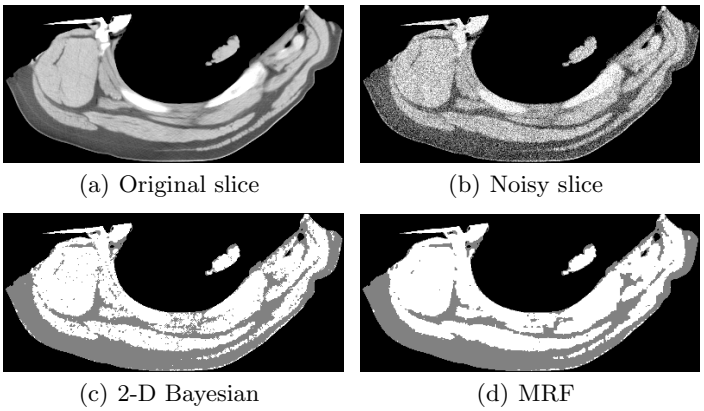

(a) Original slice (b) Noisy slice

(c) 2-D Bayesian (d) MRF

Fig. 6. Classification results for a case of extreme noise.

5 Conclusion

We have investigated the segmentation of noisy CT-data using MRF and a contextual Bayesian classifier. Extending the methods to the third dimension did not improve the results. However, in a case with extreme noise, the MRF segmentation showed promising results when extracting the outline of the meat, which was the target of the investigation.

References

1. Agriculture & Food. Statistics 2009 - Pigmeat. June 2010.
2. C. G. Jensen. CT-skanning på svineslagteriet - kun fantasien sætter grænser. *Nyhedsbrevet: Ny Viden om Slagteri og Forædling, Nr. 2, 2009.*
3. D. L. Pham, C. Xu, J. L. Prince. A Survey of Current Methods in Medical Image Segmentation. Submitted to *Annual Review of Biomedical Engineering, January 19, 1998.*
4. R. Larsen. 3-D Contextual Bayesian Classifiers In *IEEE Transactions on Image Processing, Vol. 9, No. 3, March 2000.*
5. A. Lyckegaard, R. Larsen, L. B. Christensen, M. V. Christensen, E. V. Olsen. Contextual Analysis of CT Scanned Pig Carcasses. In *52nd International Congress of Meat Science and Technology (ICoMST),* pages 207-208, 2006.
6. V. Kolmogorov, R. Zabih What Energy Functions Can Be Minimized via Graph Cuts? In *IEEE Transactions on Pattern Analysis and Machine Intelligence, Vol. 26, No. 2, February,* pages 147-159, 2004.
7. S. Z. Li. Markov Random Field Modelling in Computer Vision. Springer-Verlag Tokyo, 1995.
8. N. L. Hjort, H. V. Sæbø, K. Bråten, B. Llewellyn, E. Sohn. Contextual Classification of Remotely Sensed Data: Statistical Methods and Development of a System. In *Norwegian Computing Center, Tech. Rep. 768, 1985.*

Quantification of Microstructures in Freeze-Dried Carrots using µCT

Arno Duijster[1], Gerard van Dalen[2], John van Duynhoven[2,3], and Lucas van Vliet[1]

[1] Quantitative Imaging Group, Department of Imaging Science and Technology, Delft University of Technology, Lorentzweg 1, 2628 CJ Delft, The Netherlands.
[2] Advanced Measurement & Data Modelling, Unilever Research & Development, Olivier van Noortlaan 120, 3133 AT Vlaardingen, The Netherlands.
[3] Laboratory of Biophysics, Wageningen University, Dreijenlaan 3, 6703 HA Wageningen, The Netherlands.

Abstract. The characterization of the microstructures of freeze-dried food products determines the speed of and the properties after rehydration. The pore size distribution is an important characteristic of such textures. Spatial homogeneity and the orientation of voids and cracks inside the samples are studied.

Keywords: freeze-drying, fruit, vegetables, microtomography, granulometry, pore size

1 Introduction

Dried fruits and vegetables (F&V) are important ingredients in many convenience food products like soups, sauces and complete meals. However, the current products are a compromise between convenience and sensorial/nutritional quality. Most F&V are generally dried convectively with heated air. A disadvantage is the substantial degradation in appearance (shrunken, shrivelled, darkened), nutrients and flavour and the low rate of rehydration. Higher quality products can be obtained using freeze-drying (FD) methods. However, the very porous structure leads to a loss of texture and increase of friability. So far no systematic approach that considers the underlying microstructure during the fresh-dried-rehydrated processing chain has been applied. A major barrier to embark on such an approach has been the lack of adequate measurement technologies that enable decision making based on sound microstructural data. Hence we have deployed X-ray microtomography (µCT) [4,5] to investigate the microstructural impact of FD. 3D image analysis methods were developed to obtain quantitative information about the porous microstructure. This information will further be used to develop mathematical models for simulation of the moisture transport within the product. These models will focus on the control of ice crystal growth, microstructure and the speed of rehydration. Finally, these models will be validated using MRI. In this paper, the usability of 3D image analysis methods will be demonstrated on two individual carrot samples.

2 Material and methods

2.1 Carrots

Cylindrical samples with a diameter and length of 10 mm were cut from winter carrots. These samples include parts of the central stele and peripheral cortex, containing different types of cells having different size, shape and orientation. Samples were frozen at two different temperatures: −28 ℃and −196 ℃. Freeze drying is based on the dehydration by sublimation of a frozen product. It results in a very open structure with large cavities promoting fast rehydration. These cavities are not the plant cells but are created by the ice crystals. The size of these cavities is therefore mainly influenced by ice crystallisation behaviour or the cooling rate.

2.2 X-ray microtomography (µCT)

The internal porous structures of the samples were visualised using a SkyScan 1172 desktop X-ray micro-tomography system. A stack of approximately 2000 horizontal cross sections (4000 × 4000 pixels) was produced with a pixel size of 4.0 µm. The contrast in µCT images is based on the difference in X-ray attenuation of the constituents of the sample (e.g. solids and air), which is influenced by the density and composition of the constituents.

2.3 Image processing

The µCT images of freeze-dried carrots as shown in figure 1 clearly show differences between both drying methods. The sample on the left shows elongated voids oriented in a diagonal direction. Close inspection reveals two types of tissues, one on the bottom left and one on the top right side of the sample. The sample on the right shows more clearly distinct tissues: fine structures on the right and a very porous tissue on the left, both containing long cracks.
A characterization of these textures can be achieved in several ways. One of the quantitative methods is the computation of the distribution of the pore sizes, also called a granulometry. The minimum pore width is taken as a characteristic for the pore size. The minimum pore size can be related to the speed of the ingress of water during the rehydration.
A second quantification is based upon the homogeneity of the sample. Two types of homogeneity can be distinguished: *homogeneity in pore size*, indicated by a narrow size distribution, and *spatial homogeneity*, which means that each subset of a spatially homogeneous sample will generate 'the same' granulometry. Spatial inhomogeneity may be an indication that more than one type of tissue is present in the sample.
A third quantification is the orientation of pores, cracks and voids in a sample. As can be observed, the pores are not scattered randomly, but they are more or less parallel, due to the biological composition of the sample.

Granulometry The distribution of the sizes of the pores can be obtained using morphological sieving [1,2]. The distribution is obtained by a closing scale-space, using a sphere with increasing diameter. The spherical shape of the structuring element guarantees rotation invariance, so it is independent of the orientations of the sample and of the structures within the sample. The morphological closing is now defined as a dilation of the image with a specific structuring element, subsequently followed by an erosion with the same structuring element. As a result, all voids smaller than the size of the structuring element are filled in.

$$C(x,d) = (I(x) \oplus S(d)) \ominus S(d)\,, \tag{1}$$

where $\oplus$ and $\ominus$ denote the dilation and the erosion respectively, $I(x)$ is the image and $S(d)$ is the structuring element of diameter d. By choosing a set of increasing spherical structuring elements, a cumulative size distribution $G(d)$ can be obtained, as

$$G(d) = \frac{\int C(x,d)dx - \int C(x,0)dx}{\int C(x,\infty)dx - \int C(x,0)dx}\,, \tag{2}$$

where the closing $C(x,0)$ is equal to the original image and $C(x,\infty)$ is the closing with an infinite structuring element, which is equal to the image with all voids filled in.
Finally, we need a test to decide whether acquired granulometries differ significantly. In statistics, a Kolmogorov-Smirnov test is one of the most useful methods to compare empirical cumulative distribution functions. Suppose F_{1,N_1} and F_{2,N_2} are two cumulative distribution functions generated from respectively N_1 and N_2 independent and identically distributed observations. To test the equality of those distributions, a null hypothesis is formulated: the two distributions are equal. This hypothesis is rejected as

$$H = \sqrt{\frac{N_1 N_2}{N_1 + N_2}}\ \frac{\sup_x |F_{1,N_1}(x) - F_{2,N_2}(x)|}{K} > 1 \tag{3}$$

where $1 < K < 2$ is a critical value, depending on the significance of the test [3]. However, this test assumes that the observations are independent. The number of observations N for each granulometry is required in the test, but this cannot be the number of pixels that contribute to a particular scale. Note that each point in the curve represents an area of pixels, within the diameter of the corresponding structuring element. Here, we need a parameter which indicates the number of degrees of freedom. Since these pixels are not independent, they will not yield a reliable test. Instead of the number of pixels, the number of spheres may be a more accurate estimate for N. This value is calculated from the granulometry curve as the total area of the voids divided by the area of the characteristic diameter, i.e. the diameter where the granulometry equals one half.

Spatial homogeneity The spatial homogeneity can be defined in several ways. An obvious method is to divide the image into blocks and compute a granulometry for each block. If the sample is spatially homogeneous, these granulometries

will appear the same. Again, a Kolmogorov-Smirnov test is required in order to decide whether two granulometries from different parts of the sample are equal or not. A second method can be the analysis of the contribution from a specific closing diameter. After closing an image with a structuring element with a specific diameter, the spatial distribution of the remaining voids can be computed. This spatial distribution is an indication of spatial homogeneity.

Orientation As can be seen in the images, the voids and cracks are not oriented randomly. Most voids are elongated in the radial direction (with respect to the center of the whole carrot). Cracks appear in these samples both along and perpendicular to the radial direction.
As an approach in the determination of the main directions of the voids, one can take the projection of the sample from a specific angle. This leads to a direction dependent mass density. If the voids are aligned with the projection, the mass density shows peaks (summed cell walls) and low values (summed voids). As a result, the variance of this signal is large. If the voids are not aligned, the signal will be more homogeneous. Rotation of the sample over 180°, will lead to a direction dependendent variance.

3 Results

3.1 Granulometry

The grey-valued µCT images are thresholded in order to get a binary image. After tresholding, the images are despeckled and masked in order to define the outer edge of the carrot sample. Cracks are regarded to be part of the sample. The acquired binary three-dimensional datasets are used as an input for the computation of the pore size distribution.
Computation of the granulometry for all datasets leads to the results shown in figure 2. The curves are in good agreement with visual inspection. The $-196\,^{\circ}\mathrm{C}$-curve rises earlier than the other curve, due to the fine structures present in the right half of the sample. For larger diameters (above 60 µm), the curve flattens and finally rises to 1 at a diameter of approximately 1000 µm. This is due to the large hole in the center left part of the sample. Application of the Kolmogorov-Smirnov test leads to $H = 287$. Experimentally, it has been determined that comparable distributions lead to H-values considerably smaller than 100. As a result, the hypothesis that both distributions are equal, is clearly rejected.

3.2 Spatial homogeneity

The second image (freeze-dried at $-196\,^{\circ}\mathrm{C}$) shows two distinct tissues, one on the left side with large voids and one on the right with very fine structures. The image is now cut into four equally sized blocks ($2000 \times 2000 \times 2000$ pixels) and the granulometry is computed for each quadrant. Figure 3 shows the results. As can be seen, two types of curves can be distinguished. The curves from the right part

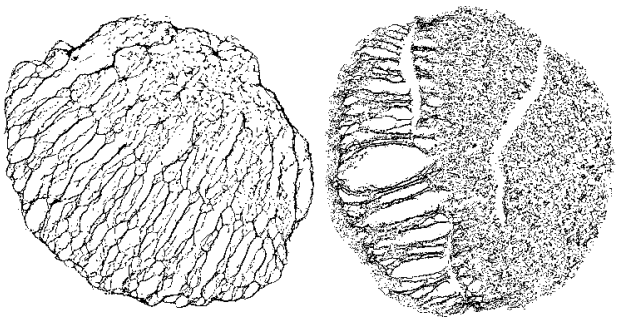

Fig. 1. Cross sections of two carrot samples, freeze dried at different temperatures. On the left at −28 ℃ and on the right at −196 ℃.

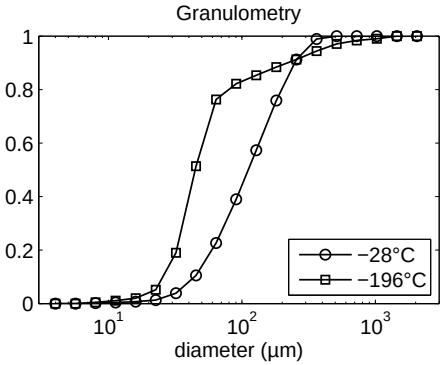

Fig. 2. Granulometries of carrot samples, freeze-dried at different temperatures.

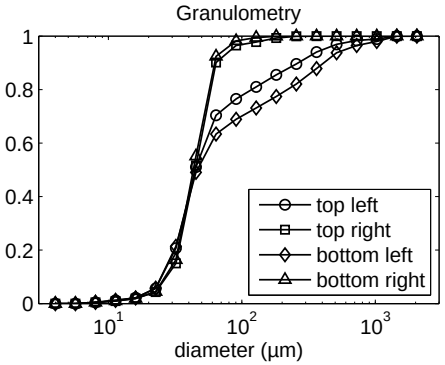

Fig. 3. Granulometry of four quadrants of the carrot sample, freeze-dried at −196 ℃.

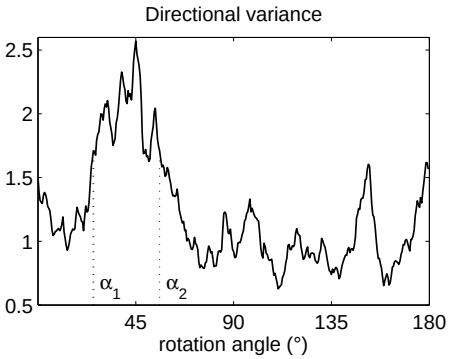

Fig. 4. The variance of the mass density as a function of the projection angle.

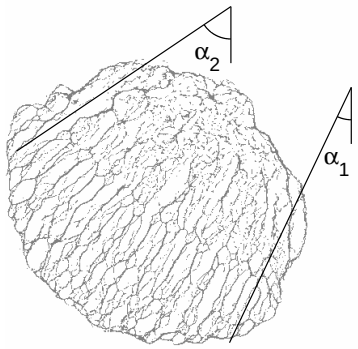

Fig. 5. Two angles from figure 4, plotted in the sample.

do not differ much from each other and show a steep rising around 50 µm, which is the characteric pore size of the fine structures. The other two curves show that a significant part of the area has a minimum pore size of $50 - 1000$ µm, which is in agreement with the expectations. The granulometry of the whole sample, as shown in figure 2, is the area-weighted mean of those four curves. Comparison of these curves leads to large values ($H > 150$) when a left quadrant is compared with a right quadrant and significantly lower values when the two left quadrants or the two right quadrants are compared ($H = 56$ and $H = 27$ respectively).

3.3 Orientation

The variance of the mass density of the first sample ($-28\,^{\circ}\mathrm{C}$) is shown in figure 4. As can be seen, between the angles α_1 and α_2, the signal is relatively large. In figure 5, these two angles have been plotted on top of the sample. The range between those two angles covers the directions of the elongated voids on the bottom left part of the sample.

4 Conclusion and further work

The granulometry is an important measure to characterize microstructures. It is also a valuable characteristic to discriminate between two or more types of tissue. Spatial homogeneity and orientation of voids and cell walls have been studied and proven to be useful.
Future work includes a more in-depth study of the orientation and shape of voids and wall thicknesses, and the correlation between granulometry and MRI measurements. For the modeling of the rehydration, the speed of water ingress has to be related to the connectivity of the voids and the tortuosity of the sample.

Acknowledgement Part of this work was supported by the Dutch Food and Nutrition Delta programme (project FND08001).

References

1. Bangham, J.A., Chardaire, P., Pye, C.J., Ling, P.D.: Multiscale Nonlinear Decomposition: The Sieve Decomposition Theorem. IEEE Trans. Pattern Anal. Mach. Intell. 18(5), 529 – 539 (1996)
2. Luengo Hendriks, C.L., Van Kempen, G.M.P., Van Vliet, L.J.: Improving the Accuracy of Isotropic Granulometries. Pattern Recogn. Lett. 28(7), 865 – 872 (2007)
3. Massey, F.J.: The Kolmogorov-Smirnov Test for Goodness of Fit. J. Amer. Statistical Assoc. 46(253), 68 – 78 (1951)
4. Mohorič, A., Vergeldt, F., Gerkema, E., Van Dalen, G., Van den Doel, L.R., Van Vliet, L.J., Van As, H., Van Duynhoven, J.: The Effect of Rice Kernel Microstructure on Cooking Behaviour: A Combined µCT and MRI Study. Food Chem. 115(4), 1491 – 1499 (2009)
5. Van Dalen, G., Nootenboom, P., Van Vliet, L.J., Voortman, L., Esveld, E.: 3D Imaging, Analysis and Modelling of Porous Cereal Products using X-Ray Microtomography. Image Anal. Stereol. 26, 169 – 177 (2007)

Barcode imaging of chocolate milk

Flemming Møller,

Danisco A/S, Physical Food Science, Edwin Rahrs Vej 38, 8220 Brabrand, Denmark

Flemming.moller@danisco.com

Abstract. Chocolate milk stability was monitored using spectral images. It is demonstrated how a time series of images can be converted into a single image, named a stability barcode. The stability barcode was generated by collapsing time series frames to pixel columns. Classical image filters were used to generate the pixel columns. Chocolate milk can show different instability types such as layers or marbling. It is demonstrated how median and standard deviation filtering can be used to detect chocolate milk layers and marbling, respectively.

Keywords: Chocolate milk, stability, creaming, sedimentation, marbling, spectral image, time series, barcode.

Chocolate milk is the most popular flavoured milk product worldwide. It is also one of the most difficult flavoured milk types to produce. Several factors have to be controlled when producing high quality chocolate milk. First, a good grade of cocoa powder should be selected with good flavour and good bacterial quality. As the cocoa particles are not soluble, the cocoa powder should be "superfine" in order to reduce tendency for the particles to settle on the bottom of the bottle. In addition, it is necessary to use stabiliser compounds to keep the cocoa in suspension. Most stabilizers used in chocolate milk form a weak gel-like structure by interaction with the milk proteins. This structure remains intact while the milk is undisturbed, suspending the cocoa particles in its network, but breaks down as soon as the milk is gently shaken or disturbed during drinking [1].

A stable chocolate milk is visually homogenous throughout the shelf life of the product. The most common types of instability seen in chocolate milk are, sedimentation, fat creaming, top whey layer or marbling. The formulation, processing and storage conditions of the chocolate milk can greatly influence the instability type and kinetics of its development [1].

The aim of this work is to develop methods to visualize the destabilization kinetics which can occur in chocolate milk: sedimentation, creaming, whey separation and marbling. In this work, marbling is considered most important since only sensory analysis has previously been able to quantify marbling.

2 Danisco A/S, Physical Food Science, Edwin Rahrs Vej 38, 8220 Brabrand, Denmark

1.1 Chocolate milk

Chocolate milks with different levels and types of stability were manufactured. Formulation and composition can be seen in **Table 1**. The processing was: add dry ingredients to 50°C milk+water, heat to 65°C and de-areate for 30 minutes, adjust pH to 6.3. Homogenize upstream at 200 bar/70°C. Heat treat at 137°C for 4 sec. Cool to 20°C and fill into sterile flasks.

An image of the six chocolate milks is shown in **Fig. 1**. Samples 1, 2, 4 and 5 looks stable, though sample 2 and 5 have some white 'clouds'. Sample 3 shows sedimentation and sample 6 marbling and creaming. In **Fig. 1** all samples show a horizontal line one third down in the product – this is thought to be a camera artifact, since this could not be seen by humans or the analytical set-up.

Table 1 Ingredients and composition of evaluated chocolate milk.

Composition	1	2	3	4	5	6
Total Fat	1.48	1.48	1.48	1.48	1.48	1.48
Total MSNF	2.56	5.48	5.99	5.48	5.48	8.01
Total Dry Matter	8.63	11.55	16.74	11.55	11.55	14.51
Total Carbohydrate	5.58	7.1	12.05	7.1	7.1	8.6
Total Protein	1.16	2.3	2.5	2.3	2.3	3.4

Fig. 1 The chocolate milks evaluated by the end of the evaluation period (3 days).

1.2 Imaging device

The stability of the chocolate milk was evaluated using a VideometerLiq instrument (Videometer A/S, Hørsholm, Denmark). The instrument is composed of a camera, light emitting diodes (LED) placed in an integrating sphere and a backlight. The equipment produces diffuse lighting which ensure homogenous and reflection-free images. The instrument acquires multi-spectral images by strobing the 10 diffuse LEDs and backlight one at the time, see **Table 2** for wavelength information. The resulting multispectral image is 460 * 1450 pixels which correspond to 19*60 mm.

Disposable sterile flasks with chocolate milk are placed in the VideometerLiq instrument. An auto sampler that can hold 6 samples makes it possible to generate time series of images. The time series of images is necessary for visualization and quantification of any instability.

Table 2 VideometerLiq wavelengths and lighting types.

Wavelength (nm)	Colour	Lighting type
405	UV	Diffuse
450	Blue	Diffuse
470	Blue	Diffuse
505	Blue-Green	Diffuse
525	Green	Diffuse
570	Green	Diffuse
630	Red	Diffuse
660	Red	Diffuse
700	Red	Diffuse
850	NIR	Diffuse
850	NIR	Backlight

1.3 Spectral images

Creaming and marbling was seen in the UV and visual image bands, preferably the low wavelengths. Surprisingly was creaming not seen clearly in the NIR images. An alternative technique for measuring chocolate milk stability uses a 850 nm laser and proton multiplier for measuring stability of food products (Instrument: Turbiscan produced by Formulaction AS, France) [1, 2]. The Turbiscan instrument is not able to detect marbling.

The penetration depth of light is wavelength dependent, i.e. long wavelengths penetrate further than short wavelengths. For this reason short wavelengths are best for imaging fine surface structures.

1.4 Stability evaluation

Chocolate milks can show instability as a function of storage time, conditions and composition. The most common instability types are:

- Layers
    - Sedimentation
    - Creaming
    - Whey separation
- Bulk changes
    - Marbling
    - Colour change

Quantification of layers is done by measuring the thickness as a function of time. The bulk changes are measured in the middle part of the product in between any layers. Destabilization kinetics should be measured relatively to the freshly produced product; hereby influence due to formulation and processing is reduced.

All chocolate milks were evaluated for 3 days and a total of 132 spectral images per sample were recorded. **Fig. 2** shows selected images from the stability evaluation of sample 6, only images at 505 nm are shown[1]. The first image from the time series (leftmost image) shows a stable chocolate milk with some air bubbles at the top. A bright top layer is forming soon after production and increases in thickness as a function of time. Marbling is seen as an inhomogeneous structure which forms soon after production.

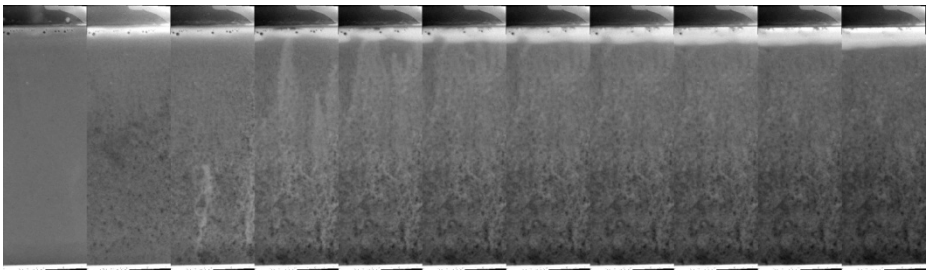

Fig. 2 Selected images at 505 nm of sample 6. The images are taken throughout the evaluation period.

Stability barcodes

A way of converting a time series of images into one image is by converting each frame to a pixel column and let the width represent the time – all pixel columns are then stacked to one 2D image. Conversion of movie frames to a 2D image is known as movie barcodes [4, 5]. The conversion from a 2D image into a 1D column can be done by calculating the mean pixel value in each 2D image row (from 2D to 1D). The width of the 1D columns is scaled to reflect the period between two frames. All the scaled 1D columns are placed according to their order and together generate the stability barcode, see Figure 3.

Median barcodes can be used for detection of layers and colour changes, see **Fig.** . Layers are seen as horizontal zones which increase in intensity as a function of time, for example samples 2 and 5 show sedimentation and sample 6 creaming (seen as red in the mean barcodes). A chocolate milk can be stable, but still show colour change, this is seen in samples 4 and 5 that become darker as a function of time.

[1] 505 nm had a high signal to noise and was used for all work in this paper.

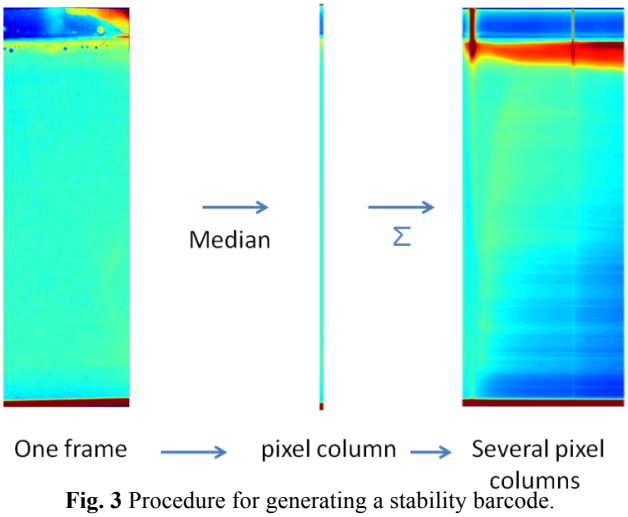

Fig. 3 Procedure for generating a stability barcode.

In figure 3 the median barcode for the six evaluated chocolate milks is presented. The first measurement (first pixel column) is subtracted from each barcode, thereby any intensity differences due to formulation and processing are removed.

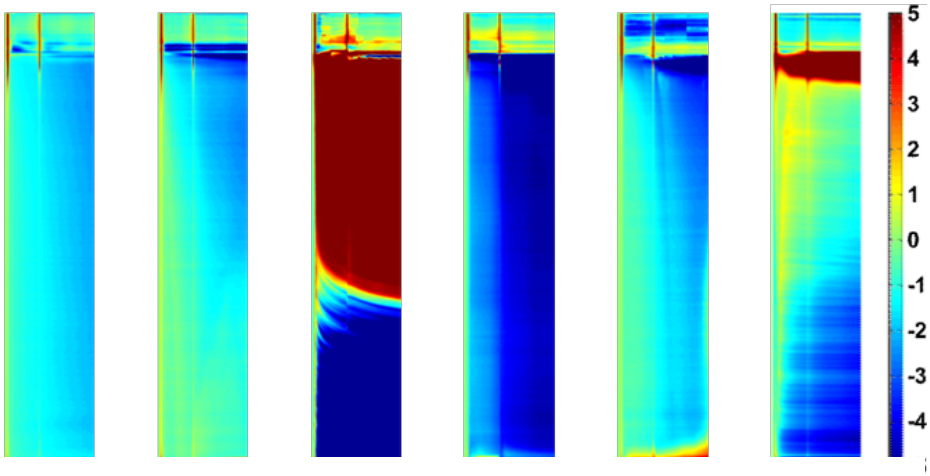

Fig. 4 Median barcodes for the 6 chocolate milks. Each barcode represents 3 days of analysis at 505 nm. The x-axis represents time. Column points are calculated by a 1D median filter of the original image rows.

Structure development in the chocolate milk (marbling) can be visualized by calculating the standard deviation or using classical image filters to generate the barcode, see Fig. 5. Marbling in samples 3 and 6 is seen as high standard deviations in the middle/lower part of the chocolate milk. A white haze in samples 2 and 5 is also seen as an increase in the standard deviation barcode after some storage time.

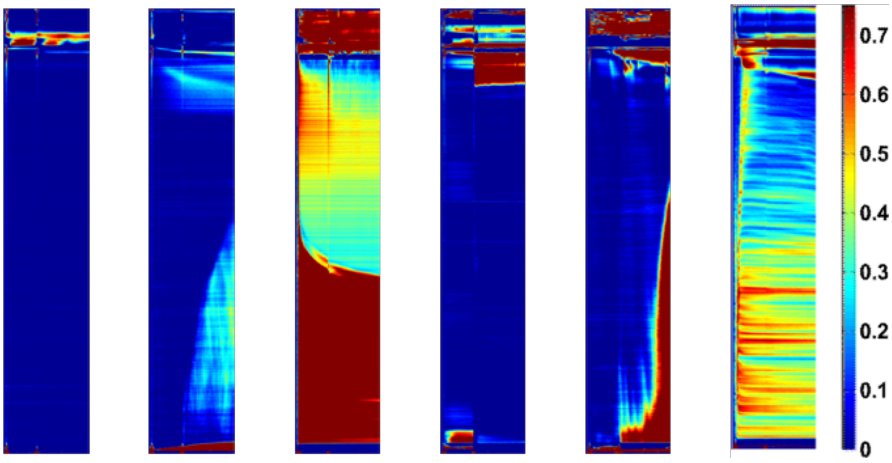

Fig. 5 Standard deviation barcodes for the 6 chocolate milks. Each barcode represents 3 days of analysis at 505 nm. The x-axis represents time.

Future work should demonstrate how data from the barcodes can be used to statistically compare the different chocolate milk formulations. It should also be investigated if orthogonal transformations, such as PCA, MAF and MNF can be used as a pre-treatment step.

1.5 Conclusion

It was demonstrated how destabilization of chocolate milk could be visualized by converting a time series of images into a single image, a stability barcode. Median and standard deviation filters were used to calculate the stability barcodes. The median filter was able to detect colour and layer changes the standard deviation filter could detect marbling and haze in the chocolate milk.

1. Boomgaard, T. van den; Vliet, T. van; Hooydonk, A. C. M. van. Physical stability of chocolate milk. Int J of Food Sci & Tech. **22**,3 pp 279-291 (1987)
2. Mengual O, Meunier G, Cayre I, Puech K, Snabre P. Characterisation of instability of concentrated dispersions by a new optical analyser: the TURBISCAN MA 1000. Colloids and Surfaces A: Physicochemical and Engineering Aspects. Vol. 152, Issue. 1-2, pp. 111 -123 (1999)
3. Grotenhuis TE, Tuinier R, de Kruif CG. Phase stability of concentrated dairy products. Jour. Of dai. Sci. Vol. 86, Issue: 3, pp. 764-769 (2003)
4. White, Michelle. "Jason Salavon: Emblem," Artlies, Issue 47, 2005.
5. Flowing data, Movie barcodes, http://flowingdata.com/2011/03/07/entire-movies-compressed-into-single-barcodes/

Multispectral imaging of wok fried vegetables

Hanne Løje[1], Bjørn S. Dissing[2], Line H. Clemmesen[2], Bjarne K. Ersbøll[2] and Jens Adler-Nissen[1]

[1]National Food Institute, Division of Industriel Food Research,
Technical University of Denmark, DK-2800 Lyngby, Denmark
{halo,jadn}@food.dtu.dk

[2]Department of Informatics and Mathematical Modelling
Technical University of Denmark, DK-2800 Lyngby, Denmark {bdi,lhc}@imm.dtu.dk

Abstract. This paper shows how multispectral images can be used to assess color change over time in wok fried vegetables. We present results where feature selection was performed with sparse methods from the multispectral images to detect the color changes of wok fried carrots and celeriac stored at +5°C over 14 days. A pairwise t-test was used to detect if the differences over days were significant. For both the original as well as a follow experiment significant differences were seen in particular for celeriac, but also to some extend for carrots.

Keywords: multispectral images, color change, celeriac, carrots, wok fried vegetables.

1. Introduction

Quality control in the food industry is an important issue and it is mainly conducted by measuring various chemical components in the food. In this study, we propose the use of multispectral imaging to evaluate colour changes of meal elements for professionally prepared meals with regards to change in surface colour after freeze-chilling and thawing at +5°C over a period of 14 days.

Meal elements are robust semi-prepared convenience components based typically on meat, fish or vegetables and meant for professional use. Earlier studies have shown that stir-fried vegetable meal elements have promising properties with respect to high culinary quality and robustness towards freezing and thawing, thereby potentially solving a major hindrance for the use of heat-treated vegetables as meal elements (Adler-Nissen, 2007). Freeze-chilling involves a complete freezing of the products followed by storage at freezing temperature after which the products will be thawed at refrigeration temperatures (O'Leary et al., 2000). Freeze-chiling allows the manufacturer flexibility in manufacturing and distribution. The pre-fried vegetables are produced by a new process for continuous stir-frying in industrial scale, which has been introduced for producing convenience high-quality vegetables (Adler-Nissen,

2002). The pre-fried vegetables produced according to the process are generally prepared from the raw. They have a low fat content (typically 1%–2% of the product weight), a texture and flavour similar to what can be achieved in the kitchen, and vitamins are preserved almost 100% (Burgaard et al., 2004).

Celeriac and carrots were the subjects of this study, and the colour changes were measured by a multispectral imaging device called VideometerLab (http://www.videometer.com). The VideometerLab acquires multi-spectral images of up to 20 different wavelengths ranging from 430 to 970 nm.The camera system uses a diffuse sphere to achieve a uniform and reproducible illumination, which enables the creation of detailed surface chemistry maps with a good combination of spectral and spatial resolutions plus reproducibility over time (Gomez et al., 2007).

2. Materials and methods

Celeriac and carrots (shaped as cubes of size approximately 0.5 cm3) were fried in a continously wok (Adler-Nissen, 2002). Afterwards the products were packed in plastic bags and frozen at – 30°C. After 4 months of freezing (experiment 1) and 1½ months of freezing (experiment 2) the bags with the pre-fried vegetables were removed from the freezer and thawed up to 14 days at +5° in a refrigeration. One each day of analysis (day 2, 4, 8, 10, 12 and 14) one plastic bag was taken out from the refrigeration, the vegetables were placed in petri dishes, and the multispectral images were recorded by the VideometerLab.

Six images were recorded over 14 days for two different data set. Both experiments were conducted under the same cirumstances and the dataanalysis were performed equally for the two sets.

During the 14 days of image recording, the surface changes and thereby reflectance properties were very subtle. Therefore advanced statistical techniques were applied to to search a large featurespace of variables extracted from the chemistry maps. The features extracted were purely reflectance properties found by calculating pairwise interactions between bands within the region of interest. These interactions were then each converted to a set of percentiles which were used as features. With 20 spectral bands this amounts to a substantial amount of features. An elastic net regression was performed to extract the features of relevance and obtain good generalization (Zou & Hastie, 2005). The elastic net method uses an ordinary least squares regression with L_1- and L_2-norm penalization of the parameter estimates. The regularizations give spartisty and shrinkage to the parameters which preciously has proved to give good predicitons in high-dimensional data with correlations amongst the covariates (Clemmensen et al., 2010). The number of days was used as response variable for the predictions.

3. Results

The results showed that the celeriac predictions were somewhat better than the carrots, although a trend was seen in both. The statistical tests for experiment 1 showed that for carrots a significant change in the mean from day 2 to day 4 was seen. After day 4, it was not possible to verify a significant change in mean for carrots anymore, which could indicate a steady state has been reached. For the celeriac the change in mean continued until day 12 with the exception of day 8 where some uncertainty appears (Dissing et al., 2009).

Pairwise two sided t-tests showed exactly that these changes were statistically significant at a 5% level of significance.

In the present study the wok fried vegetables were packed in plastic bags prior to freezing and storage. Plastic bags are not tight against oxygen molecules, thus we believe that the observed changes in the spectra is caused by oxidation of the plant pigments in the vegetables. An oxidation causes browning/graying of the celeriac and carrots to become more pale. An increasing brown/gray colour is changes in a wide range of the spectrum and thereby a change of brightness. For celeriac the most significant components consisted of wavelengths from the entire visible spectrum, which match a general shift in brightness. For carrots the components seem to have a tendency to lie in the red/NIR area, which also match with a general more pale appearance, or removal of redness/orangeness components due to oxidation of the beta-carotene.

A follow up experiment was performed to verify the robustness of the model. For comparison the model parameters estimated for the first experiment were used to predict the storage time for the second experiment. The output of the predictions shows very similar results to those from experiment 1, being significant changes for celeriac and less significant results for the carrots

For the first experiment, the corresponding sensory tests showed no difference over the 14 days, which makes it more important that we were able to detect minor changes under using multispectral imaging, while the detection limit for sensory changes (using a trained panel) was 14 days. These results show the strengths of multispectral imaging.

4. Conclusion

Multispectral image analysis was used as an objective measurement of surface changes in wok fried carrots and celeriac. During 14 days, images were recorded for wok fried carrot and celeriac. The results show a large change from day 2 to day 4 in the reflectance spectrum for both carrots and celeriac and this change continued until day 12 for celeriac samples. A follow up experiment show very similar results which verify the robustness of the model.

References

Adler-Nissen, J. The continuous wok – a new unit operation in industrial food processes. *J. Food Process Engin.,* **25**: 435-453, 2002

Adler-Nissen, J. (2007). Continuous wok-frying of vegetables: Process parameters influencing scale up and product quality. *Journal of Food EngitHE INneering* **83**: 54-60.

Burgaard, M., Matzen, A., Adler-Nissen, J., (2004), Kontinuerlig wok til industriel brug. *Plus Proces* no. **6**: 24-26.

Clemmensen, L. H., Hansen, M. E., and Ersbøll, B. K. (2010), A comparison of dimension reduction methods with applications to multi-spectral images of sand used in concrete, Machine Vision and Applications, **21**(6): 959-968.

Dissing, B. S., Clemmensen, L. H., Løje, H., Ersbøll, B. E., and Adler-Nissen, J. (2009), Temporal reflectance changes in vegetables, *In proceedings: CRICV, Kyoto, Japan*.

O'Leary, E., Gormley, T. R., Butler, F., and Shilton, N. (2000), The effect of freeze-chilling on the quality of ready-meal components, Lebensm.,-Wiss. U. Technol., **33: 217-224**

Gomez, D. D., Clemmensen, L. H., Ersbøll, B. K., and Carstensen, J. M. (2007), Precise acquisition and unsupervised segmentation of multi-spectral images, *Computer Vision and Image Understanding*, **106**(2-3): 183-193.

Zou, H., Hastie, T., (2005). Regularization and variable selection via the elastic net. *Journal of Royal Statistical Society - Series B **67*** (Part 2), 301–320.

Multi-spectral Image Analysis for Astaxanthin Coating Classification

Martin Georg Ljungqvist[1,2] * Bjarne Kjær Ersbøll[1], Michael Engelbrecht Nielsen[2], Stina Frosch[2]

1. Technical University of Denmark (DTU),
Department of Informatics and Mathematical Modelling
2. Technical University of Denmark (DTU),
National Food Institute, Division of Industrial Food Technology

Abstract. Industrial quality inspection using image analysis on astaxanthin coating in aquaculture feed pellets is of great importance for automatic production control. In this study multi-spectral image analysis of pellets was performed using LDA, QDA, SNV and PCA on pixel level and mean value of pixels for each pellet. Classification using LDA or QDA on pellet mean or median values showed better results than using the pixel values or PCA.

Keywords: astaxanthin, multi-spectral, image analysis

1 Introduction

Industrial quality inspection using image analysis is an area of extensive development. Pigment inclusion in aquaculture feed pellets is of great interest for automatic visual analysis for statistical production control and optimisation.

Astaxanthin is a naturally occurring carotenoide with a high antioxidant activity essential for reproduction, growth and survival, and important for the development of colour in salmonide fishes [1]. The primary use of astaxanthin within aquaculture is as a feed additive to ensure that farmed salmon and trout have similar appearance as their wild counterparts [2]; it is the pigment that makes salmonide fishes red. The colour appearance of fish products is important for the customers. Astaxanthin is highly expensive [3] and therefore optimisation of its use in fish feed production is of importance.

An automatic vision system for on-line quality control of pigment inclusion will be of great benefit to the industry both in relation to process control and process optimisation.

This paper is based in part on an earlier study by Ljungqvist et al. (2010) [4]. Besides this no further work has to the authors' knowledge previously been done on analysing the coating of fish feed using image analysis. Multi-spectral image analysis has shown good results in previous biological applications [5, 6, 7, 8] where it is of interest to detect subtle differences in colour and surface chemistry.

* malj@imm.dtu.dk

The aim of this project is to investigate the possibility of distinguishing between feed pellets coated with fish oil with and without added astaxanthin using multi-spectral image analysis and in this way investigate what spectral features are of interest for further analysis of astaxanthin coating.

2 Material and Methods

2.1 Material

The feed type used is EcoLife20 and AquaLife R90, both with the radius of 4.5 mm. The fish feed pellets are divided into two groups. One class constitutes pellets coated with fish oil with 50 ppm added of a synthetic version of astaxanthin; class A (astaxanthin). The other class is the same pellet types with fish oil coated without additional astaxanthin included; class B (base). (The fish oil typically contains a small amount of natural astaxanthin, but this is assumed to be less than 1 ppm and should therefore not affect the results.) The distribution of the surface coating is unknown and some amount of variation is likely to occur.

A total of 2223 EcoLife20 pellets were used, and a total of 2158 AquaLife R90 pellets were used, see Table 1.

2.2 Imaging Equipment

The equipment used was a camera and lighting system called VideometerLab which supports a multi-spectral resolution of up to 20 wavelengths. These are distributed over the ultra-violet A (UVA), visible (VIS) and first near infrared (NIR) region. The range is from 385 to 1050 nm.

This system uses a Point Grey Scorpion SCOR-20SOM grey-scale camera and the objects of interest are placed inside an integrating sphere (Ulbricht sphere) with uniform diffuse lighting from light emitting diodes (LED) placed around the rim of the sphere. The curvature of the sphere and its white matte coating ensures a uniform diffuse light so that specular effects are avoided and likewise minimising the amount of shadows. The device is calibrated radiometrically with a following light and exposure calibration. The system is geometrically calibrated to ensure pixel correspondence for all spectral bands [9].

The image resolution is 1280 × 960 pixels. Each file contains 20 images, one for each spectral band. This results in a multi-spectral image cube with dimensions of 1280 × 960 × 20.

Table 1. Number of analysed pellets in each group.

	Size (mm)	Class A samples	Class B samples	Total samples
EcoLife	4.5	1165	1058	2223
R90	4.5	1207	951	2158

2.3 Spectral Equipment

In order to further explore the spectral properties of astaxanthin a spectrometer was used. Absorption spectra of synthetic astaxanthin in a solution of fish oil along with plain fish oil were recorded in the VIS and NIR range using a NIRSystems 6500 absorption spectrometer. The absorption spectra was transformed to reflection values using the standard relation $A = -log(R)$, where A is absorption values and R is the reflection values.

2.4 Image Analysis

The pellets were segmented from the background using a grey-scale threshold.

The basic pellet compound gives a spectral response which will be present in both class A and B. Each pixel is thus a combination of the reflectance of a set of constituents. This mix is assumed to be of equal amount for each pellet type except for the difference of the astaxanthin coating that we want to isolate in our classification.

The ground truth is that we know that certain pellets are coated with synthetic astaxanthin, but since the surface distribution is unknown it is unclear how much synthetic astaxanthin each of those pixels contains. This gives us an uncertain one-to-many relationship situation.

A way to solve this uncertainty is to represent each pellet using the mean or median of all pixels in a pellet as sample values. In this manner we even out the variance of all pixels in a pellet and each pellet becomes a distinct observation.

In addition to the pellet pixel mean and median values further summary statistics features to describe the coating distribution were extracted based on pellet pixel values: Skewness, kurtosis, variance and maximum value.

PCA Our multivariate data from the images was analysed using principal component analysis (PCA) for exploratory purpose. PCA is the most optimal method with respect to maximising the variance [10] and has been commonly used for dimension reduction for dealing with ill-posed problems. If the relation of interest contains large variation then PCA is a good method for analysing the data.

The pre-processing method standard normal variate (SNV) [11] was used to reduce any variation in concentration level of the overall coating concentration between pellets.

Discriminant Analysis To discriminate between the two classes we want the within group deviation to be small compared to that between groups. Wilk's Λ consists in principle of the ratio of the within group variation ($\mathbf{W}$) and the total variation ($\mathbf{T}$), i.e. the within group plus the between group variation. $\Lambda = \frac{\det(\mathbf{W})}{\det(\mathbf{T})}$. A value of Wilk's Λ which is close to zero indicates that the two groups are well separated.

For statistical discriminant analysis methods we use linear discriminant analysis (LDA) and quadratic discriminant analysis (QDA) [10]. They are both based

on the Mahalanobis distance, and assumes that the variables in each class are normally distributed. LDA and QDA are based on a distance to the class mean weighted by the variance. A training set of 70% of the samples were used here, along with a test set of 30% of the samples.

3 Results and Discussion

It turned out that spectral band number 20 showed some artefacts for about half of the EcoLife20 class A due to temperature variations so therefore statistical tests were also performed without this band. Results show that this problem did not affect the classification in a negative manner (results not shown).

Comparing the SNV-normalised mean spectra of the two classes of EcoLife20 elucidates the largest difference being at 970, 950 and 565 nm (in order of magnitude). Both 970 and 950 nm are in the NIR range, while 565 nm represents the green colour which is next to yellow. For AquaLife R90 the largest difference between the class spectra are in the visual range around 400 nm and also slightly above 600 nm.

The spectrometer results show a large deviation between synthetic astaxanthin in fish oil and plain fish oil to be in the range of 500 – 600 nm, see Figure 1. This corresponds well with the results from the VideometerLab images and partly corresponds with previous studies of astaxanthin [12, 13].

The mean spectra of the two groups of both EcoLife20 and AquaLife R90 are significantly different at a 0.1% level. This is promising for classification between the two coating groups. On the other hand, Wilk's lambda of the class means of EcoLife20 pellet mean values equals 0.987, and for AquaLife R90 it is 0.826. The high values here are reflecting the situation of high variation within the groups and a low variation between the groups. So even though the class means are well separated, there is a vast overlap of the two groups.

Classification tests of EcoLife20 show that LDA on the pellet means or pellet medians gave the best result with a classification correctness of about 93%. See Table 2 for test results.

Classification tests of AquaLife R90 show that QDA on the pellet medians gave the best result with a classification correctness of 100%.

Using LDA and QDA on the other summary statistics features (skewness, kurtosis, variance and maximum value) gave results of lower correctness for both pellet types (results not shown).

Using PCA before doing LDA or QDA on the pellet mean values did not improve the results, see Table 2. This may be an indication that maximising the variance is not a well-suited method for this particular problem, which also was indicated by the high variation within groups in comparison to the variation between groups. PC2 shows the largest difference between the two classes, see Figure 2. The first five principal components explain 98% of the total variance of the pellet mean values, and still the result of the discriminant analysis on these five components rendered worse classification in comparison to using the plain data itself.

Table 2. The misclassification of pellet coating type for different kinds of features. Displayed values are total test error for classification of the two groups A (astaxanthin) and B (base).

EcoLife20	LDA	QDA
Mean	0.0646	0.0901
Median	0.0736	0.0931
Mean, SNV, PC1-5	0,1396	0,2162
AquaLife R90		
Mean	0.0046	0.0031
Median	0.0015	0.0000
Mean, SNV, PC1-5	0.0185	0.0201

To sum up, the results show that it is possible to distinguish between feed pellets with and without inclusion of synthetic astaxanthin in the coating using multi-spectral image analysis. However, more work is needed in order to make the method robust for various pellet types and also for various amount of astaxanthin. Since astaxanthin is expensive it is desired to have a good accuracy in the method. This will further on be of importance for developing on-line quality food and feed products with optimal use of pigment and minimum amount of waste.

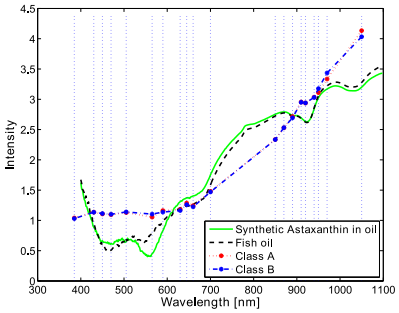

Fig. 1. Spectrometer reflectance of synthetic astaxanthin in oil (*green*) and plain fish oil (*black*). Multi-spectral images (reflectance) mean of class A (synthetic astaxanthin in fish oil) (*red*) and class B (fish oil) (*blue*) of the EcoLife20 type.

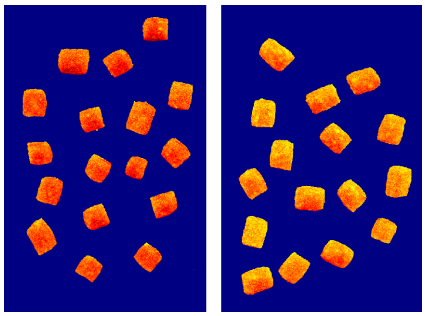

Fig. 2. The 2nd principal component of the multi-spectral image (reflectance) of EcoLife20 pellet pixels. Pellets coated with synthetic astaxanthin in fish oil, class A (*left*). Pellets coated with fish oil, class B (*right*). Red colour indicates high values.

Acknowledgments

The work presented has received funding from BioMar A/S and the EU under the Seventh Framework Programme FP7/2007-2013 under grant agreement number 214505.10.

References

[1] J.B. Owen. Genetic variation and nutrition - edited by a. p. simopoulus and b. childs. *Clinical Nutrition*, 10(1):61–62, 1991.

[2] O.J. Torrisen, R.W. Hardy, and K.D. Shearer. Pigmentation of salmonids - carotenoid deposition and metabolism. *Reviews in Aquatic Sciences*, 1(2):209–225, 1989.

[3] R.T.M. Baker, A.-M. Pfeiffer, F.-J. Schöner, and L. Smith-Lemmon. Pigmenting efficacy of astaxanthin and canthaxanthin in fresh-water reared atlantic salmon, salmo salar. *Animal Feed Science and Technology*, 99(1-4):97–106, 2002.

[4] Martin Georg Ljungqvist, Stina Frosch, Michael Engelbrecht Nielsen, and Bjarne K. Ersbøll. Analysis of astaxanthin in fish feed pellets. *Proc. West European Fish Technologists Association*, 40:59–60, Oct 2010.

[5] David Delgado Gomez, Line Harder Clemmensen, Bjarne K. Ersbøll, and Jens Michael Carstensen. Precise acquisition and unsupervised segmentation of multi-spectral images. *Computer Vision and Image Understanding*, 106(2-3):183–193, 2007.

[6] Line Katrine Harder Clemmensen and Bjarne Kjær Ersbøll. Multispectral recordings and analysis of psoriasis lesions. *MICCAI 06 - Workshop on Biophotonics Imaging for Diagnostics and Treatment, October 6, 2006 proceedings, 9th MICCAI Conference*, 2006.

[7] Line H. Clemmensen, Michael E. Hansen, Jens C. Frisvad, and Bjarne K. Ersbøll. A method for comparison of growth media in objective identification of penicillium based on multi-spectral imaging. *Journal of Microbiological Methods*, 69(2):249–255, 2007.

[8] Bjørn Skovlund Dissing, Line Katrine Harder Clemmensen, Bjarne Kjær Ersbøll, Hanne Løje, and Jens Adler-Nissen. Temporal reflectance changes in vegetables. *2009 IEEE 12th International Conference on Computer Vision Workshops (ICCV Workshops)*, pages 1917–1922, 2009.

[9] Jørgen Folm-Hansen. *On chromatic and geometrical calibration.* PhD thesis, Technical University of Denmark, 1999.

[10] Trevor Hastie, Robert Tibshirani, and Jerome Friedman. *The Elements of Statistical Learning: Data Mining, Inference, and Prediction.* Springer, 2nd edition, February 2009.

[11] Asmund Rinnan, Frans van den Berg, and Søren Balling Engelsen. Review of the most common pre-processing techniques for near-infrared spectra. *TrAC Trends in Analytical Chemistry*, 28(10):1201–1222, 2009.

[12] Manuel. Buchwald and William P. Jencks. Optical properties of astaxanthin solutions and aggregates. *Biochemistry*, 7(2):834–843, 1968.

[13] Jian-Ping Yuan and Feng Chen. Identification of astaxanthin isomers in haematococcus lacustris by hplc-photodiode array detection. *Biotechnology Techniques*, 11(7):455–459, 1997.

Visual effects of β-glucans on wound healing in fish

Jacob G. Schmidt[1], Martin G. Ljungqvist[2], Bjarne K. Ersbøll[2], Michael E. Nielsen[1].*

1. Technical University of Denmark, National Food Institute, Biological Quality Group, DK-2800 Kgs. Lyngby, Denmark.
2. Technical University of Denmark, Department of Informatics and Mathematical Modelling, Section of Data Analysis, DK-2800 Kgs. Lyngby, Denmark.

*e-mail: jacsc@food.dtu.dk

Introduction

β-glucans are diverse polysaccharides that occur naturally in plants, fungi and bacteria. β-glucans have been shown to have an immunostimulatory effect[1]. In addition, β-glucans have been found to increase wound tensile strength and collagen synthesis[2]. This is likely to affect the filet quality[3]. With multispectral imaging we investigate the effect of adding β-glucans to the water during healing of open wounds in fish. Multispectral imaging is used in human diagnostic medicine for evaluating fx proriasis and chronic diabetic wounds, but has not yet been applied to wounds in fish.

Experimental set-up.

The fish (common carp, *Cyprinus carpio* and rainbow trout, *Oncorhynchus mykiss*) were wounded with a biopsy punch (Miltex, York, USA), thus removing a cylinder of tissue. The resulting wound exposed the muscle. Fish were then kept for 14 days in either pure tap water or tap water supplemented with β-glucans (to a final concentration of 0.1mg/L). The experiment was then either terminated or continued with normal tap water. Multispectral images were acquired several times during the experiment using a VideometerLab (Videometer A/S, Horsholm, Denmark).

Results and discussion

Experiments are still underway, but some results are expected to be ready for the workshop.

All procedures were conducted in accordance with the regulation set forward by the Danish Ministry of Justice and animal protection committees by Danish Animal Experiments Inspectorate permit 2007/561-1302 and in compliance with European Community Directive 86/609.

Acknowledgements: BIOP Graduate School, DTU FOOD PhD School and Danish Ministry of Food, Agriculture and Fisheries 304-FVFP-08-K-08-01 have all supported this work.

[1] Soltanian et al. 2009. Beta-glucans as immunostimulant in vertebrates and invertebrates. Critical Reviews in Microbiology, 35(2): 109–138
[2] Portera et al. 1997. Effect of macrophage stimulation on collagen biosynthesis in the healing wound. American Journal of Surgery, 63(2): 125-31.
[3] Ingerslev et al, in prep.

3D Measurement Analysis Method Development for Classification of Chewing Gums

Sara Kiani, Mahan Ahmadi, and Anders Heyden

Centre for Mathematical Sciences, Lund University, Sweden
heyden@maths.lth.se

Abstract. The purpose of this paper is to develop an automated 3D measuring analysis method for chewing gums produced by a pharmaceutical company. It is an important phase in a project that aims to reduce production losses that occur during the manufacturing process. The main reason is believed to be the lack of convexity in the shape of the gums. We will present a method for measuring the convexity of gums with the help of a 3D measurement equipment. An algorithm is developed that fits the data obtained from measurements of gums to the suitable mathematical model of an ellipsoid. The volume of the approximated ellipsoid that each gum is represented by determines the convexity of the gum. The volume is smaller for gums with a more convex shape. This is thereby the quality measure used to classify the gums. The measurement method is validated statistically in order to determine its statistical properties.

Keywords: 3D data analysis, fitting, image analysis, mathematical modeling, quality control

1 Introduction

In the manufacturing process of chewing gums, it is believed that reoccurring production losses are caused by planar surfaces or not sufficiently convex surfaces on the chewing gums. These imperfections might influence the coating process such that the chewing gums glue together, forming so called doublets or even triplets, and has to be discarded.

The purpose of this paper is to develop a fast and user-friendly method to measure the shape of gums and determine the level of convexity of each gum by analyzing the measurement data. By measuring a number of gums with the help of a non-contact optical measuring device, we use the data to implement an algorithm that analyzes gums according to a consistent classification system. This will hopefully help identifying the factors in the production that might cause problems in the manufacturing process.

2 Methodology

Gums of different qualities are produced during the manufacturing process, which are classified into five different convexity categories. The original clas-

sification system, prior to this project, is visual and based on the gum's level of convexity seen from different angles. An overall assessment based on the convexity determines which of the previously mentioned five categories the gum belongs to, see Fig. 1

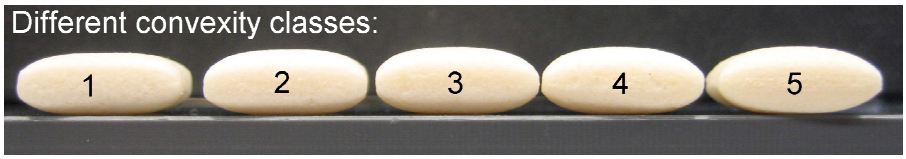

Fig. 1. Convexity classes.

The disadvantage of this classification system is occasional inconsistency due to the human factor, which a computerized measuring method would avoid. A highly advanced and accurate measuring device is used to measure the surface of the gums. An algorithm, developed in MATLAB, uses the data from the measurements to estimate the convexity of the gum and determines to which category the gum belongs.

3 Equipment

The measuring equipment used is a 3D topography measurement system for optical acquisition of the structure of rough and reflective surfaces. It consists of a desktop PC, a monitor and the interferometer TMS-100 Polytec [1], see Fig. 2. A measurement of a gum produces about 121000 data points (x-, y- and z-coordinates). The interferometer measures from the top of the gum along the z-axis going down to the edges. By brushing some talcum powder on the gum, the reflections from the surface become consistent. In turn, this helps creating more data points. In order to standardize the measuring method for the user, the optimal placement of the gum (in terms of distance from the detector of the interferometer) had to be determined. Also, a generally suitable starting and ending point in z-direction (with respect to the thickness of the gum) for the measurement had to be determined, since the device measures along the z-axis. A fixture was constructed, with the purpose of keeping the gum stabile at the optimal placement. It should help in producing consistent results and also be easy for the user to handle, i.e. by simply placing the gum on the fixture, see Fig. 2.

4 Mathematical Modeling

When a model is considered, one can fit a set of data points to the chosen model by forming a system of equations with the help of the data and then finding

[1] Manufacturer and developer of the measurement equipment.

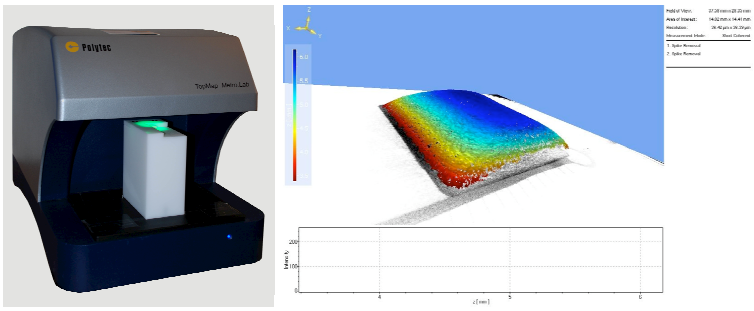

Fig. 2. The measuring device and a measurement result.

its least squares solution. Due to the large amount of data an overdetermined homogenous system of linear equations is generated. The matrix A is the size of $m \times n$, where $m > n$, and the array $\bar{x}$ is a vector of n unknown variables;

$$A\bar{x} = 0 \ . \tag{1}$$

The least squares solution to this system is obviously the trivial solution. A way to avoid this is to constrain the vector $\bar{x}$ to a fixed length by imposing $\|x\| = 1$, see [1].

A way to solve the equations numerically is by performing singular value decomposition (SVD), [2] on the matrix A, which factorizes the matrix into the unitary matrices U and V, and the diagonal matrix S which contains the singular values according to

$$A = USV^H \ . \tag{2}$$

When performing an ordered SVD on A, the diagonal elements of S are in descending order. Since the system of equations is overdetermined, there is no exact solution. The least squares solution to the system is given by the last column of V, which corresponds to the smallest singular value of the matrix S. The sum of squared errors is then at minimum, [2].

The ellipsoid model The model came from the idea that the perfect shape of the top of a chewing gum is spherical. The smaller the sphere (shorter radius), the more the surface element (the gum) is convex. The idea of a sphere evolved into an ellipsoid, which has the equation

$$k_3(z - z_0)^2 + k_2(y - y_0)^2 + k_1(x - x_0)^2 = R^2 \ . \tag{3}$$

A homogenous system of equations is formed from the measurements, giving

$$A\bar{x} = 0 \ , \tag{4}$$

with

$$A = \begin{bmatrix} z^2 & -2z & 1 & y^2 & -2y & 1 & x^2 & -2x & 1 & -1 \end{bmatrix}$$

and

$$\bar{x} = \begin{bmatrix} k_3 & k_3 z_0 & k_3 z_0^2 & k_2 & k_2 y_0 & k_2 y_0^2 & k_1 & k_1 x_0 & k_1 x_0^2 & R^2 \end{bmatrix}^T \quad .$$

The constants R^2/k_1, R^2/k_2 and R^2/k_3 are the ellipsoid's three radii squared.

Let the origin be a point placed under the centre of the gum on the surface that the gum lies on. Let x_0, y_0 and z_0 describe the distance from the origin to the centre of the fitted ellipsoid. Due to the complexity of the combination of unknown variables, the system cannot be solved linearly.

The number of unknown variables needs to be reduced. x_0 and y_0 can be eliminated by shifting the x and y data points in the x- and y-direction so that the centre of the sphere is placed below the centre of the gum with the distance of z_0 between the centre of the sphere and the origin. The new system, with a total of five unknown variables, can still not be solved linearly with SVD because of its non-linearities.

In order to make further reductions of the number of un-known parameters, one could estimate z_0 beforehand. Suppose that there is circle that follows the shape of the gum. One can then estimate z_0, which denotes the distance from the origin to the centre of the circle, by subtracting the largest value of the measured z-points from the estimated radius of the circle.

The number of unknowns was reduced even further by considering k_1 and k_3 identical. The values of k_1 and k_1 are in fact very close, which was discovered empirically while studying the values of the constants from a model where z_0 was assumed to be a known variable. Making this assumption that $k_1 = k_3$ enable us to solve the system of equations by linear methods.

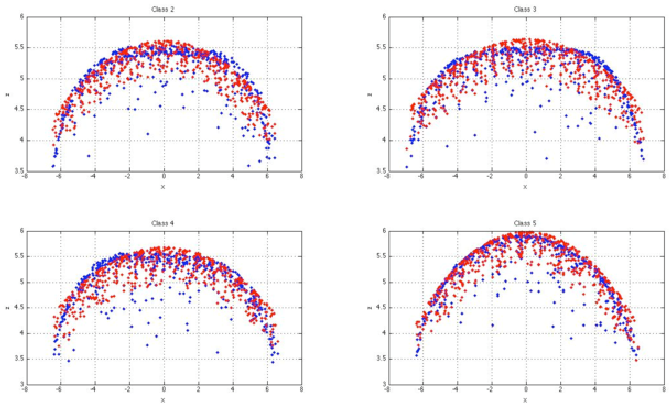

Fig. 3. Fittings of the measurement data from four gums, one (the flattest) of each convexity class, using the new spherical model with z0 unknown. Measured points: blue, fitted points: red.

5 Model Optimization and Quality Measure

By combining two models, solutions for the five unknown variables (k_1, k_2, k_3, z_0 and R) can be obtained. First, a system of equations is formed according to

$$k_1(z - z_0)^2 + k_2y^2 + k_1x^2 - R^2 = 0 \ . \tag{5}$$

After solving this system, the value of the unknown variable z_0 is stored. Then, a new system of equations is formed according to

$$k_3(z - z_0)^2 + k_2y^2 + k_1x^2 - R^2 = 0 \ , \tag{6}$$

using the stored value of z_0 . After solving the second set of equations, solutions for k_1, k_2 and k_3 are found and unique values for the original five unknown variables are obtained, see Fig. 3.

By adding terms that describe slight deformations that gums possibly might have in the x-z plane, y-z plane and x-y plane, the fitting becomes even better. A proposed model for this is

$$k_3(z - z_0)^2 + k_2y^2 + k_1x^2 + k_4xz + k_5yz + k_6xy - R^2 = 0 \ . \tag{7}$$

See Fig. 4 for an example.

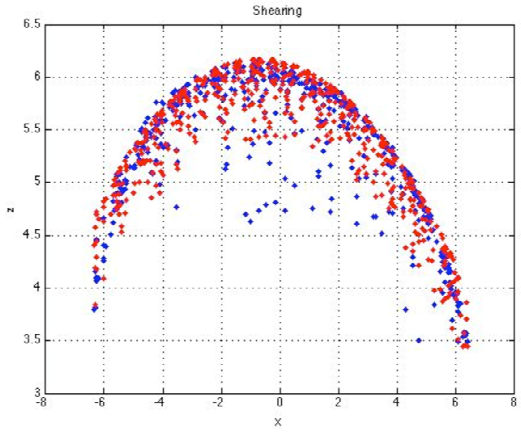

Fig. 4. Plot in 2D of measured and fitted z points, from data belonging to the thickest gum in class 5, which is slightly deformed. Data fitting according to the ellipsoid model with deformation terms. Comparison of fitting error indicates improvment when adding deformation terms to the model.

A quality measure that takes the three radii; a, b and c, into account is the volume of the ellipsoid, which is used in the algorithm. Gums with a flatter

surface are represented by bigger ellipsoids and smaller ellipsoids with smaller volumes represent gums with convex surfaces.

6 Results

The algorithm was applied to measurement data from the thirty previously mentioned gums. After computing fitted data points and finding the ellipsoid that each gum represents, the volume for each ellipsoid is calculated. The automated classification system is consequently dependant of, and will be based on these values.

6.1 Classification

The volumes of the chosen thirty gums which represent the variation in each class are computed with the final algorithm and can be seen in Fig. 5. There is a certain overlap within the different classes. It can be relatively difficult to distinguish gums of class 4 from gums of class 5, and the same goes for the rest of the classes. It is however obvious that the volume decreases, the higher the class.

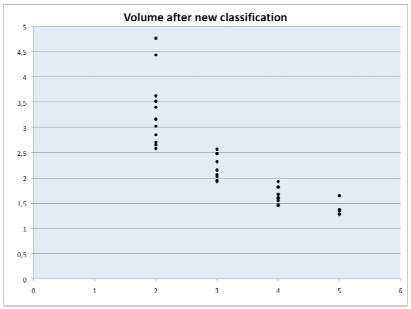

Fig. 5. Volumes ($10^4 mm^3$) of all gums from different convexity classes.

6.2 Validation

A measurement system consists of everything that has to do with the measurement, such as the measurement equipments, the measurement samples and the operators performances. These are factors of uncertainty that affect the result and its dispersion, which is actually the repeatability and reproducibility of the measurement system. That is, how well repeated measurements produce the same result. The lack of repeatability denotes the variation obtained when one operator with one measurement equipment performing multiple measurements on one sample. The lack of reproducibility denotes the variation obtained

when different operators with one and the same measurement equipment measure one and the same sample or one operator measures one sample with different measurement equipment. Reproducibility is in this case the variation between operators, [1].

These studies help determining whether the measurement system is good enough to provide an accurate method for classification of gums, by analyzing the variance, i.e. variations in the measuring system which occur when different operators perform measurements. Consistent result regardless of who performs the measurements and how many times the measurements are made, should be produced.

Two operators (A and B) measured five new, randomly selected, gums from each class, twice. The results were analyzed and the total variance became 23.49%. The measurement system is acceptable if the total variance is below 30% and considered very reliable if it is below 10%. An analysis of the measurements performed by operator A only results in a total variance of 10.85%.

7 Discussion

The method developed was based on the manual classification method, in which a general assessment of the convexity was done visually. The automated method uses a mathematical approach that provides a quality measure in terms of the volume of an ellipsoid.

7.1 Results

One can state that the new classification algorithm is an improvement of the old manual method, since these differences become much more obvious and the quality measure is thereby more precise. In spite of the simplification the developed method has contributed with, it is still essential to have some knowledge about which side of the gum is the most convex, since that is the side to be measured. It is also important to apply the appropriate amount of talcum on the gum and placing it correctly on the fixture, which also depends on how much experience the operator has.

The validation result supports these theories. Operator A had acquired much more experience in measuring, which is believed to explain the total variation when looking at the results for operator A only. The value of the total variation is near 10%, under which corresponds to a very good measurement system.

The difficult part for the inexperienced Operator B was to identify the convex side of the gum. Mistakes caused larger variation in terms of repeatability and reproducibility. Some gums of lower classes are equally flat on both sides, which makes it difficult to distinguish the convex side from the flat side. By excluding the class 2 results from the study of Operator A only, the total variation became about 5%.

The validation of the measurement method resulted in fairly good results, showing that it has a potential. However, it is essential that the person that performs the measurement has adequate experience in measuring.

7.2 Limitations of the Method

Despite the potential of the method, there are a number of issues that limits its usage. The algorithm has only been tested on "normal" gums. Gums with pressure damages might generate data that, when applied to the algorithm, yields a deceptive fit resulting in a misleading classification. In addition, if the operator is not able to reliably identify the convex side of the gum, it could be necessary to measure both sides. The side that corresponds to the smallest volume must then be the convex side.

7.3 Improvements and Further Development

This work opened up quite a few doors and there are many possibilities for further development, which include

- Non-linear Method
  The deviation of the fitting could have been less if the algorithm could handle equation systems with complex combinations of unknown variables. Possibly a custom-made non-linear method might be able to solve the system.

- Further Automatization The goal was to automatize as much as possible in order to simplify the measuring process for the operator. It is possible to integrate MATLAB code into a C# project and implement macros that can automate basically every step of the measurement.

References

1. Forsyth, D., Ponce, J.: Computer Vision: A Modern Approach. Prentice Halle (2003)
2. Süli, E., Mayers, D.: An Introduction to Numerical Analysis. Cambridge University Press (2003)

Characterization of a Commercial Danish Apple Cultivar Using Novel Optical Sensing Techniques

Mabel Martinez Vega, Torben Bo Toldam-Andersen & Dvoralai Wulfsohn

Department of Agriculture and Ecology, Faculty of Life Sciences, University of Copenhagen, Hoejbakkegaard Allé 13, DK-2630 Taastrup, Denmark.
mmar@life.ku.dk, tbta@life.ku.dk, dvor.wulfsohn@gmail.com

Abstract. Denmark has about 300 local apple cultivars; many of them are still unknown. Most of these have been previously described on a database that compiles phenological and quality features, known as 'The Pometum apple key' [2]. However, specific quality parameters that might explain their potential for commercial use are still under research. Fruit skin color is one of the quality parameters that might explain the maturity stage of apples [1]. At harvest level, skin color coverage and intensity is important when selecting the fruits that are ready to be collected. Typically well exposed fruits obtain the desired color and maturity faster and to a higher degree than those located in the inner part of the tree. We characterize the skin color of the cultivar Ingrid Marie from images taken of both exposed and non-exposed sides of samples collected systematically from the top and bottom of the tree. The data was collected in a photographic lab using a multispectral camera (DuncanTech MS3100-CIR, Auburn CA). The G, R and IR bands are centered at 550, 660 and 800nm with a bandwidth of 200nm respectively. Color variation and homogeneity of the samples were studied using ImageJ Software. The histograms showed well distributed pixel values. The blue channel histogram showed low pixel values (mean 75) whereas the red channel had high pixel values (mean 190). As for the green channel, significant differences on the histogram peaks and positive skeweness were observed.

Key words. Apple, multispectral, Ingrid Marie, Image analysis

References

1. Jongen, W.: Fruit and Vegetable Processing. Woodhead Publishing Limited, Cambridge, England (2002)
2. The Pometum Apple Key, http://www.nordgen.org/nak/?chglang=ENG

Improving texture optimization with application to visualizing meat products

Line Clemmensen & Lasse Farnung Laursen
Department of Informatics and Mathematical Modelling
Technical University of Denmark
{lhc, lfla}@imm.dtu.dk

May 17, 2011

Abstract

When inspecting food quality, CT Scanning is among the primary tools used to gain insight. It provides valuable volumetric data using a process, which leaves the product unspoiled and untouched. However, volumetric data is merely a measure of density and therefore contains no appearance information (such as color, translucency, reflective properties). One way of reintroducing this lost information back to the volume data is to synthesize an appropriate texture and apply this to the volume data.

A recent method within the field of texture synthesis is called Texture Optimization presented by Kopf et al. in 2007. This method accepts a number of 2D input exemplars, from which it generates a solid texture volume. The volume is iteratively improved via an expectation maximization algorithm. The bottleneck of Texture Optimization occurs during a nearest neighbor search, between texture patches from the 2D input exemplars and the generated texture volume. We examine the current procedures for minimizing the bottleneck and present a novel approach which increases the speed of the synthesis algorithm while minimizing loss of quality.

The nearest neighbor search is performed in a high dimensional space. Applying a principal component analysis on the texture patches originating from the synthesized solid accelerates the process. These patches are then reduced in dimensionality until "only" 95% of their original variance remains. This usually results in a dimension reduction from 192 to about 60-80. The reduction in dimensionality speeds up the convergence of the Texture Optimization method considerably.

We examine the impacts of reducing the dimensionality further by tweaking the parameters as well as introducing an alternative method to reducing the dimensionality. Additionally, we study the possibility of selecting only a subsample of the neighborhoods available from the input exemplar without significantly impacting the overall synthesis quality.

Keywords

Volumetric Rendering, Texture Synthesis, Dimension Reduction, Princible Component Analysis, Non-Negative Matrix Factorization, Subset Selection

1 Introduction

Adding appearance information to volumetric data is commonplace. In most cases this is achieved via transfer functions [HKRs+06], but a viable alternative is to use solid textures [LEB11]. Solid textures and volume data are almost a perfect match, since they occupy the same dimensions, making the application straightforward. One drawback of solid textures is that they are not easily acquired. Therefore, there exists a large body of research concerned with synthesizing solid textures from existing 2D textures, also called input exemplars. A recent method is called Texture Optimization[KFCO+07]. In brief terms, this method starts with synthesizing a solid volume based on random samples from the input exemplars. The volume is then iteratively improved on a rough scale using an Expectation Maximization method. Once it has converged, the solid texture is scaled up and iteratively improved until convergence is once again reached. Eventually the synthesis process is complete at the highest resolution of 128x128x128 voxels. Higher resolution synthesis is not performed due to the computational complexity involved.

Local correlation between the synthesized solid and the input exemplars is achieved by comparing small 8 by 8 texture patches, from here on also referred to as neighborhoods. These neighborhoods are essentially vectors in a 192 dimensional space, due to the three-color channels. For each neighborhood in the synthesized solid, the best match is found among the neighborhoods from input exemplars. Figure 1 shows how a number of neighborhoods from the synthesized solid are matched to neighborhoods originating from the input exemplar. This is basically a nearest neighbor search in a high dimensional space. This search is the bottleneck for the entire Texture Optimization method. To lessen the impact of this expensive search, a principle component analysis is performed on the input exemplars. The neighborhoods are then projected into a space where 95% of the variance is retained. This usually results in a dimension reduction from 192 to around 60-80 dimensions.

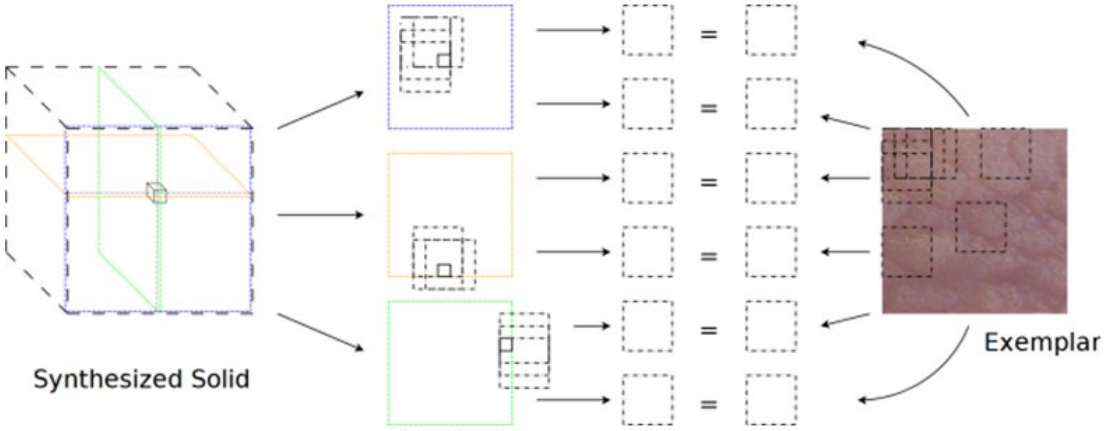

Figure 1: Neighborhoods on axis-aligned planes related to a single voxel are found. These neighborhoods are then compared to all existing neighborhoods in an input exemplar. For each, the optimal match is found.

We intend to show how optimizing the process in two different ways can further reduce this bottleneck. First, we examine whether we can further reduce the dimensionality by applying an alternative dimension reduction method as well as using fewer dimensions in the PCA. Second, we attempt to reduce the number of contributing neighborhoods based on a similarity measure. Eliminating similar neighborhoods from the pool provided by the input exemplar should speed up the synthesis algorithm while only slightly diminishing the texture quality.

2 Preliminary results

Our preliminary research has been performed on the input exemplars shown in figure 2, which originate from pig muscle.

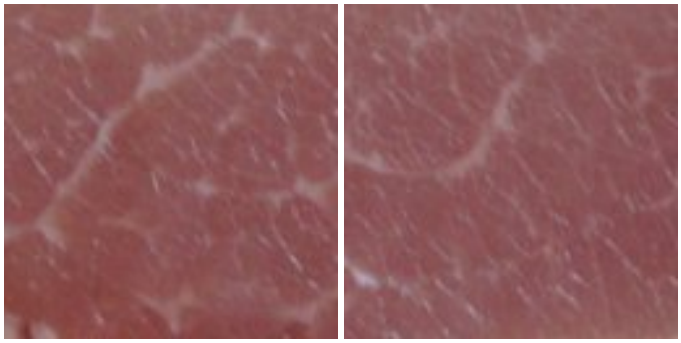

Figure 2: Input Exemplars used to obtain preliminary results.

Figure 3 shows results from the original texture synthesis algorithm, which uses a PCA reducing the number of dimensions to 80 while 95% of the variance is retained.

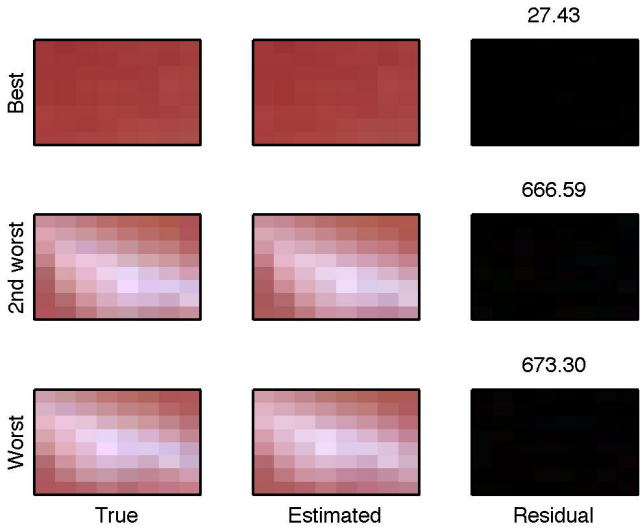

Figure 3: The true and estimated patches using a PCA dimension reduction of size 80. The last column shows the residual between the true and estimated patch and the associated number gives the SSE of the reconstruction. The rows, from top to bottom, represent the best, the 2nd worst and the worst reconstructions.

We apply Non-Negative Matrix Factorization (NMF), which is an alternative decomposition method [LS99]. NMF is known by learning by parts and instead of finding components, which describe maximal variance in data like PCA; it finds components, which describes localized features in data. Figure 4 shows the results from applying the NMF to our input exemplars.

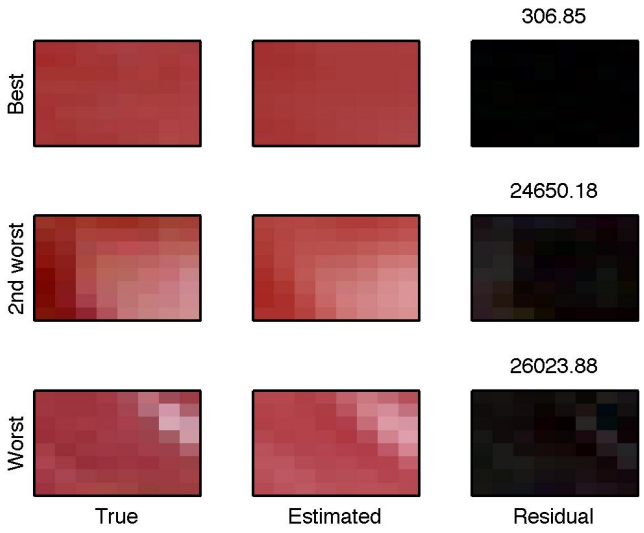

Figure 4: The true and estimated patches using NMF decompostion with a dimensionality of 15. The last column shows the residual between the true and estimated patch and the associated number gives the SSE of the reconstruction. The rows, from top to bottom, represent the best, the 2nd worst and the worst reconstructions.

The NMF reduces the dimensionality to 15, while still retaining similarity, even among the worst estimated neighborhoods.

Figure 5 shows the results of reducing the dimensionality to 15 via PCA, which contains 83% of the variance. Although the sum squared error is better when compared to NMF, the visual result is not noticeably improved. It is difficult at this point to ascertain the global impact of these changes to the final result of the texture synthesis process. The lack of perceptible difference warrants further study.

Figure 6 shows a comparison of a subset of neighborhoods extracted from the input exemplar, after a PCA dimension reduction to 80 dimensions. We measure Euclidian distance between the neighborhoods. At a Euclidian distance of 100, shown in the bottom right of figure 6, the difference between two random patches is visible, yet small. Neighborhoods with an even shorter distance will look increasingly similar. This supports our hypothesis that a number of neighborhoods are redundant and can be discarded with minimal impact to the final synthesized result.

3 Future work

Achieving the optimal balance between speed and quality will require further study. We have briefly covered the main areas within which we believe we can improve the Texture Optimization algorithm. By comparing original results from the method with results produced by our own modified methods, we should be able to achieve considerable increases in speed with hopefully minimal impact to the image quality.

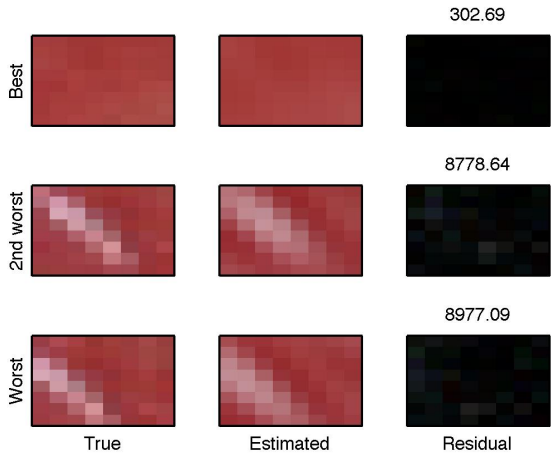

Figure 5: The true and estimated patches using PCA decompostion with a dimensionality of 15. The last column shows the residual between the true and estimated patch and the associated number gives the SSE of the reconstruction. The rows, from top to bottom, represent the best, the 2nd worst and the worst reconstructions.

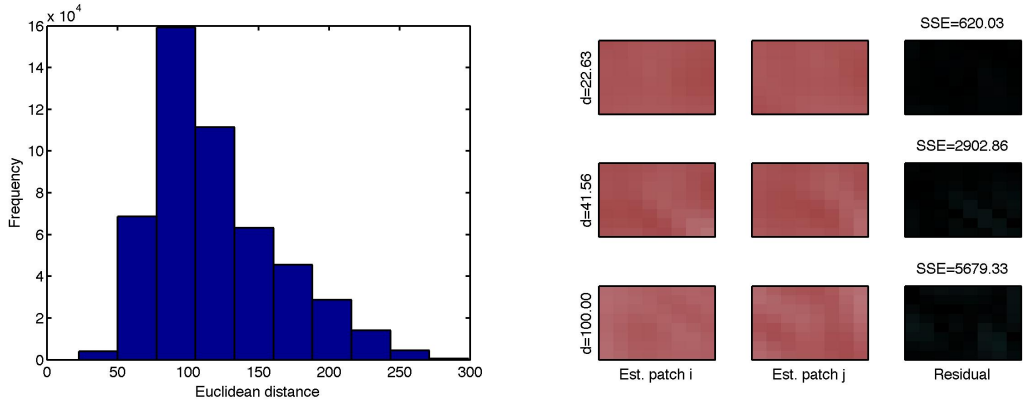

Figure 6: Left: Histogram of the Euclidian distances between the dimension reduced patches using a PCA reduction of 80 dimension. Only a subset of the patches were included in this analysis. Right: Examples of Euclidian distances (d), and an illustration of the corresponding two estimated patches, plus the residual between the two estimated patches and the SSE between the two estimated patches.

Acknowledgements

This research was supported in part by the Danish Meat Research Institute. The input exemplars were acquired with the help of the Danish Meat Research Institute.

References

[HKRs+06] Markus Hadwiger, Joe M. Kniss, Christof Rezk-salama, Daniel Weiskopf, and Klaus Engel, *Real-time volume graphics*, pp. 81–102, A. K. Peters, Ltd., Natick, MA, USA, 2006.

[KFCO+07] Johannes Kopf, Chi-Wing Fu, Daniel Cohen-Or, Oliver Deussen, Dani Lischinski, and Tien-Tsin Wong, *Solid texture synthesis from 2d exemplars*, ACM Transactions on Graphics (Proceedings of SIGGRAPH 2007) **26** (2007), no. 3, 2:1–2:9.

[LEB11] Lasse Farnung Laursen, Bjarne Kjær Ersbøll, and Jakob Andreas Bærentzen, *Anisotropic 3d texture synthesis with application to volume rendering*, 2011.

[LS99] Daniel D. Lee and H. Sebastian Seung, *Learning the parts of objects by non-negative matrix factorization*, Nature **401** (1999), 788–791.

Spectral color reconstruction and target visualization of live tissue

Md. Abul Hasnat[1], Jussi Parkkinen[1], Markku Hauta-Kasari[1], Jukka Antikainen[1], Joni Orava[1], Mikael von und zu Fraunberg[2], Juha E Jääskeläinen[2]

1 University of Eastern Finland, P.O.Box 111, FI-80101 Joensuu, Finland,
2 Kuopio University Hospital, P.O.Box 1777, FI-70211 Kuopio, Finland
mhasnat@gmail.com, {jussi.parkkinen, markku.hauta-kasari, jukka.antikainen, joni.orava}@uef.fi, {Juha.E.Jaaskelainen, Mikael.Fraunberg}@kuh.fi

Abstract. Significant amount of research has been conducted to explore the possibility of using spectral imaging in biomedical applications. However, existing solutions are not sufficient enough to handle the tradeoff between spectral resolution, spatial resolution, portability and speed of acquisition. This research propose a framework to generate neurosurgery spectral video from RGB video. A spectral estimation model is applied on each RGB video frames. A database of neurosurgery spectral images is used for both training and testing. Five different spectrum estimation techniques were experimented to determine the best model. A prototype spectral video generation system is developed according to the preference of neurosurgeons. Although this framework is established for neurosurgery spectral video generation, however, the methodology would also be just as applicable to other similar research.

Keywords: Spectral imaging, spectral estimation.

1 Introduction

The objective of spectral imaging is to represent object color most accurately through acquiring spectral information. Furthermore, this information allows reproduction of color image under various illuminations, study images in individual spectral band for better discriminating objects of interest, segmentation, recognition and classification of objects, and study computational color vision. Usage of spectral imaging technology in various fields are evidence of significant interest in this area.

An important drawback of the available spectral imaging devices is the speed of image acquisition. Despite the invent of many faster spectral imaging devices, a near real time spectral image capturing device with reasonable spatial resolution is yet to become available. In order to overcome this limitation, several alternative approaches have been proposed [1-4]. Beside these techniques, there are several computational approaches to obtain spectral reflectance with the use of conventional 3 band camera through spectrum estimation [5-10]. These approaches estimate spectral reflectance using various mathematical modeling with the aid of prior knowledge. The aim of

these estimation approaches is to reduce the cost and complexity of the image acquisition system while preserving its colorimetric and spectral accuracy.

Spectral imaging has received immense interest in the field of medical imaging modalities [11], and [12]. Spectral imaging has proven its capability to produce reliable data for the surgeons with sufficient sensitivity for discriminating different types of tissues. Now a day, surgeons are interested to see spectral image information continuously during surgery and monitor important information such as temporal changes in the organs and tissues. Therefore, a spectral video system is necessary to use during surgery. However, currently no such spectral video capturing device exists with sufficient spatial resolution which covers a wide range of spectrum. A possible solution is that, rather than using spectral video system, a RGB video camera in cooperation with spectrum estimation technique can be used. In this research, we considered this solution and propose a framework to generate spectral video from neurosurgery RGB video. The RGB video is captured using a digital camera connected with an operational microscope dedicated to neurosurgery. The result of this research generates near real time estimated spectral video which can be displayed in different ways.

We discuss about the estimation models in section 2, briefly present our methodology in section 3, then discuss the results in section 4, and then finally conclude.

2 Spectral estimation techniques

The basic idea of spectral estimation is to compute spectral response of a pixel value consisting RGB responses from a digital camera. The estimated spectral response will be a high dimensional representation of color signal within a desirable wavelength.

A reasonable number of estimation techniques have been proposed in literature and usefulness of these techniques was evaluated [5-10]. One of the most widely used techniques is Wiener estimation [5], [7], and [8], which minimizes the mean square errors (MSEs) between the recovered and measured spectral reflectances. In Wiener model, estimation matrix can be computed from different set of information. One set of information is reflectance, illumination and device sensitivity [7],[8]. The alternative set consist of only reflectance and corresponding RGB values [5]. Because of the unavailability of device sensitivity information, this research computes the estimation matrix from reflectance and corresponding RGB values. However, when necessary CIE color matching function is considered as sensitivity information. A modification of Wiener estimation is accomplished by a technique called pseudoinverse transformation method [7] which is also called least square method [9]. This technique uses regression analysis between the known spectral reflectances and corresponding device response values. Another category of the models are linear models where the spectral reflectance is represented by a linear combinations of the orthonormal basis vectors [7],[9]. Regression analysis is employed to modify the linear model, where a relation is established between the weight column vectors for the basis vectors and corresponding sensor responses. This modified method is called Imai-Berns model [6], [7], and [10]. One of the major focuses of Imai-Berns model is

to determine the optimal number of channel and basis vectors for sufficient estimation.

Different method requires different set of prior information. Prior knowledge required by different models discussed above is summarized in Table 1.

Table 1. Requirements of prior knowledge for each model.

	Wiener	Pseudoinverse	Linear	Imai-Berns
Sensitivities	Yes / No	No	Yes	No
Illumination	Yes / No	No	Yes	No
Reflectance	Yes	Yes	Yes	Yes
RGB values	No / Yes	Yes	No	Yes

3 Experimental procedure

The aim of this research is to establish a framework which generates neurosurgery spectral video from neurosurgery RGB video. The core operation is called spectral video generation. RGB video acquisition and spectral video visualization are two subparts of the system.

The RGB video is captured using a digital camera connected with an operational microscope dedicated to neurosurgery. A frame grabber is used to capture the video with spatial resolution 720x576 and 25 frames per second.

The task of spectral video generation is decomposed into two subtasks: (a) training spectra selection and (b) spectral video construction. Block diagram of spectral video generator is illustrated in figure 1.

Training spectra are collected from a database of spectral neurosurgery images. The database consists of 17 spectral images which were captured during surgery of 6 patients. Each spectral image was captured within the wavelength range of 420 nm to 720 nm at 10 nm interval. From the spectral images RGB images were generated using CIE color matching function and standard illuminant D65. These are considered as training RGB images.

The training spectra are collected by choosing certain percentage (1%, 5%, 10%, 20% and 50%) of random pixels from each image. In this random selection process, total 85 (17*5) different set of training spectra are collected for training. However, the final goal is to select only one set of training spectra which will be considered as a representative set. The representative set of spectra may not be the same for all estimation methods. Therefore, the searching procedure must be applied to each method separately. Steps required to search representative set are as follows.

Step 1: For each RGB image, estimate spectral image using each set of training spectra. Compute RMSE and select the set with lowest RMSE.
Step 2: Using each one of the training sets (obtained from step 1), estimate all spectral images. Compute average RMSE value. Then, sort them in increasing order.
Step 3: Choose the first five sets and generate all possible combination. With these combinations, follow the procedure in step 2. Then, select the best training set according to lowest average RMSE value.

Spectral video construction process begins by sequentially extracting the frames as RGB image from the video. Then, the spectral image is estimated from the RGB image using an estimation method. After that, the estimated spectral image is added as a frame to target spectral video. This process is continued until the last video frame is reached. Temporal aspect of video processing is maintained either by including wait functionality or by skipping few frames based on inter frame similarity.

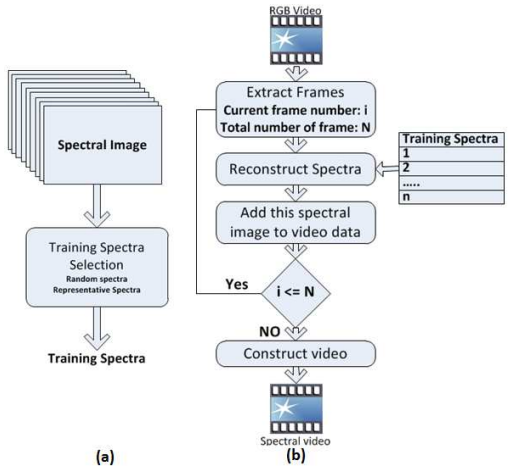

Fig. 1. Block diagram of spectral video generator. (a) Training data collection (b) Spectral video generator.

In order to visualize the spectral image, three visualization techniques are considered (a) single band visualization (b) three bands color image visualization and (b) all bands visualization with interactive filter.

4 Results and Discussion

Five spectral estimation models (described in section 2) have been applied to estimate 17 neurosurgery spectral images from RGB images. Accuracy of estimation is evaluated by computing root mean square error (RMSE) between actual and estimated spectral images. For each method, initially RMSE is computed for estimating 17 images using 5 sets of training spectra. Then the average RMSE values is calculated, which is used for evaluating the estimation models. Left part of table 2 illustrate the performance of the models in terms of accuracy and speed. In this experiment, three basis vectors are considered while estimation was performed with linear and Imai-Berns model. From the average RMSE value of table 2, it is clear that Wiener and pseudoinverse models are providing best accuracy. An investigation on low accuracy of the linear model reveals that, inclusion of device sensitivity and illumination decrease the accuracy. The plot of the right part of table 2 illustrates the recovered spectra from different models in comparison to actual spectra. A pixel from a vein of the brain surface is considered for this illustration. The plot illustrates that, the

recovered spectra from Wiener, pseudoinverse and Imai-Berns models are very much similar throughout the whole spectrum. Required computing time for a particular estimation task is listed in table 2. It is observed that pseudoinverse is faster than any other models. Therefore, in this research the pseudoinverse is considered for further estimations.

Table 2. Left: accuracy and required time of the models for estimating 17 spectral images. Right: Comparison between actual spectra and estimated spectra from all models.

	Avg. RMSE	Time (sec)
Wiener	0.029	0.031
Pseudoinverse	0.029	0.027
Linear	0.143	0.069
Imai-Berns	0.036	0.093

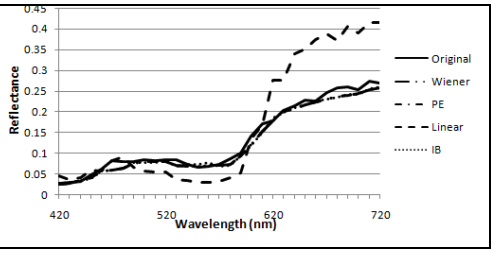

In order to further increase the accuracy of estimation using pseudoinverse model, different combinations of higher order terms of polynomials have been experimented. It is observed that the accuracy increases (average RMSE decreased) with certain combinations when the number of terms is increased. However, it is also important to note that computation time is proportional to the addition of terms. Therefore, there is a tradeoff between number of terms and computation time which should be considered depending on the demand of application. In this research, we choose [R, G, B, R2, G2, B2] for neurosurgery video estimation since it has reasonable balance between computation time and accuracy.

Table 3 presents the accuracy (in terms of average RMSE) of five best training datasets which are used to estimate all test spectral images. It can be concluded, that there is no significance difference between different datasets.

Table 3. Average RMSE of common training datasets to estimate all test images. Numbers indicate the percentage of data which has been collected from training images and numbers within '[]' indicate the images which were combined.

Dataset	5%, [2]	20%, [2]	5%, [2, 12, 17]	5%, [2, 7, 12, 17]	5%, [All]
Avg. RMSE	0.026	0.027	0.03	0.028	0.027

5 Conclusion

This research presents a framework for generating and displaying near real time neurosurgery spectral video. Each frame in the spectral video is generated using a spectrum estimation method. Five different estimation methods are examined for estimation. Pseudoinverse method is selected for video estimation considering its

accuracy and speed. It has been found that second order polynomial with six terms is the best choice. A searching technique has been proposed to find out the best set of training spectra. Temporal aspects of video have been considered and compromise between frame rate and speed is suggested. The experimental programs in this research are written in Matlab and the prototype is developed in C++ with OpenCV library. The methodology outlined here would also be just as applicable to other research, such as food quality inspection.

Acknowledgements

This work was financially supported by the Erasmus Mundus CIMET-master programme and by the Finnish Funding Agency for Technology and Innovation (Tekes).

References

1. 1. Yi, D., Kong, L., Wang, F., Liu, F., Sprigle, S., Adibi, A.: Instrument an Off-shelf CCD Imaging Sensor into a Handheld Multispectral Video Camera. In: Photonics Technology Letters, IEEE , vol.23, no.10, pp.606-608. IEEE (2011).
2. Yamaguchi, M.: Multispectral surgery video processing and display. In: 23rd Annual Meeting of the IEEE Photonics Society, pp.36-37. IEEE (2010)
3. Du, H., Tong, X., Cao, X., Lin, S.: A prism-based system for multispectral video acquisition. In: 12th International Conference on Computer Vision, pp.175-182. IEEE(2009)
4. Park, J., Lee, M., Grossberg, D., Nayar. S. K.: Multispectral Imaging Using Multiplexed Illumination. In: IEEE International Conference on Computer Vision, pp.1-8. IEEE (2007)
5. Stigell, P., Miyata, K., Hauta-Kasari, M.: Wiener estimation method in estimating of spectral reflectance from RGB images. In: J. Pattern Recognition and Image Analysis, Vol. 17, Nr. 2, pp. 233--242. Springer (2007).
6. Cheung, V., Westland, S., Li, C., Hardeberg, J., Connah, D.: Characterization of trichromatic color cameras by using a new multispectral imaging technique. In: J. Opt. Soc. Am. A 22, pp. 1231-1240. OSA (2005)
7. Shimano, N., Terai, K., Hironaga, M.,: Recovery of spectral reflectances of objects being imaged by multispectral cameras. In: Vol. 24, Issue 10, pp. 3211-3219. OSA (2007)
8. Haneishi , H., Hasegawa, T., Hosoi, N., A., Yokoyama, Y., Tsumura, N., Miyake, Y.: System design for accurately estimating the spectral reflectance of art paintings. In: Appl. Opt. 39, 6621–6632. OSA (2000).
9. Connah, D., Hardeberg, J.Y., Westland, S.: Comparison of linear spectral reconstruction methods for multispectral imaging. In: International Conference on Image Processing, vol.3, pp. 1497- 1500. (2004)
10. Imai, F., H., Berns, R., S., Tzeng, D.-Y.: A comparative analysis of spectral reflectance estimated in various spaces using a trichromatic camera system. In: J. Imaging Sci. Technol. 44, 280–287 (2000).
11. Gebhart, S., C., Thompson, R., C., Mahadevan-Jansen, A.: Liquidcrystal tunable filter spectral imaging for brain tumor demarcation. In: Appl. Opt. 46(10):1896–1910 (2007)
12. Hamed Akbari and Yukio Kosugi (2009). Hyperspectral Imaging: a New Modality in Surgery, Recent Advances in Biomedical Engineering, Ganesh R Naik (Ed.), ISBN: 978-953-307-004-9, InTech.

Bread Water Content Measurement Based on Hyperspectral Imaging

Zhi Liu [1], Flemming Møller[1,2]

[1] Department of Informatics and Mathematical Modelling, Technical University of Denmark, Kgs. Lyngby, Denmark
[2] Danisco A/S, Brabrand, Denmark
zliu@imm.dtu.dk

Abstract. Water content is one of the most important properties of the bread for tasting assesment or store monitoring. Traditional bread water content measurement methods mostly are processed manually, which is destructive and time consuming. This paper proposes an automated water content measurement for bread quality based on near-infrared hyperspectral imaging against the conventional manual loss-in-weight method. For this purpose, the hyperspectral components unmixing technology is used for measuring the water content quantitatively. And the definition on bread water content index is presented for this measurement. The proposed measurement scheme is relatively inexpensive to implement, easy to set up. The experimental results demonstrate the effectiveness.

Keywords: water content measurement, hyperspectral image, nonnegative matrix factorization

1 Introduction

The water content is one of the most important properties of the bread for tasting assesment or store monitoring. Generally, the higher the water content, the fresher the bread will be perceived by the consumers. On the other hand, too much water may be too soft for shaping. Therefore, evaluating the water content quantitatively is important for making bread.

Traditional methods for measuring the water content of bread are mostly destructive and time consuming. Recently, some work based on spectroscopic analysis has been done on food inspection [1,2]. Sepctrum imaging is relatively new technology to the agriculture and food industry. In spectroscopic analysis, hyperspectral imaging takes the advantage of both spectroscopic and image processing techniques, which can be simultaneously analyzed to see the spatial variations in an image as well as variations in spectral response of the pixels in an image. Both spatial and spectral information is important for quality monitoring and visualization of the food product as it can be used to extract the chemical mapping of

the sample and to analyze the distribution of chemical components in a sample. So using hyperspectral image technology for bread quality assessment over the storage period is a promising approach, which is non-contact and non-distractive.

In this paper, the proposed method for measuring the water content of bread is based on near infrared (NIR) spectrum imaging, which includes hyperspectral image preprocessing, spectral signature unmixing [3], and water content calculation. The primary purpose of this paper is to measure the water content of bread against the conventional loss-in-weight method for rapid and accurate quality assessment.

2 The scheme for water content measurement

The scheme mainly includes preprocessing (selection of region of interest (ROI), normalization and smooth), unmixing and water content calculation, which are demonstrated in Fig.1.

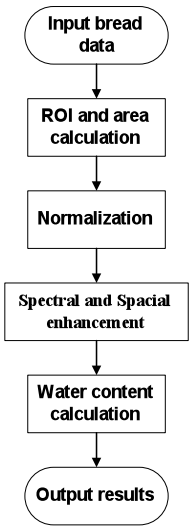

Fig. 1 the flowchart of the scheme for water content measurement

2.1 ROI

Spectroscopic systems should get more spatial field of view than the bread sample. Therefore hyperspectral imaging systems acquire abundant spatial information while collecting spectral information. So the selection of ROI can not only improve the accuracy of the measurement but also reduce the computing cost. In this study, the thin bread slice always has some holes which can affect the measurement significantly (shown in Fig 2).

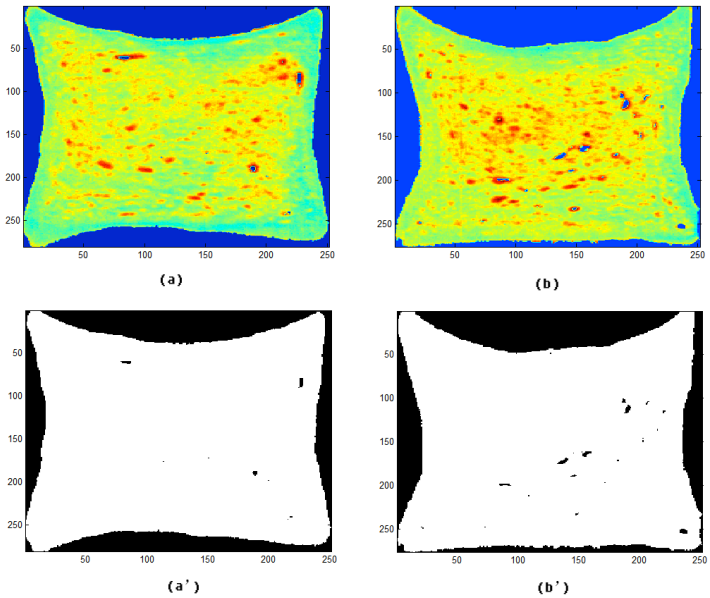

Fig. 2 The illustration of ROI operation

2.2 Normalization

Because of some sensory noise, the reflection spectral properties have some negative value. This problem is against the law of physics. Therefore, it is necessary to normalize the reflectance value. In this study, Eq. (1) is used for normalization.

$$w_{ijk} = \begin{cases} \dfrac{w_{ijk} - \arg(\min(w_{ijk}))}{\left\| \arg(\max(w_{ijk})) - \arg(\min(w_{ijk})) \right\|_2} \\ 0, \quad w_{ijk} < 0 \end{cases} \tag{1}$$

where w_{ijk} is the reflectance value at pixel the i^{th} row j^{th} column k^{th} waveband.

2.3 Spectral and spacial enhancement

Since reflectance at both small and large scattering distances is needed for accurate determination of the optical properties of the samples, an adequate signal-to-noise ratio (SNR) should be maintained, which is especially important for large scattering distances. For this reason, spectral averaging over three consecutive wavelengths was first performed to improve the SNR of the image data. Furthermore, the spatial

profiles from the two sides of the incident point were averaged to further enhance the SNR of the sample data.

2.4 Spectral unmixing

Non-negative Matrix Factorization (NMF) [4] is a matrix factorization algorithm that focuses on the analysis of data matrices whose elements are nonnegative, which can be used to extract the spectra of endmembers from the multi-array of mixed spectral observations.

2.5 Water content calculation

The conventional methods for the measurement of water content including drying the bread in an oven and weighting the bread slice are practicable, but they are also destruction and time consuming and difficult to integrate to on-line quality assessment. Therefore, the quantitative and non-contact methods for measuring the water content are necessary in bread production [5].

Considering the fact that the bread reflectance is predominantly affected by the optical properties of bread components, flour and water, the water content index (WCI) is proposed for measuring the water content.

WCI is defined as Eq.(2).

$$W = \log(\frac{\sum a_{ij}}{A}) = \log(\frac{\sum \left\| (\frac{1}{v_{ij}} - \frac{1}{v_{ref}}) \right\|}{A}) \quad (2)$$

where a_{ij} notes the water abundance at each pixel, and the $\left\| (\frac{1}{v_{ij}} - \frac{1}{v_{ref}}) \right\|$ represents the absolute value of the abundance value difference between the testing pixel and the reference value, and A means the area of the testing bread effective region, i.e. the ROI. So the index is higher, the level of water content in bread is higher.

3 Experimental results

Some NIR bread images used for the experiments are shown in Fig.3. These images are from four different kinds of bread slices with the selected wavebands.

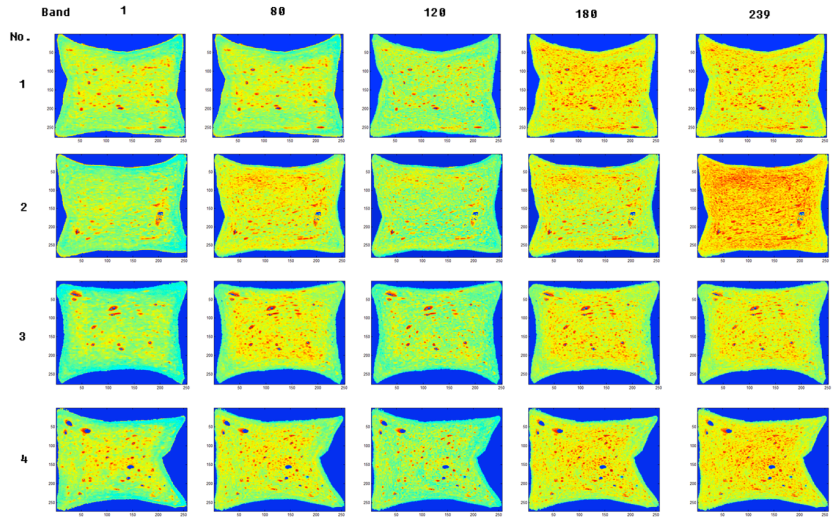

Fig. 3 Some samples in the bread NIR dataset

Through the spectral unmixing, the main components of bread can be separated, so that the water spectral properties are extracted before the measurement. In the unmixing process, the multiplicative updates using Euclidean distance by Lee. D.D. [6] is used for optimal value searching. This process is demonstrated in Fig.4.

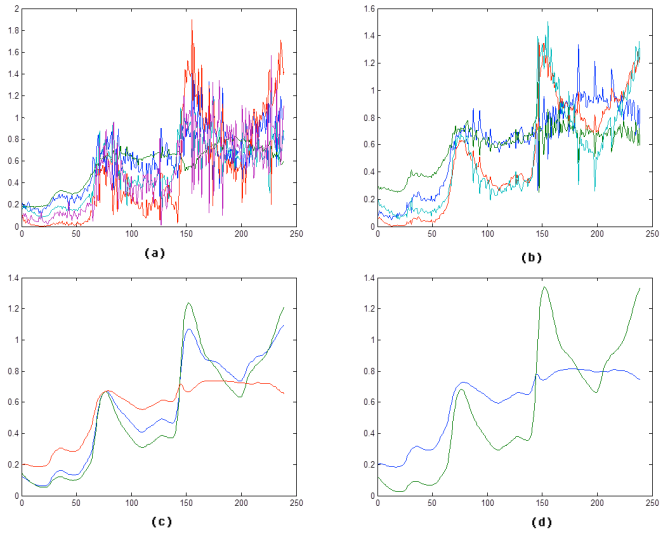

Fig.4 The results by unmixing the spectral image of bread assuming 5 different kinds components for (a), 4 for (b), 3 for (c) and 2 for (d).

Some computing results are listed in Table 1. From Table 1, it can be seen that the values of WCI are stable during changing the number of iteration of NMF. The experimental platform is Matlab® with Intel® i5 with 4G memory. The time cost on all these process on this dataset is less than 2 minutes

Table 1 Some water content index for the bread dataset

No.	WCI			
	Iteration (300)	Iteration (500)	Iteration (700)	Iteration (1000)
1	10.4912	10.4311	10.4212	10.4271
2	9.6609	9.6735	9.5547	9.6003
3	9.6504	9.6547	9.7100	9.6630
4	9.6142	9.6231	9.6283	9.6110

4. Conclusion

Water content measurement plays an essential role in food technology and it is subject to a fast growing interest due to increasing requirements in product quality control. The loss-in-weight techniques though simple and direct, are time consuming and destructive. In this paper, the NIR spectral imaging technique was used to effectively measure the water content of the bread slice. The experimental results show the performance of the proposed method based on NMF for measuring the water content of bread.

References

1. C. N. G. Scotter.: Non-destructive spectroscopic techniques for the measurement of food quality. Trends in Food Science & Technology. 8, 285--292 (1997)
2. C. B. Singh, et al.: Near-infrared hyperspectral imaging for quality analysis of agricultural and food products, pp. 767603--9. Orlando, Florida, USA (2010)
3. L. Parra, *et al*., "Unmixing Hyperspectral Data," presented at the Proc. Adv. Neural Inf. Process. Syst., (1999)
4. V. P. Pauca, et al., "Nonnegative matrix factorization for spectral data analysis," Linear Algebra and its Applications, vol. 416, pp. 29-47, (2006)
5. C. S.P. and Y. l.S., *Bakery Food Manufacture and Quality, Water Control and Effects*: Blackwell Science Ltd., 2000.
6. D. D. Lee and H. S. Seung, "Learning the parts of objects by nonnegative matrix factorization," Nature, vol. 401, pp. 788-791, (1999)

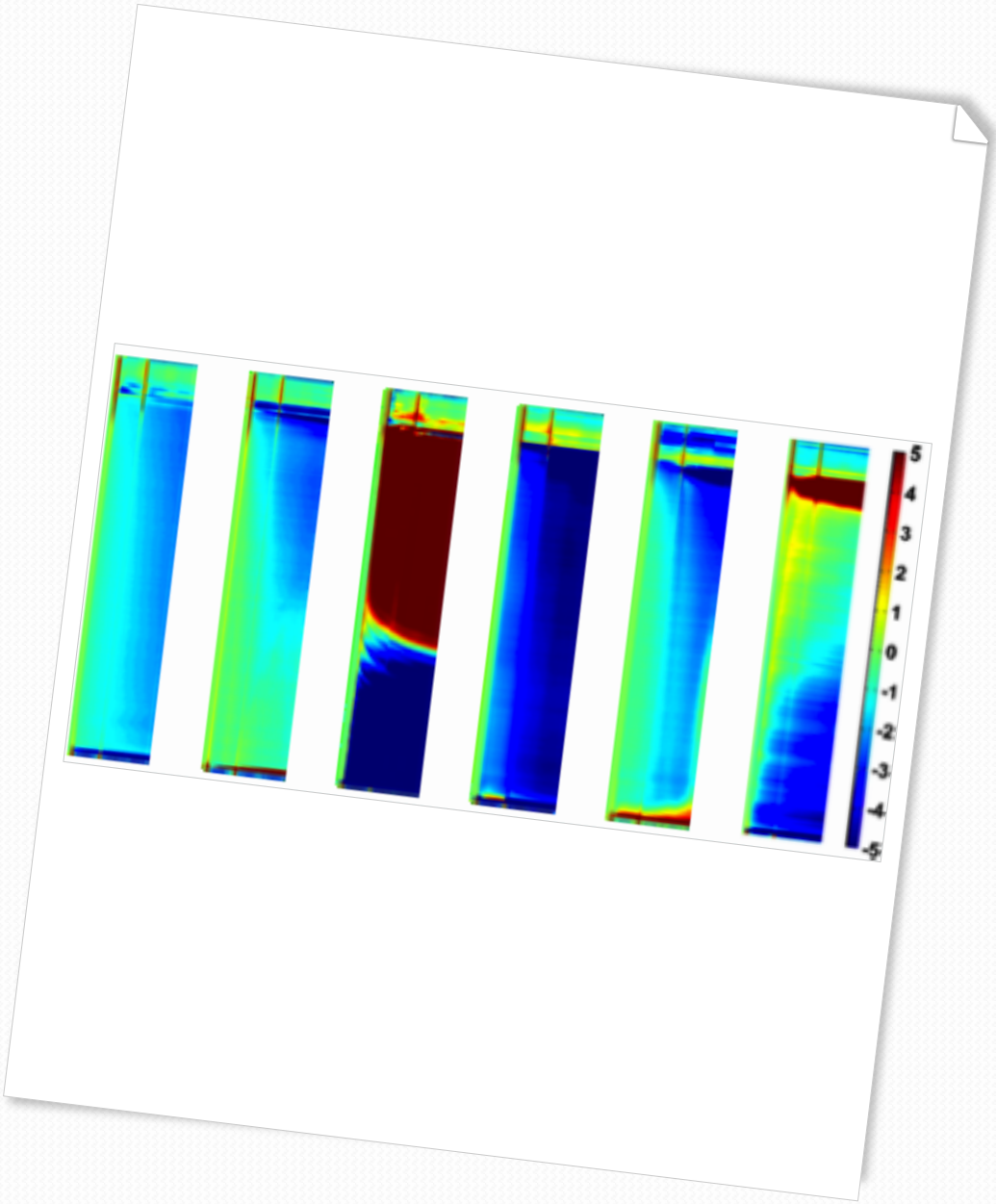

Scandinavian Workshop on Imaging Food Quality 2011

Proceedings
Ystad, May 27, 2011
IMM-Technical Report-2011-15